Université des Sciences et Technologies de Lille

Ecole Doctorale des Sciences Pour l'Ingénieur

# Étude de propriétés électroniques de nanostructures par microscopie à force atomique sous ultra-vide

## THÈSE

Présentée à l'Université des Sciences et Technologies de Lille

pour obtenir le grade de

**Docteur de l'Université des Sciences et Technologies de Lille**

**Discipline : Micro et Nanotechnologies, Acoustique et Télécommunications**

par

## Łukasz BOROWIK

**Soutenue le 14 décembre 2009 devant le jury composé de :**

Président

| | | | |
|---|---|---|---|
| **Alain CAPPY** | Professeur, Université Lille 1 | IEMN | Villeneuve d'Ascq |

Rapporteurs :

| | | | |
|---|---|---|---|
| **Benjamin GRÉVIN** | Chargé de Recherche CNRS | SPrAM | Grenoble |
| **Sébastien GAUTHIER** | Directeur de Recherche CNRS | CEMES | Toulouse |

Examinateurs :

| | | | |
|---|---|---|---|
| **Amal CHABLI** | Directeur de Recherche CEA | LÉTI | Grenoble |
| **Pere ROCA i CABARROCAS** | Directeur de Recherche CNRS | LPICM | Palaiseau |

Directeur de thèse :

| | | | |
|---|---|---|---|
| **Thierry MÉLIN** | Chargé de Recherche CNRS | IEMN | Villeneuve d'Ascq |

The scientific work described in this manuscript was performed at the Institut d'Electronique de Microélectronique et de Nanotechnologie (IEMN-CNRS) during my PhD, from October 2006 to October 2009.

I want to thank mainly my supervisor Dr Thierry Mélin, on whom I could always rely and ask for advice. It was really a pleasure to work with Thierry and I hope that we can still collaborate in the future.

Afterwards, I want to acknowledge all persons who helped me during this PhD: Heinrich Diesinger who participated a lot in teaching about atomic force and Kelvin force microscopy; Didier Théron and Koku Kusiaku for teaching me how to use COMSOL; Djamila Hourlier for preparing nanowire samples; Pere Roca i Cabarrocas and Thuat Nguyen-Tran for the doped nanocrystals; Christophe Delerue for discussions and Dominique Deresmes for technical support.

I would like also to thank all my friends and colleagues in Lille for creating a motivating and good atmosphere. Thanks to Marcin Marczak, Edern Tranvouez, David Brunel, Ondrej Kilian, Ludger Wirtz, Jean Philippe Nys and Florence Senez.

I would like to address special thanks to all my family especially to my wife Ania, for her patience and support, and to my parents and brother. I hope that we can meet all together in France.

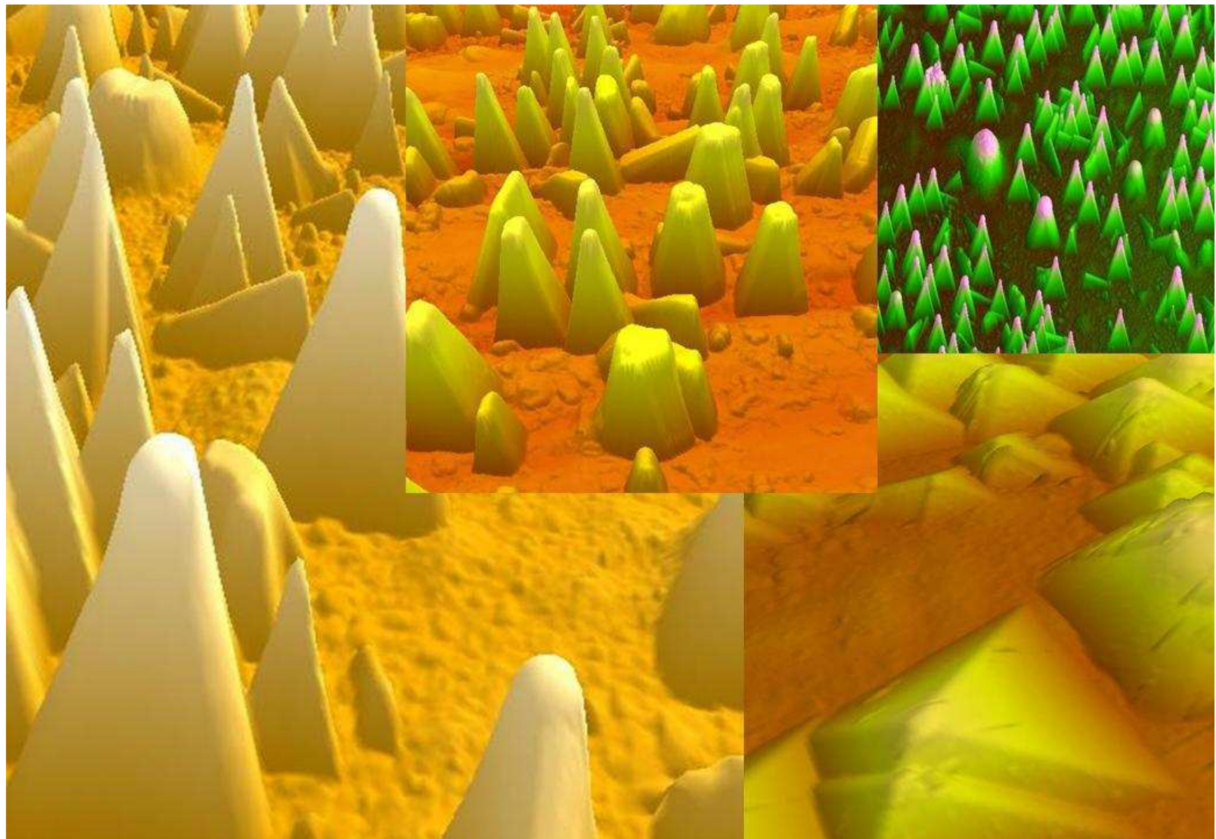

"Until man duplicates a blade of grass,

nature can laugh at his so-called scientific knowledge ...

it is obvious that we don't understand one millionth of one percent about anything."

- Thomas Edison

# Contents

**Résumé** ..... 7

**Abstract** ..... 9

**Chapter I: Introduction** ..... 11

**1.1 Nanotechnology** ..... 12
Can nanotechnology be important in daily life? ..... 12
Nanotechnology tools ..... 14

**1.2 Aim of this PhD** ..... 15
Aim of the work ..... 15
Description of the work done in this PhD ..... 16
Organization of the manuscript ..... 17

**1.3 Atomic Force Microscopy** ..... 18
1.3.1 Working principle ..... 18
1.3.2 Contact mode ..... 20
1.3.3 Tapping mode ..... 21
1.3.4 Electrostatic force microscopy ..... 23
Lift or linear scanning modes ..... 24
Imaging charged nanostructures ..... 26
Single charge resolution ..... 28
1.3.5 Kelvin force microscopy ..... 29
Operation principle ..... 29
Lift mode – linear mode ..... 30

**1.4 Atomic force microscopy in ultra high vacuum** ..... 31
1.4.1 Non-contact mode ..... 31
1.4.2 Kelvin force microscopy in vacuum ..... 33
1.4.3 Resolution and sensitivity in Kelvin Force Microscopy ..... 35

**1.5 Presentation of microscopes and cantilevers** ..... 36
1.5.1 Description of the Multimode microscope (Veeco Instruments) ..... 36
1.5.2 Description of the Dimension microscope (Veeco Instruments) ..... 36
1.5.3 Description of the Variable Temperature (VT) AFM (Omicron Nanotechnology) ..... 37
1.5.4 Cantilevers ..... 38

**References** ..... 39

**Chapter II: Electrical properties of semiconductor nanowires** ..... 43

**2.1 Introduction** ..... 44
2.1.1 Synthesis of silicon nanowires ..... 44
2.1.2 Applications of nanowires ..... 46
2.1.3 Nanowire properties - surface states and transport ..... 48

**2.2 Experiments** ..... 51
2.2.1 Intrinsic nanowires ..... 51
Analysis of as-grown silicon nanowires ..... 52
Analysis of de-oxidized silicon nanowires ..... 53
Heat treatment of nanowires ..... 56
I(V) measurements as a function of temperature ..... 57

**2.3 Conclusions** ..... 58

**References** ..... 59

**Charter III: Electrostatic properties of doped silicon nanocrystals** ..... 61

**3.1 Introduction......62**
3.1.1 Synthesis of silicon nanocrystals ...... 64
Synthesis of nanocrystals from solid sources...... 64
Synthesis of nanocrystals from liquid sources ...... 65
Synthesis of nanocrystals from gas sources ...... 66
Size-selection techniques ...... 69
Summary...... 70
3.1.2 Quantum confinement...... 71
3.1.3 Photoluminescence and the role of oxygen...... 71
3.1.4 Doped silicon nanocrystals ...... 74
3.1.5 Scanning probe microscopy experiments on silicon nanocrystals ...... 75

**3.2 Surface potential in air environment – why not possible? ......77**

**3.3 Charge transfer from doped silicon nanocrystals......80**
3.3.1 Sample preparation and setup for experiments in ultra high vacuum ...... 80
3.3.2 Intrinsic nanocrystals as reference samples ...... 81
3.3.3 Characterization of *n*-doped nanocrystals...... 83
3.3.4 Nanocrystal electrostatic potential for *n*-type doping ...... 85
3.3.5 Ionisation of the *n*-doped nanocrystals ...... 88
3.3.6 Characterization of *p*-doped nanocrystals...... 90
3.3.7 Electrostatic potential of intrinsic nanocrystals ...... 92
3.3.8 Nanocrystal electrostatic potential for *p*-type doping ...... 95

**3.4 Conclusions......96**

**References......98**

**Summary ......103**

**Annex A: Description of the numerical calculations used to analyze Kelvin force microscopy experiments......107**

**A 1 Introduction......108**

**A 2 Principle of calculation of surface potentials from static force fields......112**

**A 3 Simulations using Comsol Multiphysics ......114**

**A 4 Illustration of side-capacitance effects ......117**

**A 5 Calculations in the case of an oscillating tip ......120**

**A 6 Illustration of non-linear effects ......121**

**A 7 Measurement of the minimum tip-substrate distance ......122**

**A 8 Conclusion ......124**

**References......125**

**Annex B: Silicon nanocrystals after high temperatures treatments, and measurements at low temperatures......127**

**B 1 High temperatures treatments ......128**

**B 2 Measurements in low temperatures......129**

**Annex C: Amplitude-modulation KFM measurements on doped silicon nanowires......133**

**C 1 Preparation of samples......134**
Preparation of the nanowires...... 134

**C 2 Amplitude modulation Kelvin force microscopy measurements......135**

**List of publications and communications......137**

# Résumé

Cette thèse est consacrée à l'étude des propriétés électroniques de nanostructures par microscopie à force atomique (AFM) en ultra-vide.

La première partie de ce travail a consisté à caractériser localement des nanofils de silicium par technique d'AFM conducteur. Les expériences de conduction locale sur nanofils inclinés montrent que la conduction des nanofils intrinsèques est dominée par un transport en surface, associé à la présence de résidus catalytiques métalliques. Cette conduction peut être partiellement supprimée (par désoxydation) ou exaltée (par traitement thermique). Une caractérisation qualitative du dopage de ces nanostructures est présentée, par technique de microscopie à sonde de Kelvin.

La deuxième partie de la thèse a consisté à étudier le transfert de charges et les propriétés d'ionisation de nanocristaux de silicium passivés hydrogène, dopés de type *n* (P) ou *p* (B), fabriqués par dépôt plasma. L'analyse des images de microscopie à sonde de Kelvin en modulation d'amplitude sous ultra-vide montre que le transfert de charges des nanocristaux de silicium correspond à un mécanisme de compensation d'énergie, exalté par le confinement quantique. Les résultats expérimentaux fournissent une mesure de l'ouverture de la bande interdite des nanocristaux due au confinement quantique, dans la gamme 2-50 nm, en accord quantitatif avec des calculs en liaisons fortes. Ils mettent en avant la possibilité d'utiliser des nanocristaux dopés comme sources d'électrons pour réaliser un dopage sélectif contrôlé de nanostructures ou nanodispositifs, avec des densités dans les gammes de $2\times10^{11}$-$10^{14}$ cm$^{-2}$ ou $8\times10^{5}$-$2\times10^{7}$ cm$^{-1}$.

# Abstract

We study the electronic properties of nanostructures using atomic force microscopy in ultra-high vacuum environment.

The first part of this work consists in the characterization of silicon nanowires grown by metal-catalyzed chemical vapour deposition on silicon substrates, using conducting atomic force microscopy. The electrical transport at room and low-temperature through individual nanowires has been measured as a function of the position along tilted nanowires. It is shown that the conduction properties of as-grown intrinsic silicon nanowires are dominated by the presence of gold catalyst residues along their surface, which can be either partially suppressed (*e.g.* by a de-oxidation step), or enhanced upon heat treatment.

The second part of this work consists in studying the charge transfer and ionization properties of hydrogen-passivated phosphorus-doped and boron-doped silicon nanocrystals grown by plasma enhanced chemical vapor deposition on silicon substrates, using ultra high vacuum amplitude modulation Kelvin force microscopy. It is demonstrated that the charge transfer from silicon nanocrystals follows an energy compensation mechanism, which is enhanced by quantum confinement. The results provide a measurement of the nanocrystal conduction band-gap opening due to quantum confinement in the 2-50 nm range, in agreement with parametrized tight-binding calculations. They also put forward the possibility to use doped nanocrystals as electron sources to achieve a controlled remote doping of nanostructures and devices with typical two-dimensional charge densities in the range of $2\times10^{11}$-$10^{14}$ $cm^{-2}$, or linear charge densities in the range of $8\times10^{5}$-$2\times10^{7}$ $cm^{-1}$.

# Chapter I

## Introduction

## 1.1 Nanotechnology

The word nanotechnology defines the ensemble of techniques which can be used to create a nanoscale world. The history of nanotechnology starts back to the 1950s [1]. At this time Richard Feynman gave his famous lecture "There is plenty room at the bottom" [2]. At the beginning of this lecture, Feynman started to imagine what should be done to store the information contained in an encyclopaedia at the scale of the apex of a pin. He introduced the idea of miniaturization, and put forward the chance lying in technology, so as to operate at the scale of nanometers. At the end of his talk, he proposed two awards for future advances in miniaturization: *(i)* to make engines of size less than 1/64 of a cubic inch, and *(ii)* to write a book with proportion 1/25000. The first prize was won only ten years later (the engine had a power of 1mW), and the second prize by Thomas Newman in 1985 (the book was written by electron beam lithography). The application of nanotechnology is nowadays extremely wide, and covers the fields of electronics, chemistry, and biology. The interest for future applications of nanotechnology can be measured for instance from the investment of the European Community in nanoscience and nanotechnology from 2002 to 2006, of ~1.4 billion of euros, and covering 550 major nanotechnology-related projects.

**Can nanotechnology be important in daily life?**

The answer to this question is obvious and there are currently examples of applications which could revolutionize many fields of human life. We provide here below a few illustrations, in direct or indirect link with this PhD.

***Semiconductor nanocrystals*** provide one illustration with applications in medicine, due to their optical properties. They can be used as optical markers with a few nanometers in size and with a much larger optical stability as compared to organic markers, and are thus of great interest for immunofluorescence (labelling of antibodies or antigens using fluorescent markers). Many studies prove that single quantum dots can be optically observed under cytological conditions, with a sensitivity limit of one dot per one target molecule [3]. Nanocrystals can also be used as optical markers in living species. Kim *et al.* [4] injected near-infrared CdTe-CdSe core-shell quantum dots (optical emission at 850nm)

into the skin of live mice and pigs, and observed that quantum dots quickly migrate to lymph nodes[1]. Nanocrystals enable here to achieve background free images of lymph nodes, allowing their image-guided resection. They could be very helpful in human surgery.

Nanocrystals are also promising technological materials for optoelectronic applications like wavelength tunable lasers [5] or solar cells [6]. Ian Gur [6] demonstrated inorganic donor-acceptor mechanisms for solar cell from CdSe and CdTe nanorods. They produced donor-acceptor heterojunctions by deposition of CdTe and CdSe films, on indium tin oxide glass, coated with alumina. The device operation (*i.e.* electron-hole pair separation) is due to the type II band-gap structure (with a staggered gap as shown in Figure 1.1, left). The solar cell exhibits a current density of 10 mA/cm$^2$ under a simulated solar illumination (Figure 1.1, right), showing the possibility to achieve solar cells based on colloidal semiconductor nanocrystals.

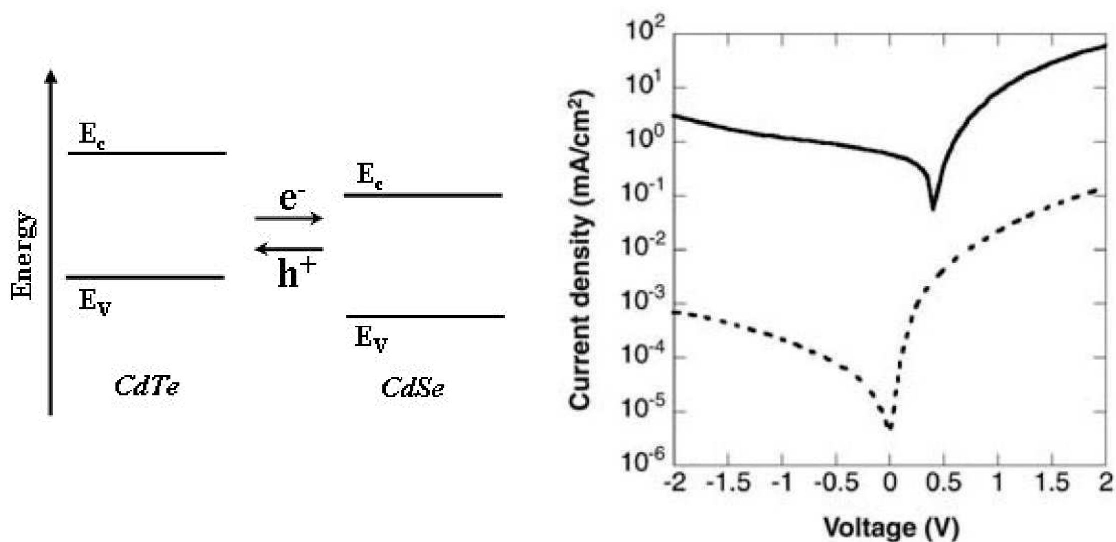


*Figure 1.1 Left: energy diagrams of CdTe and CdSe, and transfer between those materials. Right: I-V characteristics for the CdTe and CdSe solar cells device in the dark (dotted line) and under simulated one-sun AM 1.5G illumination (solid line). From Ref. [6].*

Some early experiments have also shown how ***semiconductor nanowires*** can be used to build the next generation of computing devices [7]. For example, *p-n* junctions, one of the simplest electronic devices, have been achieved from bottom-up nanowires (either by physical crossing of a *p*-type nanowire over a *n*-type nanowire or by longitudinal growth), and the formation of logic gates (AND, OR, and NOT gates) has been

[1] Lymph nodes are a part of the lymphatic system, and act as filters or traps for foreign particles.

demonstrated from connected *p-n* junctions. This shows that silicon nanowires could become important for the future of digital computing.

**Nanotechnology tools**

Dedicated tools have been developed to probe or manipulate the properties of matter at the atomic or nano scale. We will not describe here fabrication techniques (synthesis, lithography etc…), but rather illustrate the advance in nanoscale characterization from the example of scanning-tunnelling microscopy [8] (STM) invented by Binnig, Quate and Gerber in 1981, who were awarded with the Nobel Prize in 1986.

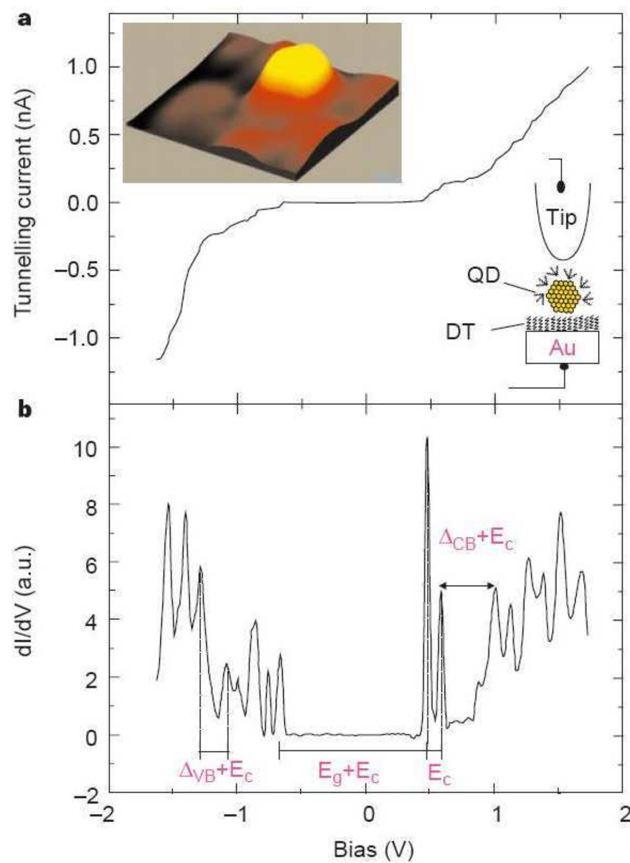


*Figure 1.2 Scanning tunnelling microscopy and spectroscopy of a single indium arsenide (InAs) nanocrystal 3.2 nm in radius, acquired at 4.2 K. The nanocrystal quantum dots are linked to the gold substrate by hexane dithiol molecules (DT), as shown schematically in the right inset. Left inset: a 10 × 10 nm STM topographic image, showing the nanocrystal. a) Tunnelling I-V characteristics over the nanocrystal, exhibiting single-electron effects. b) Tunnelling conductance spectrum obtained by numerical differentiation of the I-V curve. The arrows depict the main energy separations:* $E_c$ *is the single-electron charging energy,* $E_g$ *is the nanocrystal bandgap, and* $\Delta_{VB}$ *and* $\Delta_{CB}$ *are the spacing between levels in the valence and conduction bands, respectively. From Ref. [9].*

The STM first offered the possibility to observe in real space and to manipulate atoms, but also to perform local electronic measurements (*e.g.* of the density of states) from its spectroscopy modes (tunnel current or its derivatives as a function of the tip voltage).

This has been applied to the case of single nanocrystals such as in the work of Banin *et al.* [9] or Liljeroth *et al.* [10], in which the tunnel current versus voltage spectroscopy (see Figure 1.2) shows plateaus (peaks in the differential conductance) corresponding to tunnelling events through the nanocrystal discrete electronic states [11], and thus, related to their electronic structure. The STM is however by essence restricted to experiments made with conducting (*i.e.* metallic or semiconducting) materials. It is mainly to overcome this difficult and to enable more convenient scanning possibilities in air or liquids and on insulators, that the first atomic force microscope (AFM) has been invented in 1986 by Binnig, Quate and Gerber. In contrast with the STM, it gathers local information by "feeling" the surface using a mechanical probe (tip/cantilever, or tip/tuning fork sensors), with the possibility to reach the atomic resolution as in STM [12]. Spectroscopic modes have been developped so far which measure either electrostatic force gradients (Electrostatic Force Microscopy or EFM) or surface potentials (Kelvin Force Microscopy or KFM). These techniques – unlike STM techniques – are well suited to the nanoscale characterization of electrical devices, which are by essence fabricated on insulating substrates. This makes these tools very important for nanoelectronics applications. AFM, EFM and KFM techniques will be explained in a detailed way in the section 1.3 of this chapter.

# 1.2 Aim of this PhD

**Aim of the work**

The main aim of this work was to use atomic force microscopy in ultra-high vacuum environment so as to characterize the electronic properties of individual nanostructures, here semiconductor nanowires or nanocrystals. As already mentioned, the choice of a mechanical probe (rather than a tunnel probe) corresponds to the requirement to develop characterization tools to be used on insulators, *i.e.* able to actually probe nanodevices in their environment. The specific use of atomic force microscopy *in ultra-high vacuum* (*i.e.* with respect to ambient air experiments) is twofold: *(i)* it allows a much better lateral resolution and sensitivity (here down to a few electrons in KFM experiments)

as compared to ambient air experiments (see e.g. [13] on silicon nanocrystals, with a sensitivity of a few tens of elementary charges in EFM experiments); *(ii)* it enables a control of the nanostructure surface states. This aspect is extremely useful as for silicon nanocrystals, which can be kept hydrogen-passivated during a few days.

The issues which can be addressed with respect to silicon nanostructures such as bottom-up silicon nanowires [14] or silicon nanocrystals [15] are:

• to probe the local transport in nanostructures;

• to characterize the influence of surface states (gold residues in case of a catalytic growth, oxide or residual surface states in case of hydrogen-passivated silicon nanostructures) on the nanostructure transport or electrostatic properties;

• to investigate charge transfers at the nanoscale, as due to surface state charging or intentional nanostructure doping;

• to probe band-structure effects such as quantum confinement on the basis of mechanical measurements.

To resolve such problems, several modes of atomic force microscopy have been used in this PhD. First, conducting-AFM, in which the AFM tip is used to measure the local transport through nanostructures. This mode has been applied to characterize the local conduction properties of as-grown semiconductor nanowires, as well as their surface states due to gold and oxide. The second variant of AFM microscopy is Kelvin force microscopy (KFM) which is a non-contact electrical technique used to measure local surface potentials, and thus, local charge transfers. This technique has been applied to study doped silicon nanowires and nanocrystals, and was found particularly adapted to study the charge transfer (ionization properties) from doped silicon nanocrystals in an ultra-high vacuum environment. This enabled to establish that the charge transfer mechanisms from doped silicon nanocrystals are driven by quantum confinement effects.

**Description of the work done in this PhD**

Silicon nanowires grown by Vapour-Liquid-Solid (catalytic) chemical vapour deposition (nanowire growth made by D. Hourlier – IEMN) have been first investigated by conducting atomic force microscopy experiments in ultra-high vacuum. The aim was to obtain *local* transport information (*i.e.* conductance spectroscopy along the nanowires). Local current-voltage characteristics have been taken as a function of position along (111)-

oriented tilted nanowires. It is shown that: *(i)* the conduction along as-grown intrinsic nanowires is dominated by gold residues associated with the catalytic growth, which can *(ii)* be partially removed by chemical de-oxydation and *(iii)* recovered upon thermal annealing.

We investigated in a second step the doping properties of silicon nanostructures from their charge transfers after hydrogen-passivation. This was done first qualitatively in the case of doped silicon nanowires, and, in a second step, in the case of individual nanocrystals with diameter in the 2-50 nm range (nanocrystal growth: T. Nguyen-Tran – LPICM), for which we fully investigated the charge transfer mechanisms. It was shown that the charge transfer from doped silicon nanocrystals follows an energy compensation mechanism similar to remote doping, but is however strongly enhanced by quantum confinement. Results provide a measurement of the nanocrystal band-gap opening in the 2-50 nm range, in agreement with parametrized tight-binding calculations, and put forward the possibility to use doped nanocrystals as electrons sources to externally control the doping of nanostructures and nanodevices.

**Organization of the manuscript**

This PhD is divided into three chapters and three annexes.

• The first chapter provides a general introduction to the PhD, followed by a description of atomic force microscopy techniques: working principle of AFM in air and vacuum for topography measurements, as well as AFM electrical modes adapted to charge (EFM) or surface potential (KFM) detection. The microscopes used during this PhD are presented at the end of this chapter.

• The second chapter describes the measurements performed on semiconductor nanowires. Its first part encloses a short bibliography on the synthesis, applications, and electronic properties of nanowires. Its second part reports about the measurement on silicon nanowires by conducting AFM, and the role of gold catalyst residues and/or oxide on the nanowires conduction properties.

• The third chapter is devoted to the electronic properties of doped silicon nanocrystals. It contains first a bibliography about the synthesis of nanocrystals, and their

electronic properties like quantum confinement, photoluminescence, doping, and finally a review of scanning probe measurements on silicon nanocrystals. The second part of the chapter contains a description of the experiments made during this PhD by KFM on silicon nanocrystals in the case of intrinsic, *n*-type doped, and *p*-type doped nanocrystals on *n*-type or *p*-type doped substrates, together with their analysis in terms of surface states, doping and quantum confinement.

Finally, a set of three annexes provide: (A) an extensive description of the electrostatic calculations used for quantitative measurements in Chapter III; (B) KFM measurements on doped silicon nanocrystals at low-temperature and after temperature annealing; and (C) KFM measurements performed on intrinsic and doped silicon nanowires.

## 1.3 Atomic Force Microscopy

### 1.3.1 Working principle

Atomic force microscopy enables to image pure insulators or semiconductor materials [16] because it uses a force sensor (cantilever or tuning fork), rather than the electrical probe (tunnel current) used in STM.

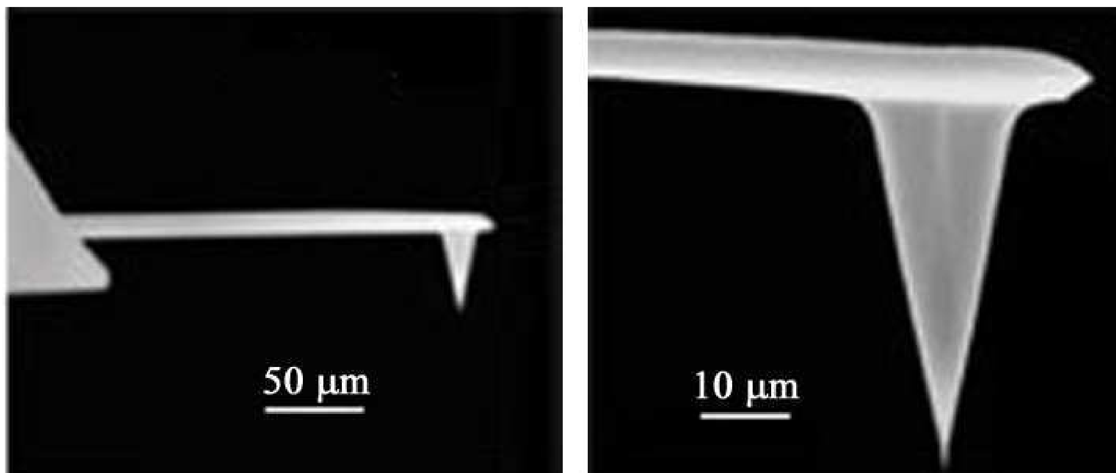


*Figure 1.3 Scanning electron microscopy image of an atomic force microscopy cantilever.*

Nowadays AFM is also frequently used as a device to image and manipulate matter in the nanoscale environment. The mechanical interaction between the AFM tip and a

sample corresponds to very small forces (typically less than 1nN), and is transformed into a three-dimensional topography image using a "constant force" feedback loop (in practise, more frequently, a constant cantilever oscillation amplitude or frequency shift). To obtain a high sensitivity to forces, flexible cantilevers must be used, with typical spring constants 10 N/m. Cantilever tips have apexes with radius around 10-25 nm [7].

Depending on the microscope and scanning mode, different forces can be measured by AFM, ranging from short-range (contact) forces, to non-contact forces such as Van der Waals or electrostatic forces. When the tip is sufficiently close to the sample so that a force can act on it, a cantilever deflection can then be measured, as illustrated in Figure 1.4 in the case of an optical beam AFM. In this case, the cantilever deflection is measured from the reflection of an incident laser on the cantilever, which is collected on two photodiodes. The deflection of the cantilever can be estimated from the quantity of light which comes on each photodiode.

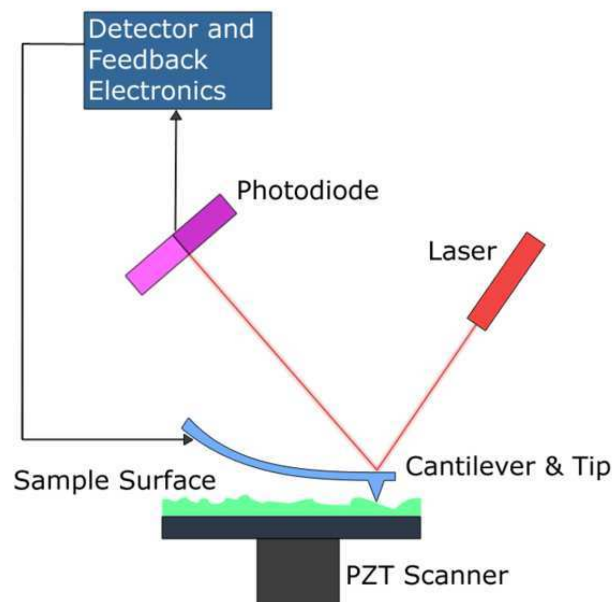


*Figure 1.4 Schematics of an optical-beam atomic force microscope. From Ref. [7].*

To control the tip-sample distance and to scan the sample (horizontal displacement), a piezoelectric scanner is used, and can either support the sample (as in Figure 1.4) or the cantilever. A feedback system is introduced to keep a constant interaction (*e.g.* a deflection in contact mode) so as to record the sample topography image. The resolution in topography depends on the tip (shape, apex diameter), but also on the environment (vacuum, liquid or air conditions), and on the operation mode of the microscope (intermittent contact or tapping, contact, non-contact, etc.).

## 1.3.2 Contact mode

The contact mode was the first mode used to obtain a topography image by AFM. By contact mode it is possible to perform a lot of investigations which are not possible to be realized by another modes: manipulation of nanostructures [17], charging [18] or conductivity measurements [19].

In this mode, the contact force on the tip is typically around $10^{-10}$ N, the force F being related to the deflection z by the Hooke's law F=kz, where k is the cantilever spring constant. Soft cantilevers (k~0.01 N/m) are often used, so as to produce significant deflections, while maintaining low interaction forces. The deflection can be either positive or negative, depending on the repulsive or attractive character of the interaction force.

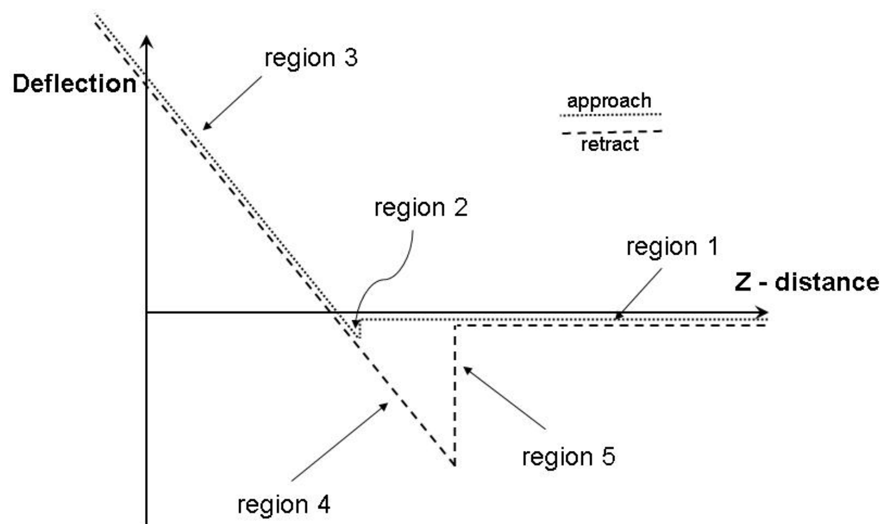


*Figure 1.5 Approach-retract curve with five interaction regions [18].*

A schematical approach-retract curve (also called "force curve") in shown in Figure 1.5. Five regions can be considered as a function of the tip-substrate distance: when the tip is far from the surface (region 1, no interaction), when the tip experiences a jump-to-contact to the surface (region 2), when the tip is repelled by the surface (region 3, the deflection is positive). A distinct behaviour is observed when the tip is retracted from the surface, because of attractive (adhesion or capillary) forces, leading a region of negative deflection (region 4), followed by a null interaction (region 5) when the tip is separated from the surface.

The major artefact in AFM topography (and not specifically related to contact mode) is “tip convolution”, as illustrated in Figure 1.6, showing that only the height of a single nanostructure can be measured correctly, while its width is also dependent on the tip shape and size. An experimental illustration of this effect is obtained from our experiments using pyramid shape contact mode cantilevers (Figure 1.6) to image vertical or tilted nanowires (see Chapter II for details). In that case, since the nanowires have a much larger aspect ratio than the pyramidal tip, the AFM image corresponds to an image of the tip shape, associated with each of the vertical nanowires, thus leading to the occurrence of pyramids in the topography image of Figure 1.6.

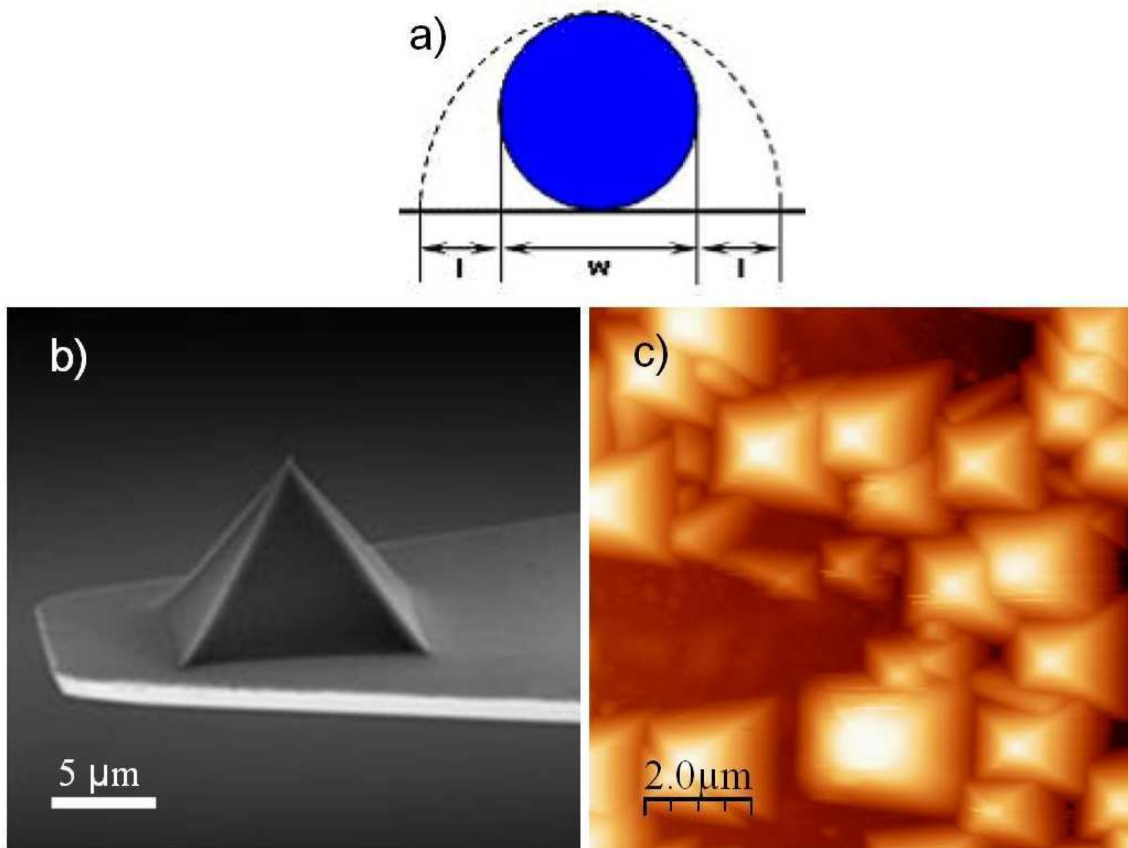


*Figure 1.6 a) Schematics of nanoparticle and trajectory of the tip, dashed line. Schematics shows overestimation of real diameter due to tip shape. b) Pyramidal contact tip from Ref. [20]. c) Topography image of vertical and tilted silicon nanowires. Since the nanowires have much larger aspect ratio comparing to pyramidal tip, the AFM image corresponds to the image of the tip shape.*

### 1.3.3 Tapping mode

In tapping mode or intermittent-contact mode, the cantilever is actuated by an additional small piezoelectric element (which is usually mounted inside the cantilever

holder) at a frequency close to its resonance frequency. This generates a cantilever oscillation (see Figure 1.8), with a typical amplitude of a few tens of nanometers in ambient air. The control of the interaction between the tip and sample is here based on a reduced value of the cantilever oscillation amplitude when the tip is brought into mechanical interaction with the surface.

We here below describe the actuation of the cantilever upon an oscillating excitation force. This description holds to describe the mechanical resonance curves used in tapping or non-contact mode, but is also valid for an electrostatic actuation.

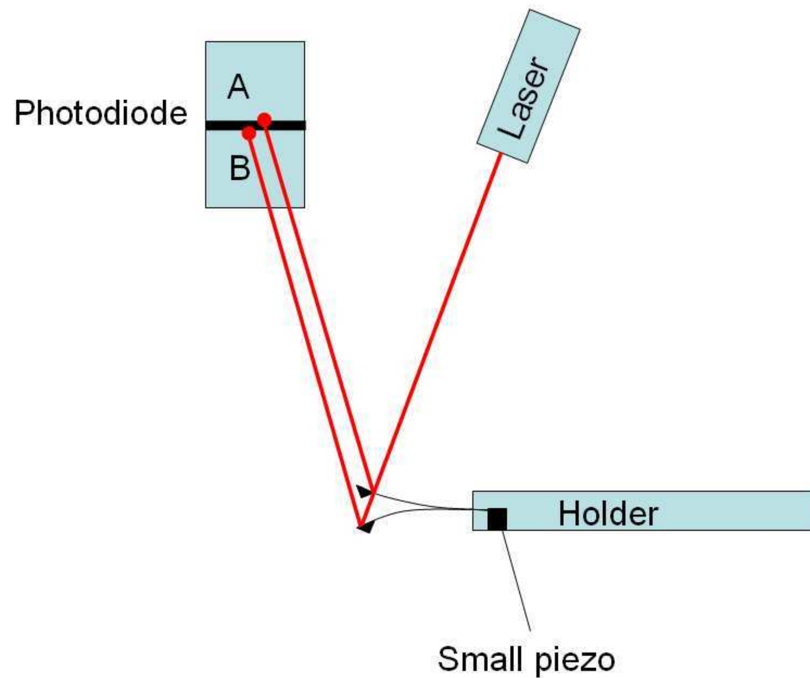


*Figure 1.7 Actuating system of a cantilever, made from small piezo-element mounted in the cantilever holder. The ac excitation of the piezo-element leads to a cantilever oscillation, detected as an ac-component on the photodiode.*

If the excitation force is $F=F_0\cos(\omega t)$ (in which $\omega$ is angular frequency and t is time), the equation of motion for the cantilever is:

$$m_c\ddot{z} + \alpha\dot{z} + kz = F_0\cos(\omega t)$$

where $m_c$ is mass of cantilever, $\alpha$ and k are constants. Dividing this equation by $m_c$ and taking: $\alpha/m_c=\beta$, $k/m=\omega_0^2$ and $F_0/m_c=B$, this equation now reads:

$$\ddot{z} + \beta\dot{z} + \omega_0^2 z = B\cos(\omega t)$$

where $\beta$ is a value dependent on the fluid damping of the oscillator, and $\omega_0$ is the cantilever resonance angular frequency.

The solution of this equation is:

$$z(t) = A(\omega)\cos[\omega t - \phi(\omega)]$$

$$A(\omega) = \frac{B}{\sqrt{(\omega_0^2 - \omega^2)^2 + \beta^2\omega^2}}$$

$$\phi(\omega) = \arctan\frac{\beta\omega}{\omega_0^2 - \omega^2}$$

where A(ω) is amplitude and φ(ω) is the phase shift between the cantilever oscillation and its excitation. For small value of β and $\omega << \omega_0$, the phase shift is nearly zero; for $\omega = \omega_0$ it equals -π/2; and for $\omega >> \omega_0$, it is nearly -π. An important parameter which defines the cantilever motion is its quality factor Q, defined by $\boldsymbol{Q = \omega_0 / \beta}$. The cantilever quality factor can be viewed as the ratio between the cantilever oscillation amplitude at the resonance frequency $\omega_0$ divided by the deflection which would result from a static force of same amplitude. The width of the cantilever resonance (defined at $1/\sqrt{2}$ of the amplitude at the cantilever resonance frequency) is $\Delta\boldsymbol{\omega = \omega_0 / Q}$. In air (see Figure 1.8), Q equals ~100, but is strongly enhanced in vacuum where Q values of 20000 are reached routinely.

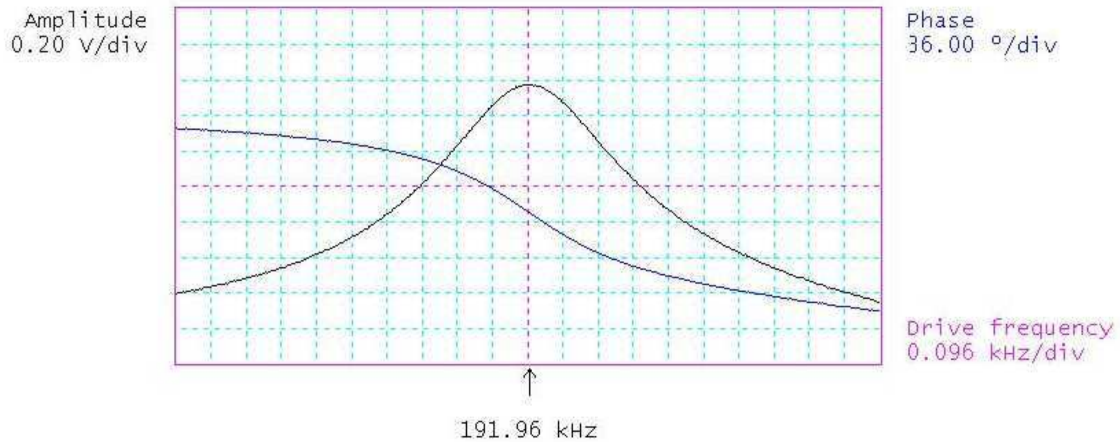


*Figure 1.8 Experimental resonance frequency curve of an AFM cantilever (here with resonance frequency ~200kHz). The black colour curve corresponds to the response in amplitude, and the pink colour curve to the phase response of the cantilever oscillation with respect to the excitation. An arbitrary phase shift has been introduced for the phase curve.*

### 1.3.4 Electrostatic force microscopy

Electrostatic force microscopy (EFM) is a variant of AFM, in which the tip is separated from the surface so as to be only sensitive to long-range electrostatic forces, and to discard short-range surface forces. Electrostatic forces are imaged from the map of the

cantilever frequency shifts (corresponding in fact to a measurement of electrostatic force gradients), with a typical accuracy of $\Delta f/f_0 \sim 10^{-5}$-$10^{-6}$ corresponding to force gradients of a few $10^{-5}$ N.m$^{-1}$ [21]. The sensitivity of EFM in terms of charge detection in ambient air has reached the level of elementary charge in specific situations such as the case of blinking nanocrystals [22], and using modulated EFM techniques.

**Lift or linear scanning modes**

EFM has been extensively applied to study silicon nanocrystal charging at IEMN [13][23][24][25][26]. This paragraph will be mainly based on this work. We first illustrate the artefacts which can occasionally take place in EFM (or KFM) images, and associated with the modes used for EFM imaging. Two modes can be used in practice. The first one is called "linear mode", and corresponds to a "constant height" scanning mode. It is obtained by recording the sample topography in a first pass (Figure 1.9 a), and recording the EFM data in a second pass, with a tip displacement corresponding to a constant height z between the tip and substrate plane (Figure. 1.9 b). The second mode is called "lift mode", and corresponds to a "constant distance" scanning mode. It is also obtained by recording the sample topography in a first pass (Figure 1.9 a), but by reproducing the topography data above the sample (Figure 1.9 c) while recording the EFM data in the second pass. This constant distance mode was originally developed so as to maintain a constant capacitance between the tip and substrate, but can become inappropriate for nanoscale studies, as illustrated below, and lead to strong artefacts in EFM images.

We first illustrate EFM measurements for uncharged nanostructures (Figure 1.9) and compare linear and lift-modes. In the linear mode, a negative shift of frequency (or phase) is observed upon tip bias, due to the local increase of capacitance when the tip is scanned over a nanostructure (see Figure 1.9 b, e and f). The lift-mode images (see Figure 1.9 c, g and h) do not show the expected null frequency shift, because the EFM tip probe interacts with a larger sample area, as compared to the nanostructure topography. It is observed that a negative frequency shift is around the nanocrystal when the tip is moved parallel to the substrate as in the linear mode, but that a positive frequency shift is monitored as soon as the tip is lifted so as to reproduce the sample topography. This effect is due to an overall decrease of the tip-substrate capacitance associated with the tip lift, and induces a footprint of the sample topography image onto the EFM image, although the EFM image is recorded with large tip-substrate distance (75 nm or 125 nm in Figure 1.9).

Such behaviour (Figure 1.9 g or h) is typical of artefact driven images associated with a lift-mode, in which a z-dependent quantity [here: the cantilever frequency shift associated with the z-dependent tip-substrate capacitance second derivative C''(z)] is imaged with a probe that reproduces the sample topography. This artefact is also expected to take place in KFM images (see here after) in which the sample surface potential $V_s$ is recorded, which can also be, in practice, z-dependent.

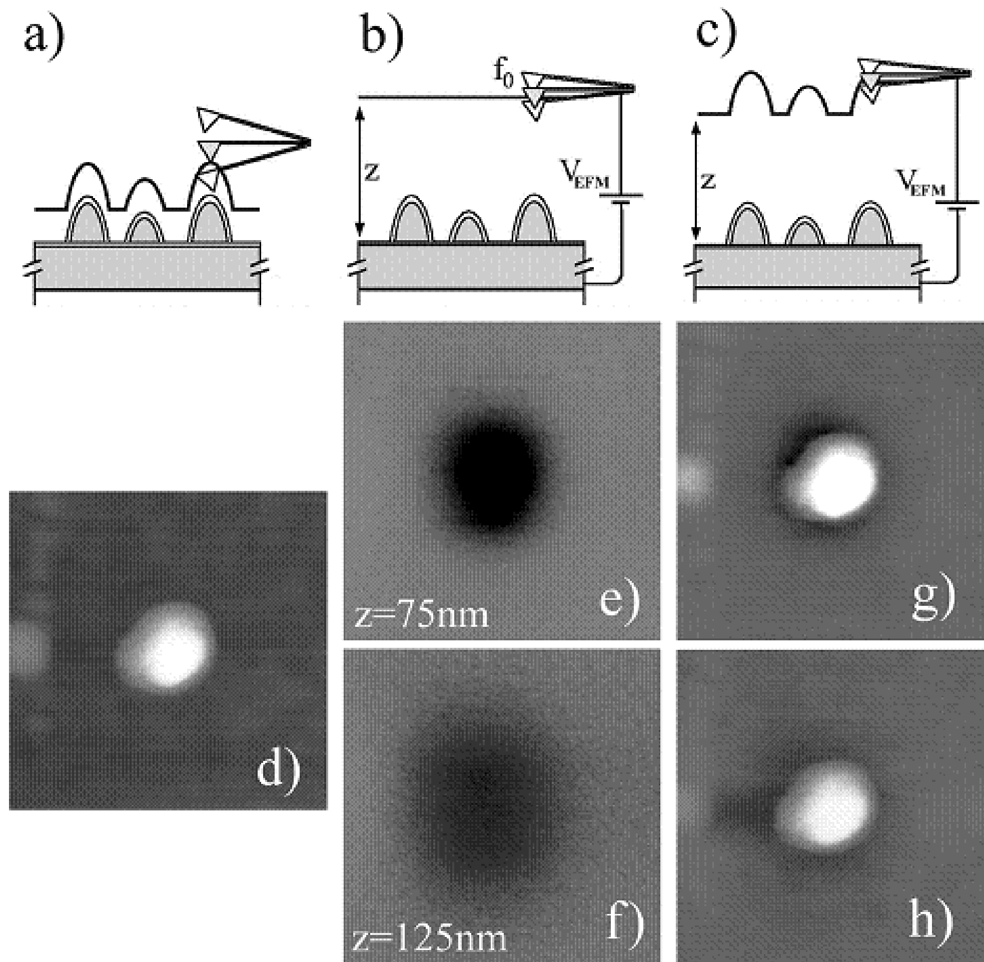


*Figure 1.9 a) Principle of topography imaging in tapping mode of silicon nanoparticles deposited on silicon substrate. b) EFM measurement in linear-mode: the tip is moved with constant distance z over the sample substrate. The EFM data consist in the variation Δf of the nominal cantilever frequency $f_0$. c) EFM measurement in the lift mode: the sample topography is reproduced during the EFM pass over the surface. d) 250 nm × 250 nm topography image of a 30 nm high nanoparticle on a silicon substrate. e) EFM phase image in the linear-mode for $V_{EFM}$=5 V and z=75 nm showing a -2,5° maximum phase shift over the nanoparicle. f) Same image in the lift-mode (+5,7° phase shift). g) EFM image in linear mode for $V_{EFM}$=10 V and z=125 nm showing a -1.0° phase shift. h) Same image in the lift-mode (+6.15° phase shift). From Ref. [24].*

**Imaging charged nanostructures**

The understanding of EFM signals on charged nanostructures require dissociating between charge and capacitive signals [23]. This is illustrated in Figure 1.10, in which four situations are presented: *(i)* a situation in which no electric force occurs (Figure 1.10 a), provided the EFM tip voltage $V_{EFM}$ equals the sample surface potential $V_S$ (in that case the cantilever oscillation frequency is $f_0$); *(ii)* the situation in which a non-zero bias $V_{EFM}$-$V_S$ occurs between the tip and substrate, leading to capacitive frequency shifts associated with the gradient of the attractive capacitive force between tip and surface $\Delta f_{t\text{-}s} \leq 0$ (Figure 1.10 b), and the increase $\Delta f_\varepsilon$ of this signal when the tip is passed over a nanostructure (Figure 1.10 c) as already discussed in experimental measurements of Figure 1.9. Both signals are proportional to $(V_{EFM}-V_S)^2$. And finally *(iii)* the situation in which a charge Q is inserted in the tip-substrate capacitance, which leads to an additional image charge signal proportional to $Q^2$, and an interaction term between the nanostructure charge and capacitive charges on the tip apex. This element is proportional to $(V_{EFM}-V_S)\times Q$, and can be either positive or negative provided the two charges repel or attract each other.

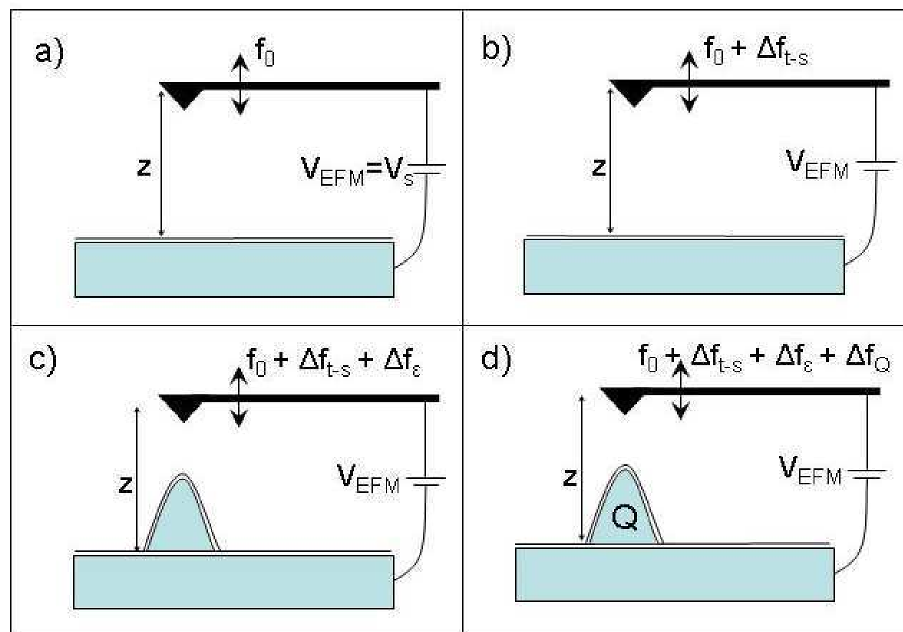


*Figure 1.10 a) EFM signal with the bias $V_{EFM}$ on the tip equals the surface potential $V_s$. b) EFM signal with the $V_{EFM} \neq V_s$. c) EFM measurement over a nanostructure for $V_{EFM} \neq V_s$ leading to an additional capacitive frequency shift $\Delta f_\varepsilon$. d) Frequency shift $\Delta f_Q$ when the nanostructure holds a charge Q.*

An experimental illustration of EFM signals can be presented from the work of Zdrojek *et al.* who performed EFM measurement on carbon nanotubes (Figure 1.11) [27].

The uncharged nanotube corresponds to Figure 1.11 b), with a capacitive EFM signal proportional to $(V_{EFM}-V_S)^2$, and the charged nanotube to Figure 1.11 c), in which the dominating EFM signal associated with the nanotube is the charge contribution proportional to $(V_{EFM}-V_S)\times Q$, leading here to repulsive force gradients (equivalently: a positive frequency shift) associated with the bright feature in the EFM image.

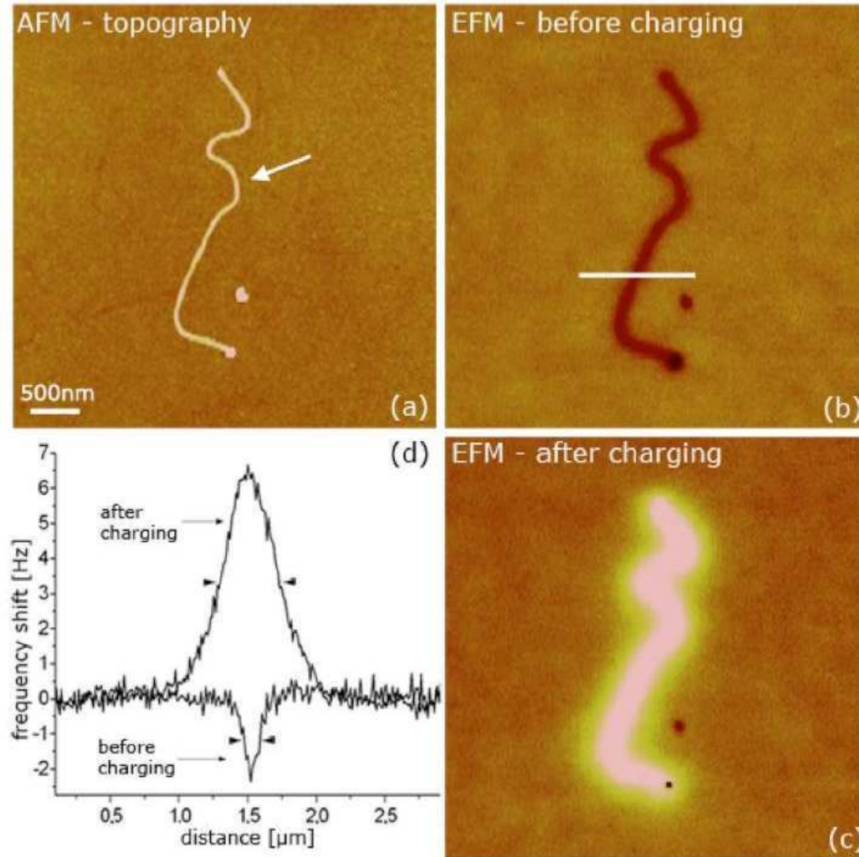


*Figure 1.11 a) AFM image of multi walled nanotube of 19 nm diameter on a 200 nm silicon dioxide surface. b) EFM image $V_{EFM}=-3$ V acquired before charging (10 Hz colour scale) with a tip-substrate distance z=100 nm. c) EFM image taken in the same conditions, after a charge injection performed at the point indicated by an arrow in a), using $V_{inj}=-5$ V for 2 min. d) Cross sections of the EFM scans for the cases b) and c). The position of the cross section is shown by the horizontal bar in b). From Ref. [27].*

To illustrate the wide range of use of EFM techniques, we present now a recent work from U. Banin *et al.* [28], detecting the electrostatic response of Au-CdSe nanodumbbells (see Figure 1.12) by EFM. This hybrid nanoparticle is made from a CdSe rod with gold nanoparticles on each side [29]. Nanodumbbells were deposited on highly oriented pyrolytic graphite covered with a thin insulating poly (vinyl brutal) layer, and measured under photoexcitation.

*Figure 1.12 Schema of Au-CdSe nanodumbbell.*

Due to the particular energy levels in those structures, the photocreated electrons are transferred to the gold nanoparticles, while the photocreated holes tunnel from the CdSe nanorod towards the substrate. The nanodumbbells are therefore imaged as negatively charged, with a net charge of the order of five electrons per single nanodumbbell, as revealed from EFM images.

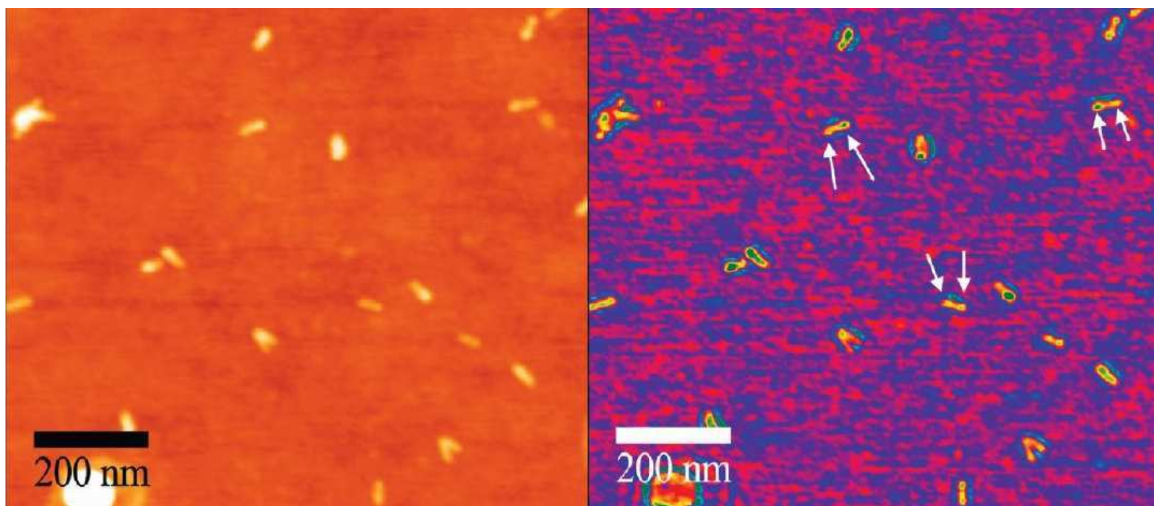


*Figure 1.13 AFM tapping mode topography image (left) of nanodumbbells with the corresponding phase image (right) showing contrast difference between the gold tips (arrows) and the CdSe rods. From Ref. [28].*

**Single charge resolution**

EFM is an instrument in which the single electron resolution can be obtained. For example, in specific situations in air environment, as in the work of T. D. Krauss and L. E. Brus [22], who performed electrostatic measurements of CdSe nanocrystals ~5 nm in diameter, using a modulated (1ω/2ω) EFM technique, and observing the "blinking" state of the nanocrystals, found to be either neutral or holding a single positive elementary charge. Stomp *et al*. [30] more recently detected single electron phenomena using EFM spectroscopy as a tool to induce single-charge jumps in a semiconductor nanocrystal. Such experiments have been performed in high vacuum and at low temperature (4.2 K).

## 1.3.5 Kelvin force microscopy

**Operation principle**

Kelvin force microscopy (KFM) is an implementation of the macroscopic Kelvin probe on atomic force microscopes, first realized in 1991 [31]. In KFM, an electrostatic excitation (DC+AC voltage) is applied to the tip at the cantilever resonance frequency (Figure 1.14), in contrast with EFM, in which a static bias is applied to the mechanically excited cantilever. The electrostatic excitation generates a cantilever oscillation if the cantilever DC bias does not match the sample surface potential $V_S$. To measure $V_S$, a feedback is introduced so as to nullify the cantilever oscillation frequency at the electrostatic excitation angular frequency. This generates a map of the surface potential $V_S$ (see Figure 1.15).

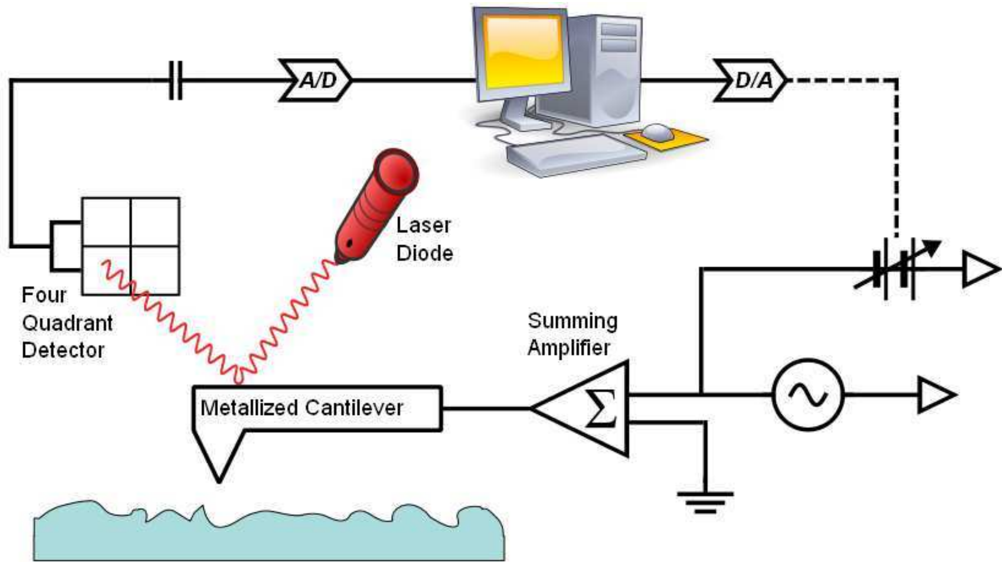


*Figure 1.14 Block schema of Kelvin force microscope. From Ref. [7].*

More quantitatively, the force acting on the cantilever can be understood by considering that the energy of the capacitor formed by cantilever and surface is [7]:

$$E = \frac{1}{2}C[V_{dc} + V_{ac}\sin(\omega_0 t)]^2$$

where C is tip-substrate capacitance, $V_{dc}$ and $V_{ac}$ are the DC and AC components of the applied voltage. The force acting on the cantilever is then given by [32]:

$$F = \frac{1}{2}\frac{\partial C}{\partial z}[(V_{dc} + V_{ac}\sin(\omega t)) - V_S]^2$$

where $V_S$ is potential difference between the tip material and the sample material, and z the tip-substrate distance. It is visible from the above equation that the electrostatic force can

be decomposed into three force components (a static component and two oscillating components at the angular frequencies ω and 2ω):

$$F = F_{dc} + F_{\omega} + F_{2\omega}$$

The three components are given by

$$F_{dc} = \frac{1}{2}\frac{\partial C}{\partial z}\left[(V_S - V_{dc})^2 + \frac{V_{ac}^2}{2}\right]$$

$$F_{\omega} = \frac{\partial C}{\partial z}(V_{dc} - V_S)V_{ac}\sin(\omega t)$$

$$F_{2\omega} = -\frac{1}{4}\frac{\partial C}{\partial z}V_{ac}^2\cos(2\omega t)$$

The amplitude of the cantilever vibration at ω is directly proportional to the spectral component of the force at the angular frequency ω. It is thus proportional to ($V_{dc}$-$V_S$) and will be nullified provided $V_{dc}$=$V_S$.

**Lift mode – linear mode**

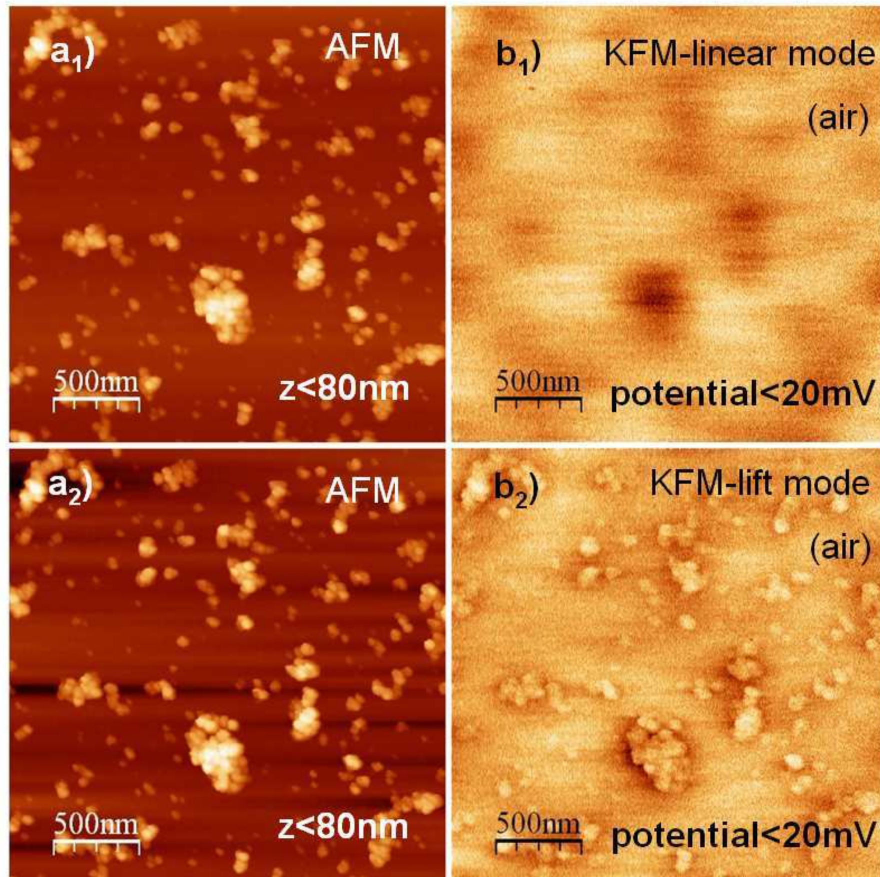


*Figure 1.15 Topography ($a_1$, $a_2$) and KFM images in linear ($b_1$) and lift ($b_2$) modes of silicon p-doped nanocrystals on p-doped surface. These measurements were done in air environment.*

Similarly to EFM, KFM images are generally established in ambient air in a mode for which the tip is retracted from the surface, *i.e.* lift-mode or linear mode. In practice, the KFM signals can exhibit variations as a function of the tip-substrate distance z. This can be due to for instance the presence of local surface charges, which induce an effective z-dependent surface potential $V_S(z)$. In such a situation, one can expect that lift-mode images can suffer from the same topography footprint artefacts as EFM images (see Figure 1.9). This point is illustrated in Figure 1.15.

# 1.4 Atomic force microscopy in ultra high vacuum

## 1.4.1 Non-contact mode

The main interests of non-contact AFM (NC-AFM) are: nanoscale or atomic resolution on semiconducting or insulating materials, or the measurement of electric potential to characterize materials at the nanoscale [33]. The majority of the experiments in air or in liquids are performed with amplitude modulation (AM) mode (see e.g. the description of tapping-mode imaging), while most experiments in ultra high vacuum (UHV) are performed with frequency modulation (FM) mode. AM would be an unsuitable technique for UHV, because the high quality factor of the cantilevers in vacuum (Q~20000) would imply extremely slow feedback responses (the typical time constant for a cantilever with resonance frequency $f_0$=100 kHz and Q=20000 is $2Q/f_0$=0.4 s). In FM mode, the cantilever is kept oscillating at its resonance frequency with a fixed amplitude[2], and it probes the shift in resonance frequency associated with the forces acting between the tip and sample. The minimum detectable frequency shift depends on the cantilever parameters and the detection bandwidth B is [34]:

$$\delta(\Delta f) = \delta(f - f_0) = \sqrt{\frac{f_0 k_B T B}{2\pi k Q \left\langle z_{osc}^2 \right\rangle}}$$

where $f_0=(1/2\pi)*(k/m)^{-1/2}$ , k is stiffness of cantilever, m is the cantilever mass, Q the quality factor, $\langle z^2_{osc}\rangle$ is the mean-square amplitude of the driven cantilever vibration and $k_BT$ is the thermal energy at temperature T. This equation shows that the sensitivity of electrostatic measurements can already be improved in UHV due to the quality factor of the cantilevers (Q~20000) with respect to ambient air (Q~200). Such values for Q are

[2] A feedback loop is introduced to maintain the cantilever oscillation amplitude constant.

illustrated in Figure 1.16, showing the first resonance ($f_0$~67 kHz) of an EFM PPP Nanosensors cantilever when mechanically excited, and its first higher-order resonance at $f_1$~422kHz, here electrostatically excited.

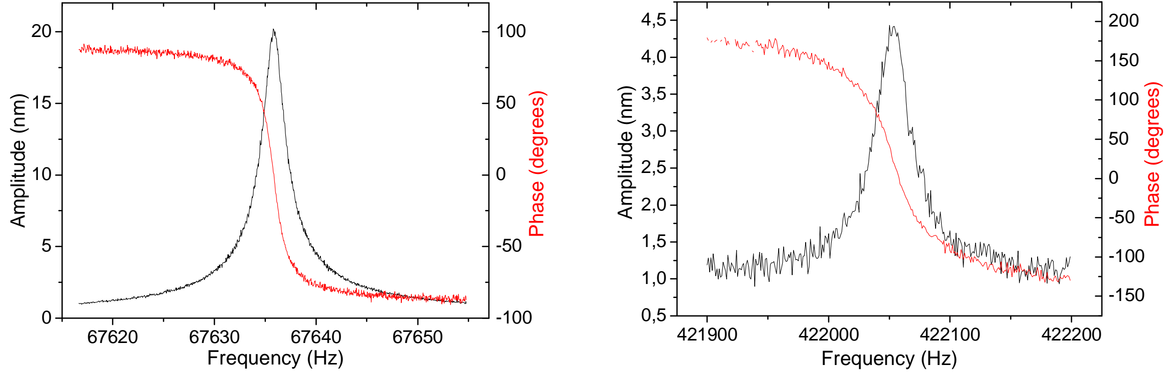


*Figure 1.16 Plots with oscillation amplitude (black line) and phase (red line) for tip Pointprobe-plus PPP-EFM 50 (Nanosensors). The left plot is representing the oscillation amplitude and phase for the cantilever first resonance using a mechanical excitation with here a Q factor~20000, and the right plot represents the resonance of the first higher-order resonance, obtained here using an electrostatic excitation (Q factor~10000).*

The force between the tip and sample $F_{ts}$ has long and short-range contributions. In vacuum, there are Van der Waals, electrostatic, magnetic, and short range chemical forces. The van der Waals interactions are caused by fluctuations in the electric dipole moment of atoms and their mutual polarization. For a spherical tip with radius R close to a flat surface, the Van der Waals potential is given by [33]:

$$V_{vdW} = -\frac{A_H R}{6z}$$

where $A_H$ is the “Hamaker constant” and depends on the type of materials of the tip and sample (it is in order of 1eV for most solids). If the tip and sample are conductive and have an electrostatic potential difference (U≠0), a (capacitive) electrostatic force will also take place, given by:

$$F_e = -\frac{\pi\varepsilon_0 R U^2}{z}$$

Chemical forces are more complicated. Potentials for chemical bonds are the Morse potential:

$$V_{Morse} = -E_{bond}\left(2e^{-\kappa(z-\sigma)} - e^{-2\kappa(z-\sigma)}\right)$$

and the Lennard-Jones potential:

$$V_{Lennard-Jones} = -E_{bond}\left(2\frac{\sigma^6}{z^6} - \frac{\sigma^{12}}{z^{12}}\right)$$

These potentials describe a chemical bond with bonding energy and equilibrium distance. Very often, the variation of surface forces with the tip-sample distance is compared with the case of a tunnelling current, so as to compare AFM and STM techniques. The tunnelling current is monotonic as function of the tip-sample distance and has by essence very sharp (exponential) distance dependence. In contrast, the tip-sample force has both long and short-range components and is not monotonic (see Figure 1.17).

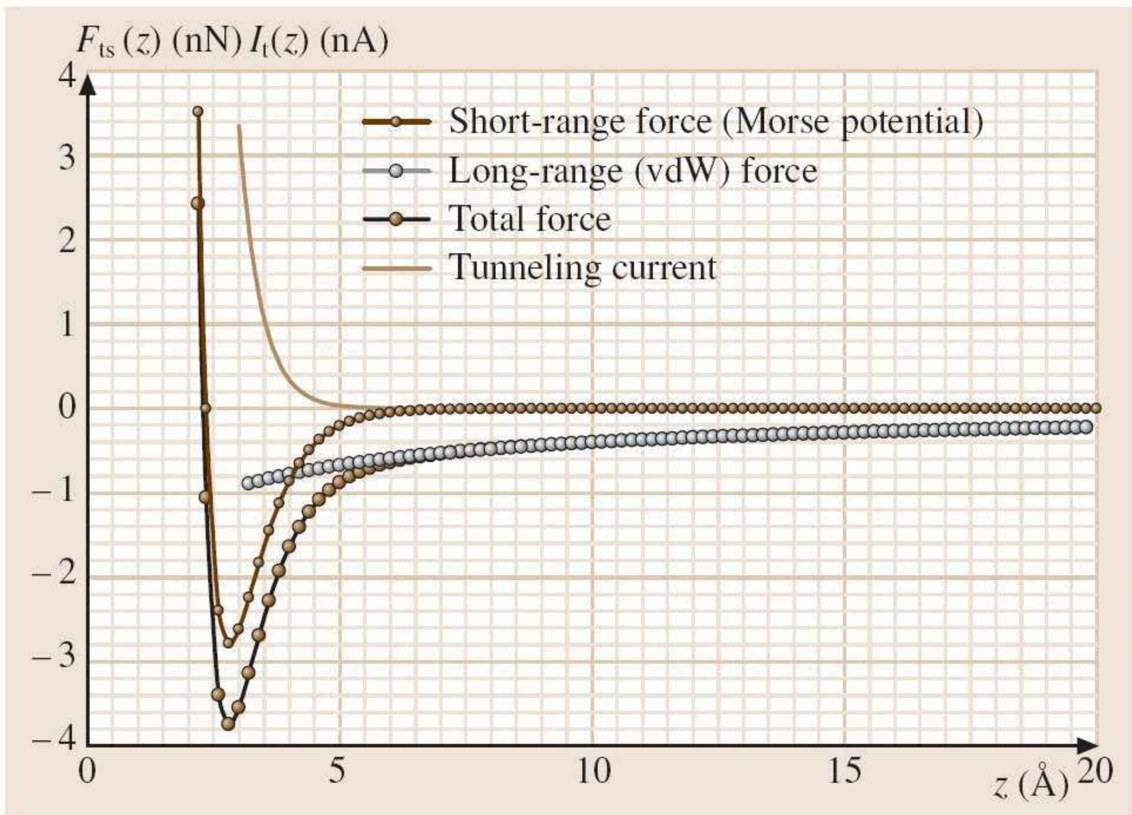


*Figure 1.17 Plot of the variations of a tunnelling current $I_t$ and of the force $F_{ts}$ as a function of distance z between the front atom of a tip and a surface atom layer. From Ref. [33].*

## 1.4.2 Kelvin force microscopy in vacuum

While KFM in air is (in general) realized after recording the sample topography, KFM in vacuum can be conveniently implemented simultaneously with topography. Two modes can be used for such measurements: frequency modulation (FM-KFM) or amplitude modulation (AM-KFM) [35].

In FM-KFM, a low-frequency AC voltage is applied to the tip, and induces a modulation of the electrostatic force gradients. This modulation can be measured by detecting the oscillation at ω of the frequency variation of the resonance. A DC voltage is then applied by a feedback loop to nullify the AC shift of the cantilever frequency shift at the excitation angular frequency ω, which is given by the following equation:

$$\Delta f_1(\omega) \propto \frac{\partial F_\omega}{\partial z} = \frac{\partial^2 C}{\partial z^2}(V_{dc} - V_S)V_{ac}\sin(\omega t)$$

The AM-KFM implementation corresponds to the implementation of KFM described for ambient air measurements, but using a higher-order cantilever resonance to perform simultaneously the topography and the KFM measurements [36].

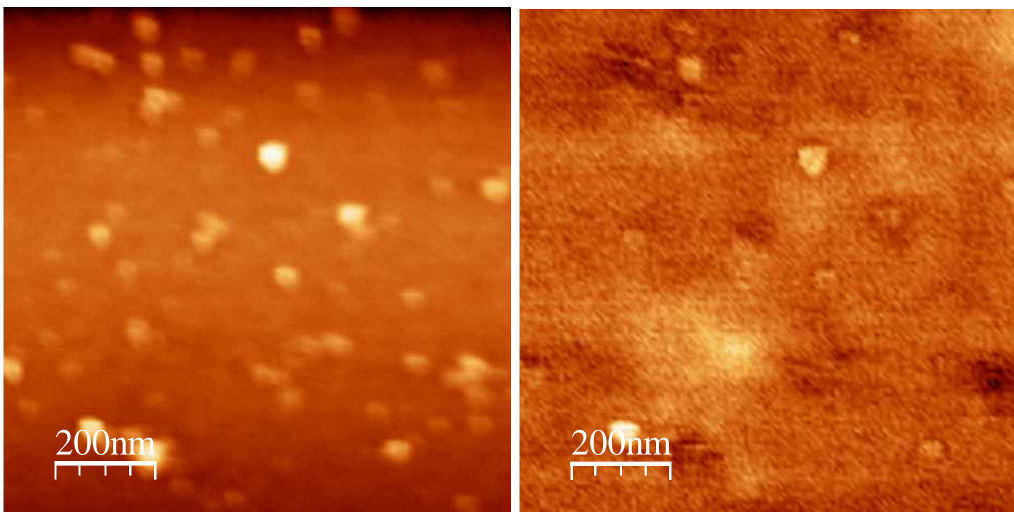


*Figure 1.18 Topography of the intrinsic silicon nanocrystals in non-contact (left) (z<30 nm) and simultaneous AM-KFM (right) (-20<z<40 mV).*

In the case of low-frequency cantilevers such as in Figure 1.16 ($f_0$=67 kHz), the second resonance at $f_1$=6.25$f_0$ ~420 kHz still falls within the AFM photodiode bandwidth as provided by the manufacturer, and can be electrostatically excited (Figure 1.16, right) to build a KFM loop, while the first resonance can be used to record the sample topography. Such a mode therefore looks like the lift mode used in air. However, due to the small z distance (typically 20nm) used in non-contact mode (and thus, the better lateral resolution), this mode is not sensitive to the artefacts debated in Figures 1.9 and 1.15 for ambient air by EFM and KFM measurements. This is illustrated in Figure 1.18, in which the topography of silicon nanocrystals is showed in non-contact mode, together with the simultaneously acquired AM-KFM data on the cantilever second resonance. Experiments were done on intrinsic nanocrystals deposited on an *n*-type silicon surface, and nanocrystals were covered by native oxide (measurement were done without any passivation of the sample).

The KFM signals in Figure 1.18 are however not correlated to the topography, because of large quantity of the surface states (see Chapter III and section 3.3).

### 1.4.3 Resolution and sensitivity in Kelvin Force Microscopy

KFM technology is a powerful tool to obtain maps with surface potential distribution on conducting, semiconducting or insulating samples. It was however shown [37] that the measured surface potential ($V_{dc}$) does not match the actual local surface potential ($V_S$), if the sample surface potential is not homogeneous. In that case, the measured surface potential $V_{dc}$ is a weighted average of all potentials around the tip, with weighting coefficients depending on the local capacitances[3] (Figure 1.19) [37]:

$$V_{dc} = \frac{\sum_{i=1}^{n} (C'_{it} \cdot V_i)}{\sum_{i=1}^{n} C'_{it}}$$

The magnitude of the measured surface potential $V_{dc}$ will therefore depend on the size of the feature of interest, its surroundings, but also on the probe geometry. Thus, to obtain the real value of surface potentials at the nanoscale, the measured KFM signals have to be interpreted using a model which takes into account the full geometry of the sample and tip. The principle and the extensive description of such effects are provided in the Annex A of this manuscript.

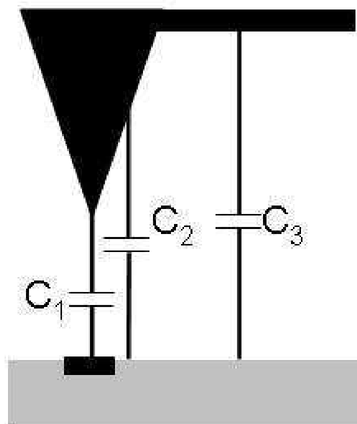


*Figure 1.19 KFM setup in which electrostatic interactions are represented by mutual capacitances $C_i$, between the cantilever tip and the surface.*

[3] In this formula, capacitance gradients have been introduced, which correspond to the situation of AM-KFM. The second derivatives of capacitances should be rather introduced in the case of FM-KFM measurements.

# 1.5 Presentation of microscopes and cantilevers

We present here microscopes and cantilevers, which have been used during this PhD thesis. Two microscopes are working in atmospheric pressure (Multimode and Dimension) and one is ultra high vacuum (UHV) system (VT-AFM).

## 1.5.1 Description of the Multimode microscope (Veeco Instruments)

The Multimode microscope with Nanoscope IIIa controller is designed to work in air environment or nitrogen atmosphere (by putting a capsule on the microscope enabling a dry nitrogen flow). Its head (Figure 1.20) contains: the cantilever, laser diode, photodiodes and cantilever piezoelectric actuator. Since the sample is mounted on the piezoelectric scanner, only small size samples (less than 10×10 mm$^2$) can be investigated, with a maximum scan size of 12×12 μm², and vertical piezo displacement of ~2 μm. This microscope has been used for silicon nanocrystal samples (see Chapter III), when investigated in dry nitrogen atmosphere.

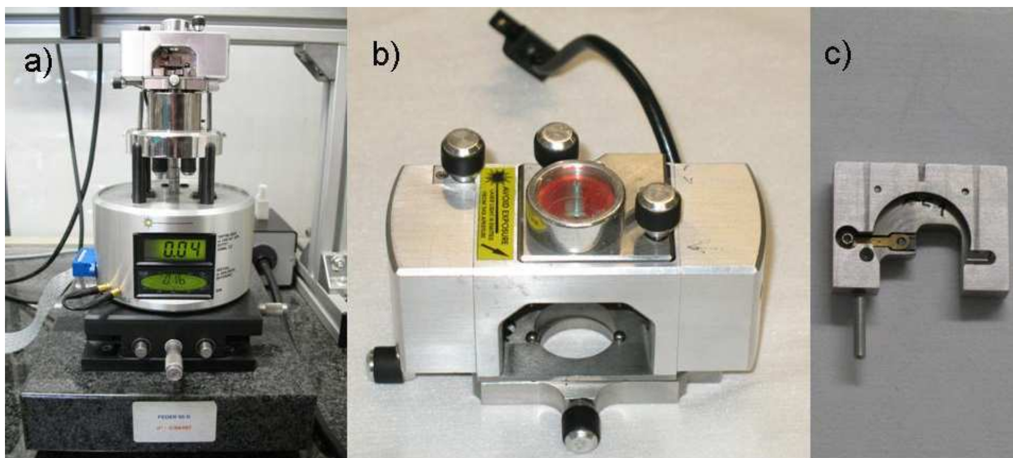


*Figure 1.20 Multimode microscope and equipment: a) main unit with anti-vibrating table, b) head with laser, photodiode and piezoelectric for tip actuation, c) cantilever holder.*

## 1.5.2 Description of the Dimension microscope (Veeco Instruments)

In this system, the sample is fixed, and the cantilever with all the AFM instrumentation is scanning above the surface, which enables the Dimension microscope to

accept samples with large size. Our Dimension system is working with a Nanoscope IV controller. Images with size up to 100×100 μm$^2$ in lateral (x,y) scale and 6.2 μm in vertical (z) direction can be acquired. This system has been used for tapping-mode imaging of samples with nanowires in air (see Chapter II).

*Figure 1.21 Dimension microscope and equipment: a) main microscope with anti-vibrating table, b) controllers, c) support for cantilever.*

### 1.5.3 Description of the Variable Temperature (VT) AFM (Omicron Nanotechnology)

The UHV-VT AFM microscope is designed for measurements in the UHV range $10^{-10}$ mBar (which is reached by a combination of pumps: rotary pumps, turbo pumps, titanium sublimation pumps and ion pumps). This microscope consists in three main chambers: the microscope chamber, the preparation and analysis chambers, as well as a load-lock to make quick sample transfers into vacuum [38]. Our VT-AFM is installed in a first floor at IEMN, and is both internally suspended, and since recently externally suspended using an active pneumatic system (IDE). The microscope can operate both as an AFM or STM. The VT contains cooling and heating facilities. The sample cooling is achieved using a liquid helium or liquid nitrogen as cryogenic fluids in a flow cryostat, leading to minimum temperatures of 25 K or 95 K respectively, on the sample. This system cannot however be considered as a cryogenic AFM system, since *(i)* only the sample is cooled (the cantilever cannot benefit from the reduction in kT as for the minimum detectable force gradient defined previously); *(ii)* the cooling is obtained in an open-geometry, leading to significant drifts at low temperatures. The VT sample holder limits the sample size to 10×5 mm$^2$ and 2 mm of thickness, with a maximum scanning area of 10×10 μm$^2$. The z-extension of the scanner is 2 μm. This microscope has been used for the

experiments described in Chapter II and Chapter III of the manuscript, as well as for the data shown in Annexes B and C.

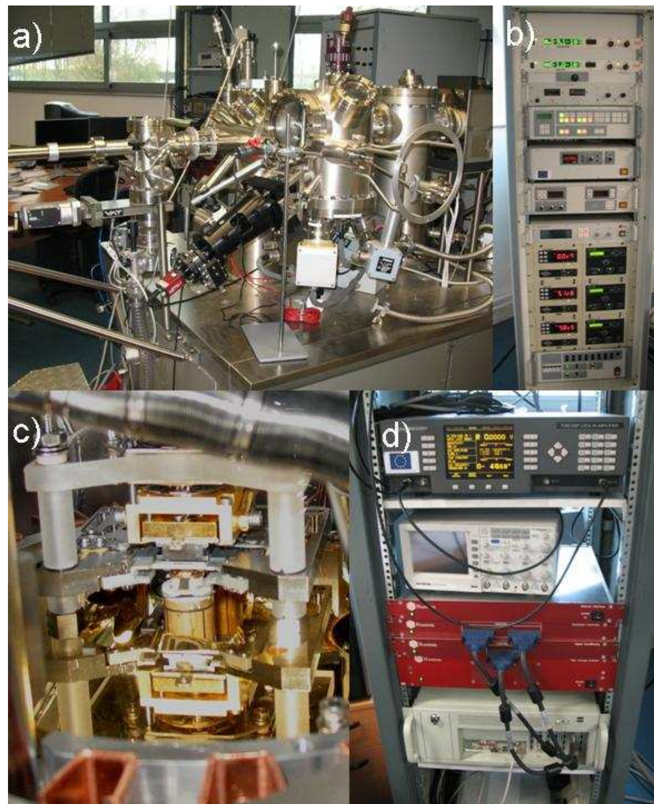


*Figure 1.22 VT-Omicron microscope and equipment: a) main microscope, b) controllers for vacuum and pumps, c) head inside microscope with mounted tip and sample, d) lock-in and controller.*

## 1.5.4 Cantilevers

The following cantilevers have been used for our experiments, depending on the mode (contact, tapping, etc.) or environment (air, vacuum):

- in case of **contact mode measurements** (Chapter II): *n*-doped silicon conical tip ($n \sim 2*10^{19}$ $cm^{-3}$) provided by Omicron Nanotechnology, with force constant of 0,2 N/m; Pt-Ir coated silicon conical tip from μ-mash with spring constant 0,63 N/m; silicon-nitride DNP-20 pyramidal tip from Veeco, with four cantilevers and different force constants 0,12 N/m, 0,58 N/m, 0,32 N/m, 0,06 N/m.

- for both **non-contact and EFM/KFM measurements** (Chapter III): NSC19/Ti-Pt cantilevers from μ-Mash, with resonance frequency 80 kHz and spring constant 0,63 N/m; Pointprobe-plus PPP-EFM from Nanosensors with Pt/Ir coating.

# References:

[1] *"Nanotechnology in Europe"* - Robert Podgórzak, **Cases of Science,** 11, 94 (2003)

[2] The Feynman talk can be found e.g. at: http://www.zyvex.com/nanotech/feynman.html

[3] *"Quantum dots for live cells, in vivo imaging, and diagnostics"* - X. Michalet, F. F. Pinaud, L. A. Bentolila, J. M. Tsay, S. Doose, J. J. LI, G. Sundarwsan, A. M. Wu, S. S. Gambhir, S. Weiss, **Science,** 307, 5709, 538-544 (2005)

[4] "*Near-infrared fluorescent type II quantum dots for sentinel lymph node mapping*" - S. Kim, Y. T. Lim, E. G. Soltesz, A. M. De Grand, J. Lee, A. Nakayama, J. A. Parker, T. Mihaljevic, R. G. Laurence, D. M. Dor, L. H. Cohn, M. G. Bawendi, J. V. Frangioni, **Nature Biotechnology,** 22, 93 (2004)

[5] *"Single-exciton optical gain in semiconductor nanocrystals"* - V. I. Klimov, S. A. Ivanov, J. Nanda, M. Achermann, I. Bezel, J. A. McGuire, A. Piryantiski, **Nature**, 447, 441-446 (2007)

[6] *"Air-stable all-inorganic nanocrystal solar cells processed from solution"* - I. Gur, N. A. Former, M. L. Geier, A. P. Alivisatos, **Science,** 310, 462-465 (2005)

[7] www.wikipedia.org

[8] *"Scanning tunnelling microscopy"* - G. Binnig, H. Rohrer, **Surface Science,** 152-153, 1, 17-26 (1985)

[9] *"Identification of atomic-like electronic states in indium arsenide nanocrystal quantum dots"* - U. Banin, Y. Cao, D. Katz, O. Millo, **Nature,** 400, 542-544 (1999)

[10] *"Can scanning tunnelling spectroscopy measure the density of states of semiconductor quantum dots?"* - P. Liljeroth, L. Jdira, K. Overgaag, B. Grandidier, S. Speller, D. Vanmaekelbergh, **Physical Chemistry Chemical Physics,** 8, 3845-3850 (2006)

[11] *"Interpretation and theory of tunneling experiments on single nanostructures"* - Y. M. Niquet, C. Delerue, G. Allan M. Lannoo, **Physical Review B,** 65, 165334 (2002)

[12] *"Subatomic features on the silicon (111)-(7×7) surface observed by atomic force microscopy"* - F. J. Giessibl, S. Hembacher, H. Bielefeldt, J. Mannhart, **Science,** 289, 5478, 422 – 425 (2000)

[13] *"Charge injection in individual silicon nanoparicles deposited on a conductive substrate"* - T. Mélin, D. Deresmes, D. Stiévenard, **Applied Physics Letters,** 81, 26 (2002)

[14] *“Towards silicon-nanowire-structured materials by the intimate mixing of patterning the solid state and chemical reactions”* - D. Hourlier, B. Legrand, C. Boyaval, P. Perrot, **Journal of Nano Research**, 6, 215-224 (2009)

[15] *“Synthesis of silicon nanocrystals in silane plasmas for nanoelectronics and large area electronic devices“* - P. Roca i Cabarrocas, T. Nguyen-Tran, Y. Djeridane, A. Abramov, E. Johnson, G. Patriarche, **Journal of Physics D: Applied Physics,** 40, 2258-2266 (2007)

[16] *“Atomic force microscopy”* - G. Binning, C.F. Quate, Ch. Gerber, **Physical Review Letters,** 56, 930-933 (1986)

[17] *“Controlled manipulation of nanoparticles with an atomic force microscopy”* - T. Junno, K. Deppert, L. Montelius, L. Samuelson, **Applied Physics Letters,** 66 (1995)

[18] *“Injection et détection de charges dans des nanostructures semiconductrices par Microscopie à Force Atomique”* Thesis by Raphaelle Dianoux (2004)

[19] *“Self-assembled DNA networks and their electrical conductivity” –* L. Cai, H. Tabata, T. Kawai, **Applied Physics Letters,** 77, 3105 (2000)

[20] www.nanoworld.com

[21] *“Probing nanoscale dipole-dipole interactions by electric force microscopy”* - T. Mélin, H. Diesinger, D. Deresmes, D. Stiévenard, **Physical Review Letters,** 92, 166101 (2004)

[22] *“Charge, polarizability, and photoionization of single semiconductor nanocrystals”* - T. D. Krauss, L. E. Brus, **Physical Review Letters,** 83, 23 (1999)

[23] *“Electric force microscopy of individually charged nanoparticles on conductors: An analytical model for quantitative charge imaging”* - T. Mélin, H. Diesinger, D.Deremies, D. Stiévenard, **Physical Review B,** 69, 3 (2004)

[24] *“Microscopie à force électrostatique de nanostructures 0D et 1D”* - **Habilitation à diriger les Recherches** by Thierry Mélin (2006).

[25] *“Charge-injection mechanisms in semiconductor nanoparticles analyzed from force microscopy experiments”* - S. Barbet, T. Mélin, H. Diesinger, D. Deresmes, D. Stiévenard, **Physical Review B,** 73, 045318, (2006)

[26] *“Electric force microscopy of individually charged semiconductor nanoparticles”* - H. Diesinger, T. Mélin, S.Barbet, D. Deresmes, D. Stiévenard, **Physica Status Solidi,** 203, 6, 1344-1247 (2006)

[27] *“Charging and discharging processes of carbon nanotubes probed by electrostatic force microscopy”* - M. Zdrojek, T. Mélin, H. Diesinger, D. Stiévenard, W. Gebicki, L. Adamowicz, **Journal of Applied Physics,** 100**,** 114326 (2006)

[28] *"Electrostatic force microscopy study of single Au-CdSe hybrid nanodumbebells: evidence for light-induced charge separation"* - R. Costi, G. Cohen, A. Salant, E. Rabani, U. Banin, **Nanoletters,** 9, 5, 2031-2039 (2009)

[29] *"Selective Growth of Metal Tips onto Semiconductor Quantum Rods and Tetrapods"* - T. Mokari, E. Rothenberg, I. Popov, R. Costi, U. Banin, **Science,** 304, 5678, 1787 – 1790 (2004)

[30] *"Detection of single-electron charging in an individual InAs quantum dot by noncontact atomic-force microscopy"* - R. Stomp, Y. Miyahara, S. Schaer, Q. Sun, H. Guo, P. Grutter, S. Studenikin, P. Poole, A. Sachrajda, **Physical Review Letters**, 94, 056802 (2005)

[31] *"Kelvin probe force microscopy"* - M. Nonnenmacher, M. P. O'Boyle, H. K. Wickramasinghe, **Applied Physics Letters,** 58, 25 (1991)

[32] *"Etude par microscopie à champ proche de matériaux III-N pour émetteurs électroniques planaires"* - Thesis by Sophie Barbet (2008)

[33] *"Springer handbook of nanotechnology"* - B. Bushan (Ed.), **Springer** (2003)

[34] *"Frequency modulation detection using high-Q cantilevers for enhanced force microscope sensitivity"* - T. R. Albrecht, P. Grütter, D. Horne, D. Rugar, **Journal of Applied Physics,** 69, 668 (1991)

[35] *"Amplitude or frequency modulation-detection in Kelvin probe force microscopy"* - Th. Glatzel, S. Sadewasser, M. Ch. Lux-Steiner, **Applied Surface Science,** 210, 84-89 (2003)

[36] *"Kelvin force microscopy at the second cantilever resonance: An out-of-vacuum crosstalk compensation setup"* - H. Diesinger, D. Deresmes, J. P. Nys, T. Mélin **Ultramicroscopy,** 108, 8, 773-781 (2008)

[37] *"Resolution and contrast in Kelvin probe force microscopy"* - H. O. Jacobs, P. Leuchtmann, O. J. Homan, A. Stemmer, **Journal of Applied Physics,** 84, 3 (1998)

[38] *"The VT AFM user's guide & service manual"* - Omicron Nanotechnology

# Chapter II

## Electrical properties of semiconductor nanowires

Semiconductor nanowires (NW's) have attracted a lot of attention in the last decade due to their electronic properties (surface sensitivity, low leakage currents, quantum confinement effects) which make them good candidates as building blocks for electronic nanodevices. This chapter consists in measuring the local electronic properties of silicon nanowires using atomic force microscopy. It corresponds to the initial work done in my PhD, in which the aim was to investigate the electronic properties of these nanostructures using the "simplest" experimental tools derived from AFM (here, conducting-AFM measurements), in an ultra-high vacuum environment.

This chapter is devoted to the investigation of the transport properties of single nanowires as a function of their surface states. It is shown on the one hand that the conduction properties of as-grown intrinsic silicon nanowires are dominated by the presence of gold catalyst residues along their surface, which can be either partially suppressed (*e.g.* by a de-oxidation step), or enhanced (upon heat treatment). A qualitative characterization for *n*-type or *p*-type nanowire doping using amplitude-modulation Kelvin force microscopy experiments is presented in the Annex C, as a counterpart to the KFM doping analysis done in Chapter III, in the case of silicon nanocrystals.

# 2.1 Introduction

## 2.1.1 Synthesis of silicon nanowires

The approaches to create one-dimensional nanostructures can be classified as either *top-down* (one-dimensional nanostructures are obtained from a macroscopic material, for example by lithography [1] and etching [2]), or *bottom-up*: the nanowires are synthesized directly, for example by laser ablation [3], solution-phase synthesis (SPS) [4] or chemical vapor deposition techniques [5].

Bulk quantities of NWs can for instance be produced by Solution-Phase Synthesis (SPS). Holmes *et al.* have fabricated silicon NWs with diameters ranging from 40 to 50 angstroms and length of several micrometers (those sizes allow to see photoluminescence due to quantum confinement) [4]. In this method, size-monodispersed gold nanocrystals were used, so as to direct the NW growth, and obtain nanowires with a given diameter. The gold particles are dispersed in hexane with diphenylsilane as a precursor of silicon. At 800°C and under a pressure of 270 bar, diphenylsilane decomposes into silicon. The phase

diagram for gold and silicon shows that for temperatures more than ~360 °C (eutectic point) these materials can form an alloy. During the decomposition of diphenylsilane, silicon dissolves in gold, until it reaches supersaturation and is expelled from the "gold" nanoparticle and forms a nanowire. The fabricated nanowires have highly crystalline cores, a narrow size distribution, a few µm length and a tunable crystallographic orientation [4].

Another way to obtain nanowires from a catalytic process is the so-called Vapor-Liquid-Solid (VLS) mechanism based on chemical vapor deposition (CVD). This process is obtained at low-pressure (typically from $10^{-3}$ mbar to 1 mbar [5]) and uses a vapor phase for the silicon feedstock (*e.g.* $SiH_4$ or $SiCl_4$). It can be divided into the following technological steps [6]:

1. deposition of a gold thin film (1-10nm) on a silicon substrate;
2. sample annealing at a temperature higher than the gold-silicon eutectic point, leading to alloyed liquid Au-Si droplets;
3. decomposition of the silicon precursor and absorption of silicon into the liquid Au-Si droplet (this process can be obtained above the droplet eutectic temperature);
4. the growth of the solid nanowire occurs when the supersaturation of liquid alloy is reached (see Figure 2.1).

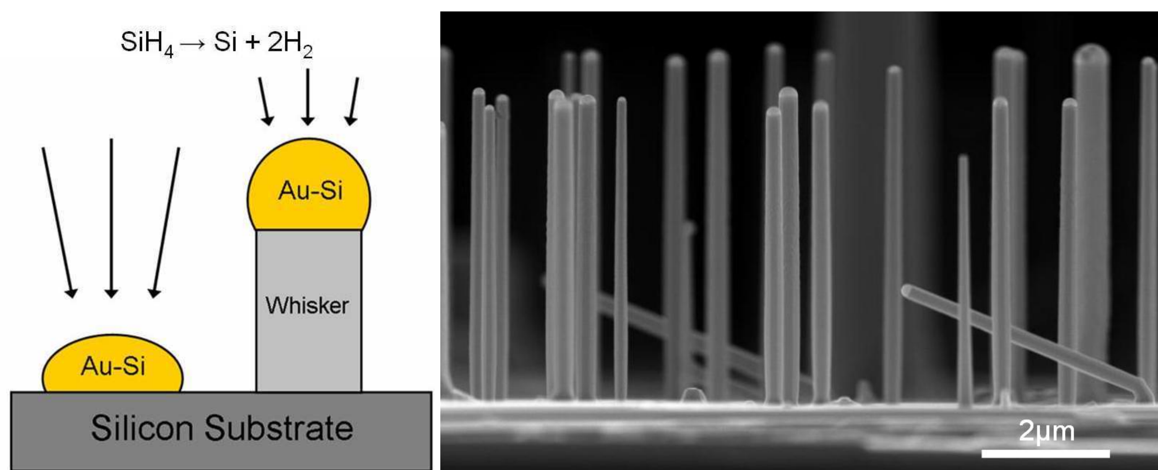


*Figure 2.1 Left: schematics of the VLS growth using a gold catalyst. Right: scanning electron micrograph of silicon NWs, using $SiH_4$ as precursor. Adapted from Ref. [6] and [5].*

The VLS growth can be also used to produce doped silicon NWs by adding to silane gases such as trimethylboron $B(CH_3)_3$ or diborane $B_2H_6$ for *p*-type doping [7]. Lew *et al.* obtained boron concentrations in nanowires ranging from $1\times10^{18}$ to $4\times10^{19}$ cm$^{-3}$ by varying the ratio between the precursor gas used for doping, and silane. It was proved that

NWs doped by diborane have a crystalline core with an amorphous layer coating, while NWs doped by trimethylboron give rise to crystalline structures even at high boron concentration. These differences are attributed to reduced reactivity and higher thermal stability of trimethylboron, as compared to $B_2H_6$.

### 2.1.2 Applications of nanowires

Up to now, prototype devices such as field effect transistors, chemical or biological sensors, and *p-n* junctions have been realized using silicon nanowires.

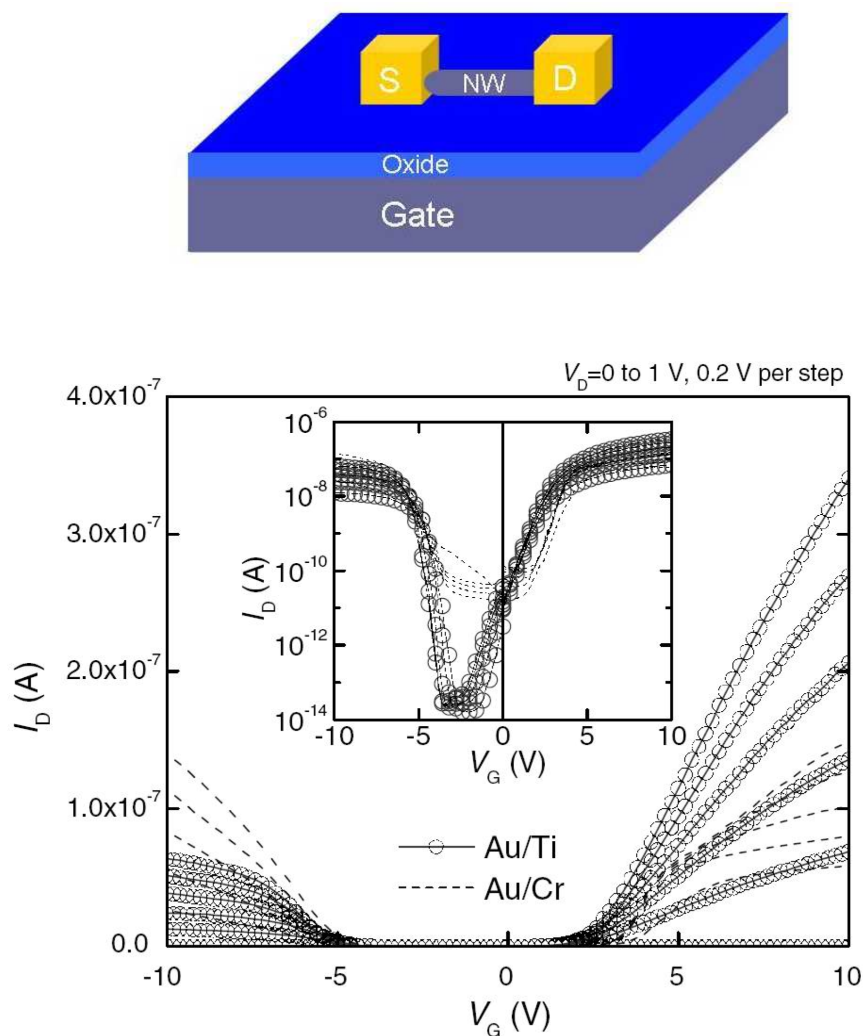


*Figure 2.2 Top: schematics of a nanowire field effect transistor, showing the metal source (S) and drain (D) electrodes, and a nanowire (NW) deposited on an oxidized silicon substrate. Bottom: drain current $I_D$ versus gate voltage $V_G$ characteristics of SiNWFETs measured at room temperature for different source drain metals, Au/Cr and Au/Ti. The inset shows the same data with the drain current on the log scale. Adapted from Ref. [8] and [9].*

Cui *et al.* prepared field effect transistors (FETs) by depositing NWs on an oxidized silicon substrate and contacting their ends as source and drain (Figure 2.2) [8]. The transconductance and carrier mobility of the devices can be improved by contact annealing and/or chemical passivation of the $SiO_x$ shell surrounding the NWs. Such transistors are good candidates as building blocks for future electronics. Similar transistors based on boron-doped (*p*-type) NWs have been used as highly sensitive detectors, by modifying the gate oxide with molecular receptors, allowing the observation of a change of conductance upon binding of charged species [10]. Such transistors can exhibit a sensitivity of a single molecule [10]. The modification of the silicon gate oxide with 3-aminopropropyltriethoxysilane provide sensors which can undergo protonation and deprotonation. Such devices have been tested as pH sensors (*i.e.* they show reversible change in their conductance as a function of pH.), and have been proposed for biology and medical diagnostics (for example as monitors of protein expression). Patolsky *et al.* [11] have shown that silicon NW FETs can be connected as hybrid structures with live mammalian neurons. Each junction can be used for stimulation, inhibition or sensitive detection of neuronal signal propagation. The properties of these hybrid structures allow using them in many purposes, one of the examples being the possibility to develop flexible real-time cellular arrays and use them for drug discovery and testing.

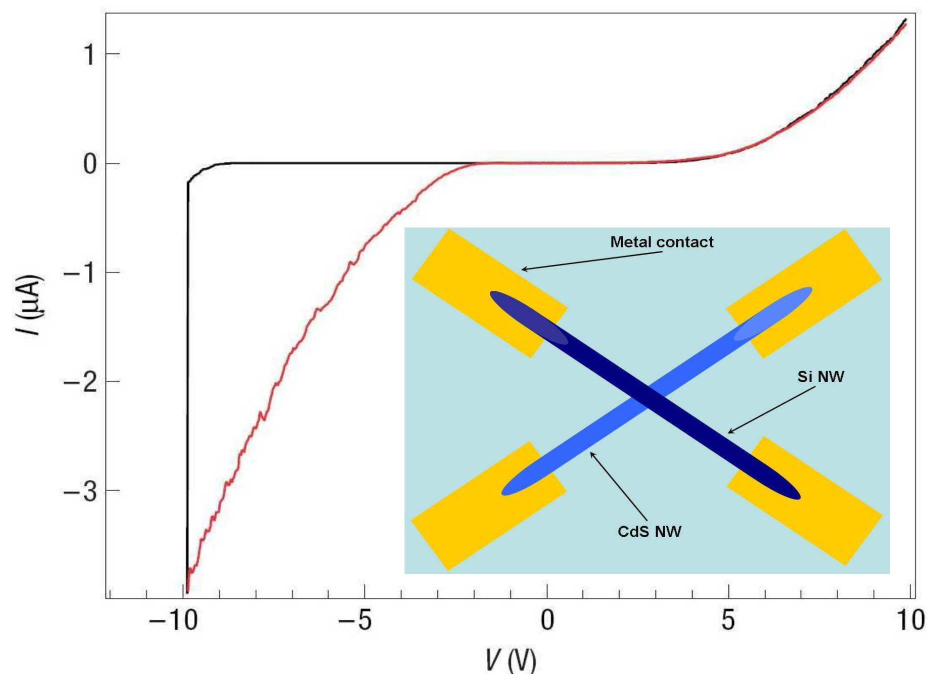


*Figure 2.3 Device with crossed Si and CdS NWs. The NWs form a p-n junction (inset). I–V characteristic of the nanowire avalanche photodiode in dark (black line) and under illumination (red line); the device was illuminated with 500 nW at 488 nm. Adapted from Ref. [12].*

Nanowires also bring new opportunities in the field of energy storage and energy conversion. There is for instance nowadays a great need to invent lithium batteries with high energy capacity and long life cycles. One bottleneck is the change in silicon anode volume (by 400%) because of the insertion and extraction of lithium, which severely limits existing devices by causing their pulverization. Chan *et al.* proposed silicon NW batteries based on VLS growth on stainless steel, which do not exhibit pulverization symptoms, reveal short lithium insertion distances [13], and exhibit higher capacitances than other forms of silicon[1].

Nanodevices based on NWs can also provide high quality devices. NW *p*-*n* junctions have been produced (here by "top-down" etching process [14]) and show an enhancement in their breakdown voltage. *p*-*n* junctions made from *n*-CdS and *p*-Si NWs have been used as "nanophotodiodes" [12], which can detect around 75 photons, are sensitive to the polarization of light, and can be assembled into arrays. Such achievements show that nanowires can play an important role in functional (opto-)electronic nanodevices.

### 2.1.3 Nanowire properties - surface states and transport

Since nanowires have a large potential to be used in devices, it is essential to understand their properties like electrical transport and surface states.

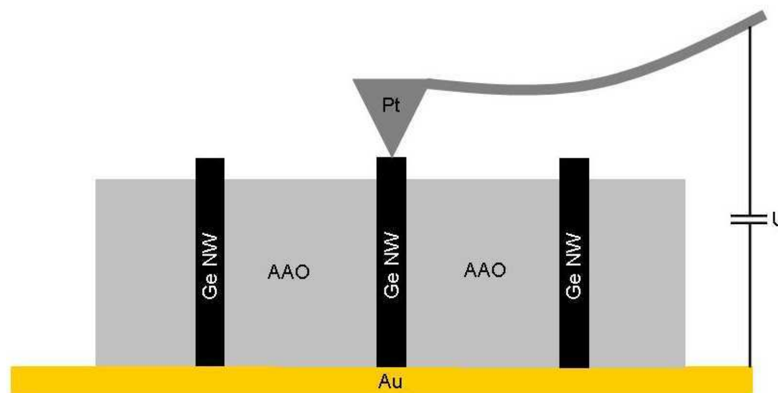


*Figure 2.4 Schematics of germanium nanowire arrays within anodized aluminum oxide, and their measurement by conducting atomic force microscopy.*

Atomic Force Microscopy can be used to measure local I(V) characteristics along nanostructures, by "conducting AFM" (C-AFM). Erts *et al.* used C-AFM to determine the

[1] Despite this advantage, the fabricated Si NW anodes show an irreversible capacity loss after their first cycle.

electrical transport through individual germanium NWs grown in anodized aluminum templates (Figure 2.4) [15]. Results from C-AFM have been compared with macroscopic contact measurements, taken from large numbers of NWs within the array, and show that nanowires can be addressed by their ends using C-AFM.

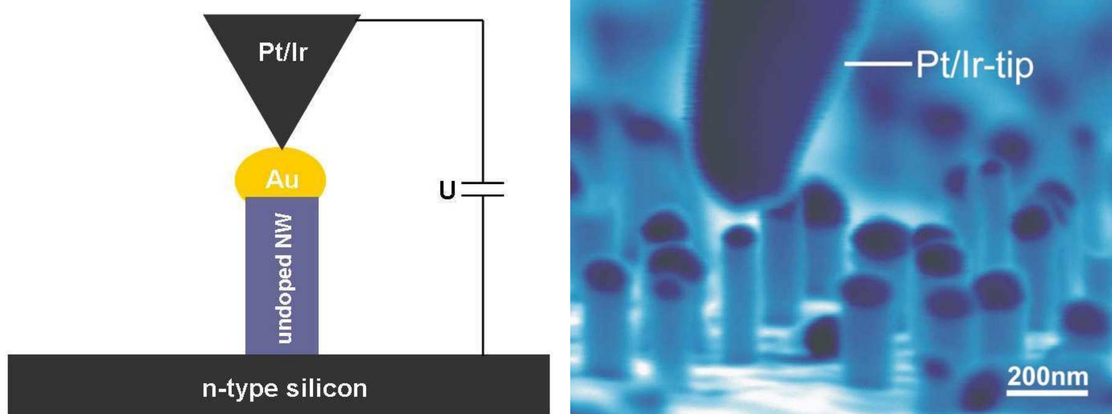


*Figure 2.5 Left: setup for the electrical measurements containing a metal tip, the gold catalyst droplet on the undoped nanowire, and the n-type doped substrate. Right: SEM image of the Si NWs and the Pt/Ir tip. The dark hemispheres on the top of the wires are gold droplets. From Ref. [16].*

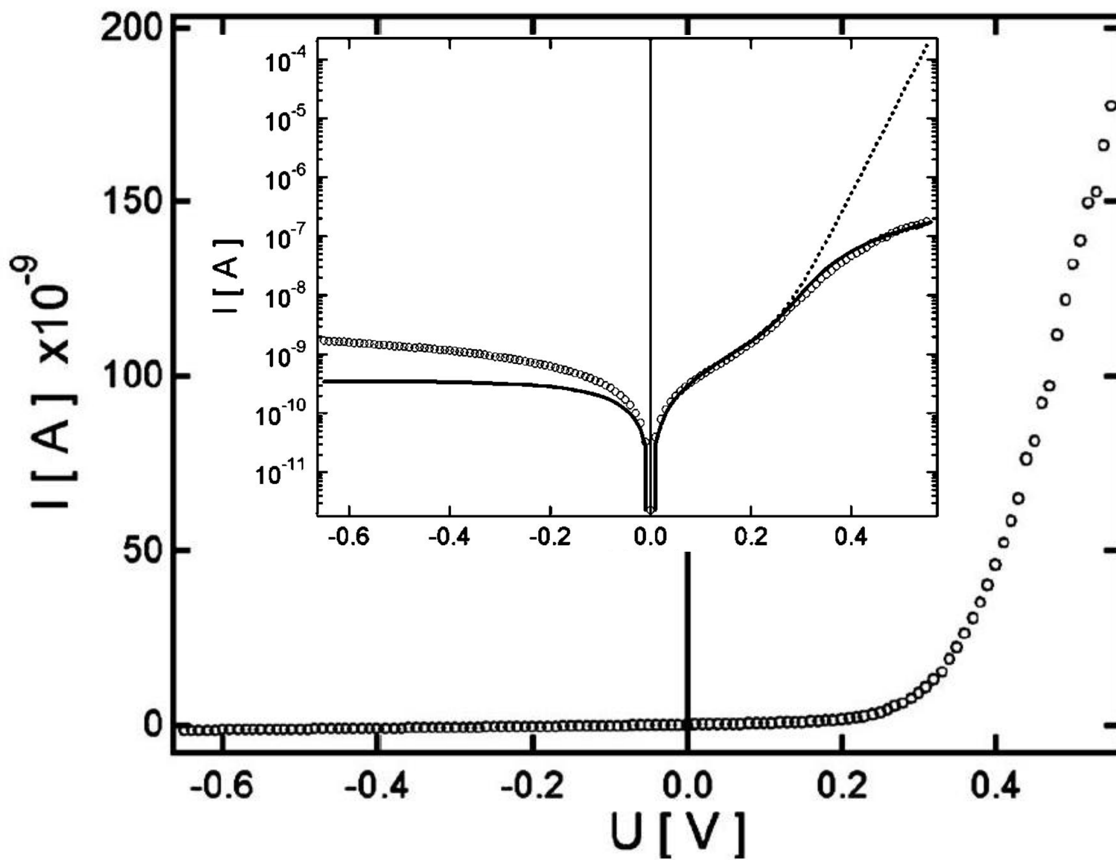


*Figure 2.6 Current-voltage characteristics of an undoped silicon NW in linear scale and logarithmic scale (inset). The fit from the two-diode model is shown without (dotted line), and with (solid line) a resistance correction with $R_s$=1.1 MΩ. Adapted from Ref. [16].*

Bauer *et al.* have presented electrical measurements of undoped silicon NWs grown by molecular-beam epitaxy on a highly doped *n*-doped surface [16]. This method consists in the electrical characterization of NWs in a scanning electron microscope, using a metallized (platinum-iridium) tip in contact with the gold droplet (Figure 2.5). The electron beam induced current (EBIC) is used to investigate the voltage drop at the interface between the NW and surface. A diode-like electrical behaviour is observed (see Figure 2.6), which is mainly governed by the junction between the intrinsic NW and the *n*-type silicon. It was considered that a leakage current can pass additionally along the NW native oxide. A two-diode model has been proposed, in which the forward current $I_{NW}$ is given by:

$$I_{NW} = I_{01}\exp\left(\frac{e(U - I_{NW}R_S)}{n_{01}kT} - 1\right) + I_{02}\exp\left(\frac{e(U - I_{NW}R_S)}{n_{02}kT} - 1\right)$$

where e is electronic charge, U is applied voltage, $R_s$ is the series resistance of the NW, $n_{01}$ is the ideality factor of diffusion current and $n_{02}$ is ideality factor of the recombination current, k is Boltzmann's constant, T is temperature (300K), $I_{01}$ and $I_{02}$ are the saturation values for the diffusion and recombination currents. From the fitted $R_s$ value of 1.1MΩ, it was deduced an equivalent resistivity of 0.85 Ω.cm, corresponding to a doping concentration $\approx 10^{16}$ $cm^{-3}$, which is unlikely for an undoped nanowire. This higher electrical conduction has been attributed to the nanowire oxide, shown from transmission electron microscopy to contain gold nanoparticles (Figure 2.7) [16].

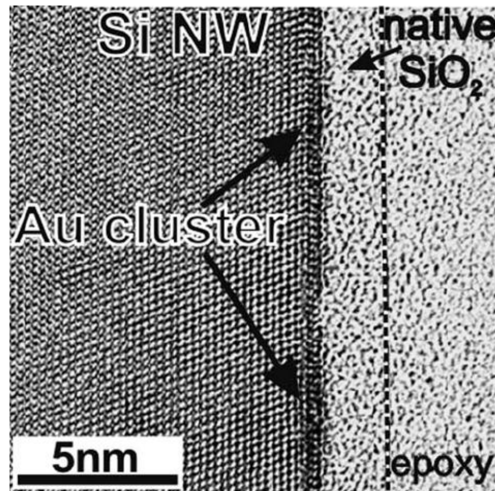


*Figure 2.7 TEM image of the edge of a NW. The dark contrast at the interface between the Si NW and the native $SiO_2$ demonstrates the presence of Au clusters. From Ref. [16].*

The influence of gold has been also analyzed by Chung *et al.* [17]. They produced silicon NWs by VLS using two types of catalyst particles (Au and Zn). NWs were

contacted, so as to measure their I-V characteristics. It was shown that the current through the NWs obtained from Au catalysts is ten times bigger than the current through the nanowires obtained with Zn catalysts, which was attributed to the presence of gold in the oxide.

# 2.2 Experiments

Vertical and tilted silicon NWs have been grown by metal-catalyzed chemical vapour deposition (CVD) on *n*-doped (111) silicon substrates (with resistivity of 0,001-0,006 Ω.cm this corresponds to doping $10^{19}$-$10^{20}$ $cm^{-3}$). The NW characterization has been performed using an atomic force microscopy (AFM) in ultra-high vacuum, with a *n*-doped silicon tip or a Pt/Ir metal-coated silicon tip, and soft spring constant k~0.2 N/m. The electrical transport through individual NWs was measured as a function of the position along NWs, either as-grown, or after etching in hydrofluoric acid, or heat treatments.

## 2.2.1 Intrinsic nanowires

Vertical and tilted silicon NW's have been grown by chemical vapour deposition on a *n*-doped (111) silicon substrate (Figure 2.1, nanowire growth made by D. Hourlier), in which $SiH_4$ was used as gaseous silicon source.

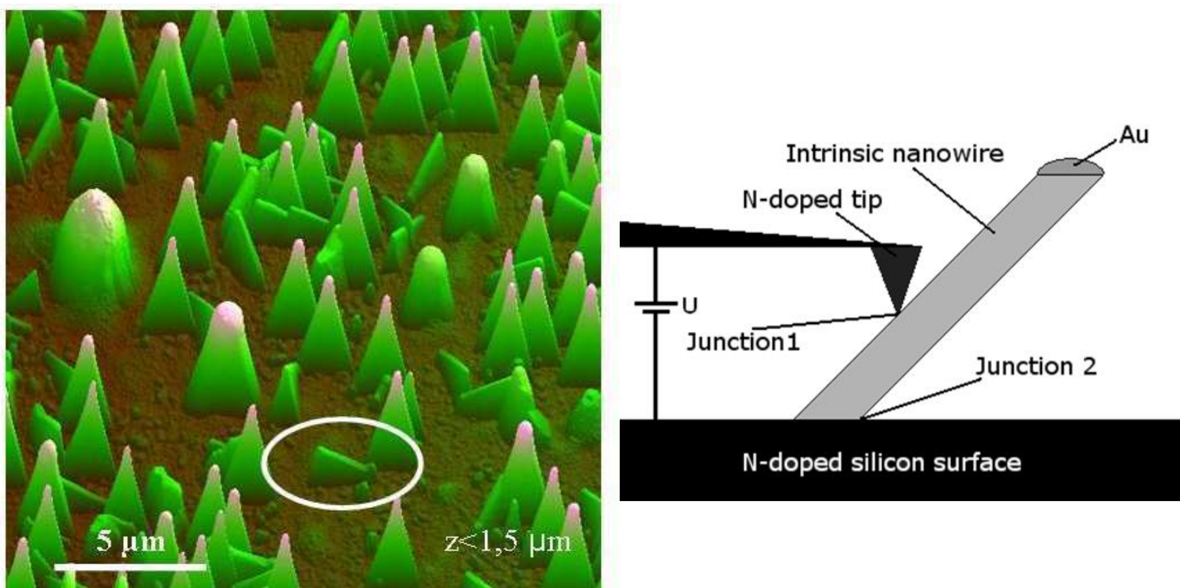


*Figure 2.8 Left: tapping mode image (in air) of silicon nanowires taken using a conical tip. Right: schematics of the local I(V) measurements on a tilted nanowire.*

This process results in (111) oriented nanowires, the vast majority of them growing perpendicular to the substrate, and a fraction of them being tilted. Vertical and tilted nanowires can be dissociated easily in atomic force microscopy images (see Figure 2.8, left) due to tip convolution effects. The aim of my experiments was to take advantage of the tilt of some nanowires, so as to establish local current-voltage measurements along these nanowires (see Figure 2.8, right).

**Analysis of as-grown silicon nanowires**

Current-voltage (I-V) characteristics and maps of current have been measured in ultra-high-vacuum as a function of the position along individual tilted NWs, while imaging the NWs in contact mode. Typical experimental data are shown in Figure 2.9 a (topography of a tilted nanowire) and in Figure 2.9 b (current map, for a tip bias of 1V). This plot shows already that: *(i)* the current is lower on the substrate surface as compared to the nanowire and *(ii)* the current is maximum on the gold catalyst. The current increase on the nanowire, as compared to the substrate, already indicates the presence of gold catalyst residues along NWs.

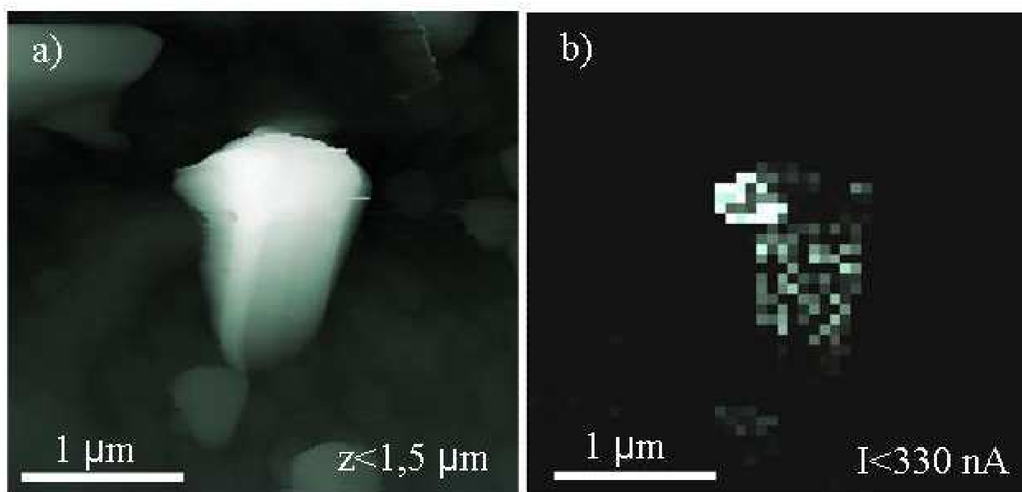


*Figure 2.9 a) Topography image in contact mode. b) Map of current with tip biased to 1V taken simultaneously with topography for an as-grown nanowire.*

The analysis of the current-voltage characteristics taken along the as-grown nanowire of Figure 2.9 are shown in Figure 2.10, both in linear and logarithmic scale. They are labelled from the substrate towards the nanowire top (the gold catalyst is not included in this plot). The I(V) characteristics look almost all proportional, as seen from their shifts in logarithmic scale, but no systematic trend can however be observed when the tip is moved along the nanowire, the current level varying almost randomly with the tip position.

Such variations are typical of conducting AFM measurements through a native oxide, and correspond to local changes in the oxide thickness acting as a tunnel barrier between the tip and sample (see e.g. [18]).

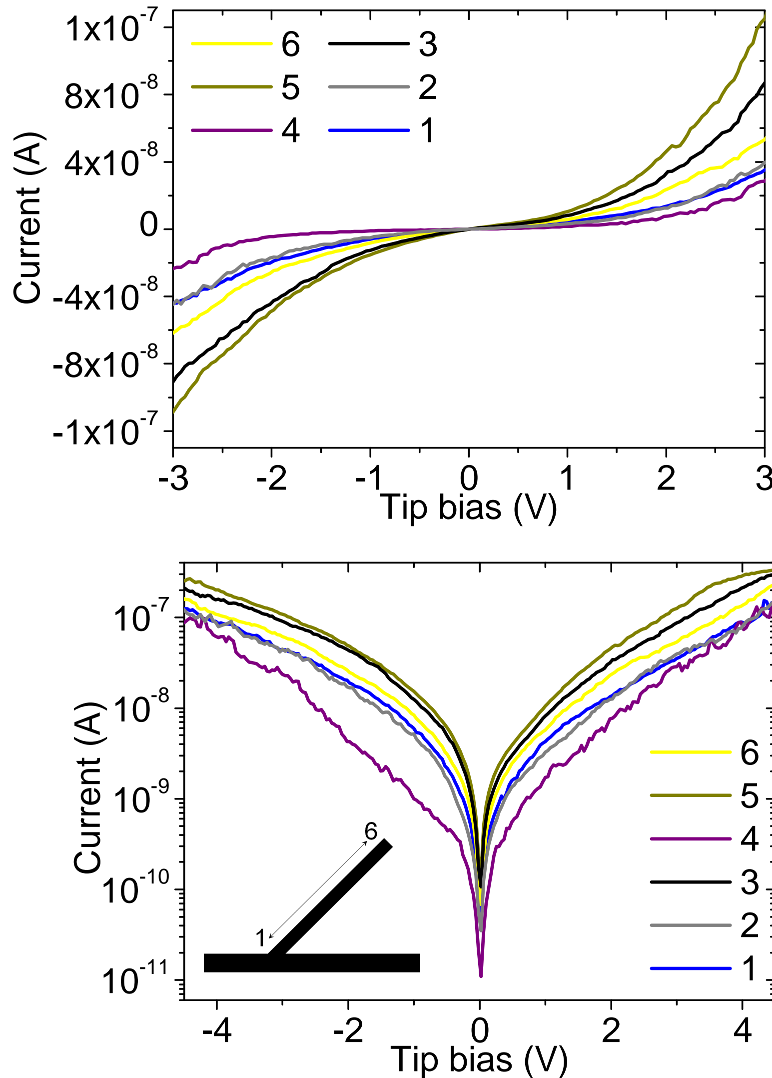


*Figure 2.10 Current-voltage characteristics taken continuously from the bottom (n=1) to the top (n=6) of the as-grown nanowire in linear scale (top) and logarithmic scale (bottom).*

**Analysis of de-oxidized silicon nanowires**

The same sample was measured after etching in a $NH_4F/HF$ solution (buffered etchant BE 7.1) so as to selectively remove the sample native oxide ($SiO_2$ etch rate 1nm/s)[2]. After a 5 second etching, the sample has been washed in deionized water and

[2] We also attempted to use a deoxidized contact-mode cantilever. However, it was not possible to scan the de-oxidized nanowire samples, due to an increased interaction (likely, adhesion force) leading to the nanowire bending during topography imaging.

dried in gaseous nitrogen. A special care was taken to load the sample back in the microscope ultra-high vacuum chamber within less than 10 minutes. Conducting-AFM experiments have been conducted again[3]. Averaged I(V) measurements are first shown in logarithmic scale on the surface and on a nanowire in Figure 2.11, and show that: *(i)* the silicon substrate exhibits an increased conductance as expected after the de-oxidation step; but that *(ii)* the nanowire conductance is decreased after the HF treatment (typically by one decade). This puts forward that the conduction of the intrinsic as-grown nanowires is dominated by a surface conduction through its native "oxide" layer containing gold catalyst inclusions, as in TEM images in Ref. [16].

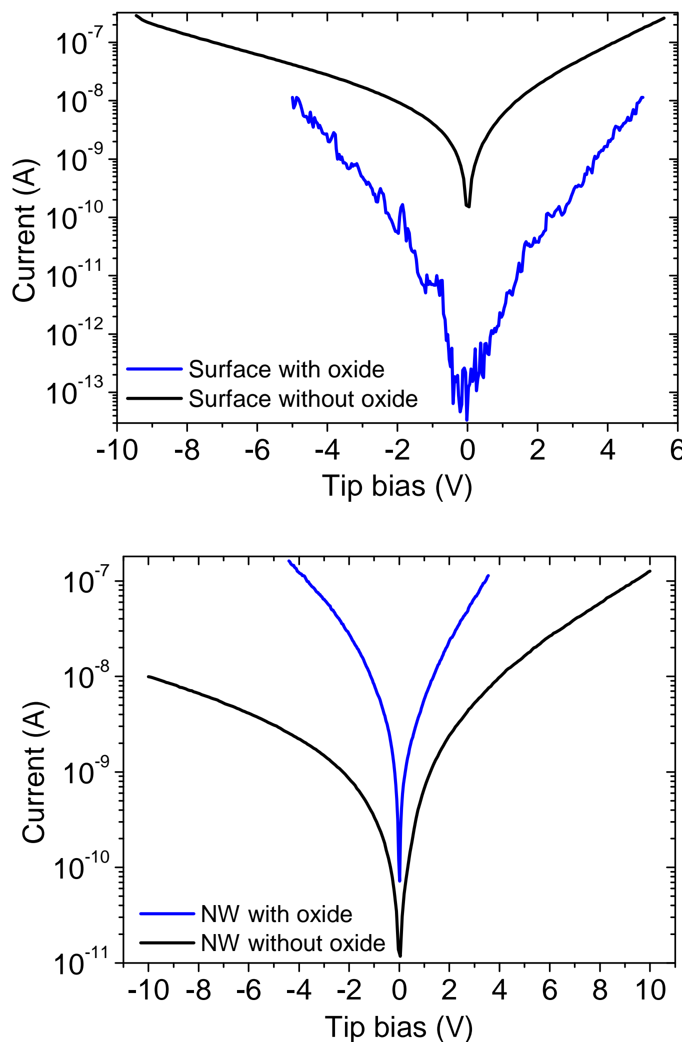


*Figure 2.11 Top: average of current on the sample surface, before (blue curve) and after etching (black curve). Bottom: same plot on the nanowire before (blue curve) and after etching (black curve).*

[3] The experiments shown in Figure 2.10 and 2.12 have not been performed on the same nanowires. It was checked however, from measurements on several nanowires before and after etching, that the I(V) characteristics (shapes, current levels etc) can be indeed compared.

Linear scale local current-voltage characteristics are now presented in Figure 2.12 in linear and logarithmic scale, as a function of the tip position along the nanowire length (the position is labeled from 1 to 7, from the nanowire bottom to the nanowire top). Less current fluctuations are observed when scanning along the nanowire, as seen from the reproducible high-field currents levels in Figure 2.12, as compared to Figure 2.10. This indicates that the nanowire oxide has indeed been etched.

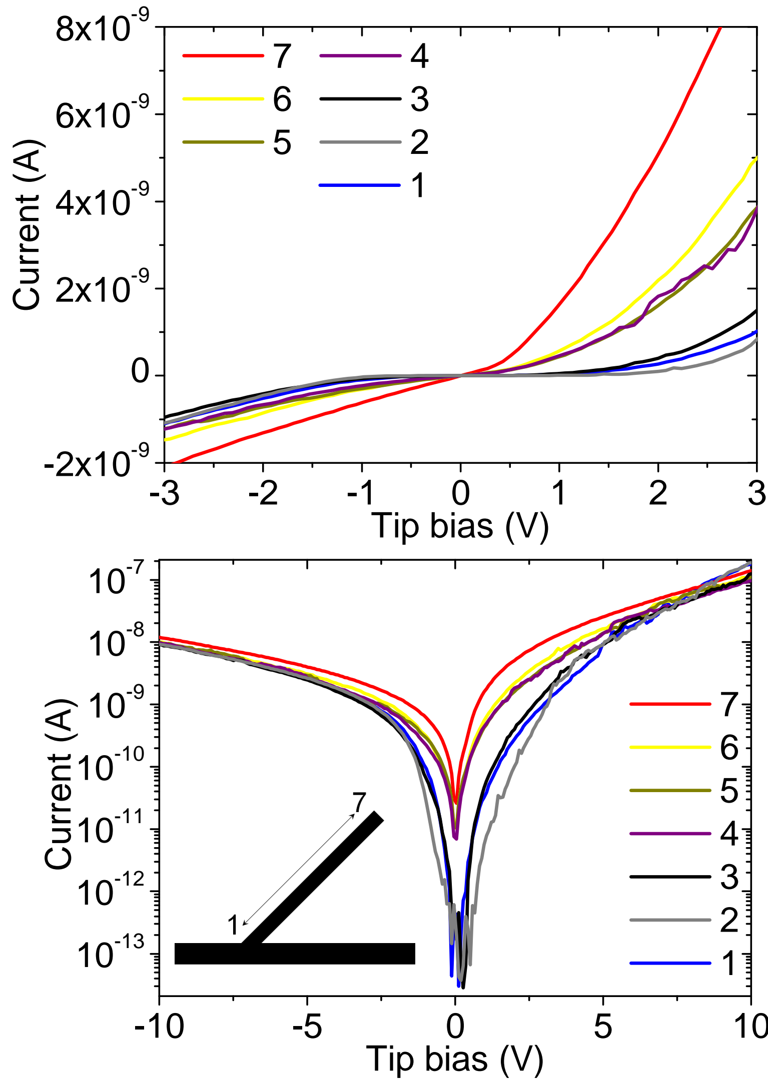


*Figure 2.12 Current-voltage characteristics taken continuously from the bottom (n=1) to the top (n= 7) of a deoxidized nanowire, shown in linear scale (top) and logarithmic scale (bottom). On this plot, it is possible to distinguish two regions along the nanowire at small bias: the nanowire bottom (with a lowest current level ~$10^{-13}$ A corresponding the I(V) amplifier noise) and a second region (towards the gold catalyst droplet) with higher current.*

We furthermore compare now the I(V) characteristics taken along the nanowire (from bottom to top) at small bias $|V_{tip}|<2.5V$ (Figure 2.13). Two regions can now be

observed in Figure 2.13, with either a low conductance (at the nanowire bottom) or a high conductance (on the gold catalyst side). This behaviour is inverse as compared to the naïve expectation that the current should decrease when the AFM tip is moved towards the nanowire end, due to an increased nanowire resistance. It suggests that the high conductance region (nanowire region close to the gold catalyst droplet) must be attributed to gold catalyst residues, still present on the nanowire after the de-oxidation step, and which act to decrease the contact resistance between the tip and nanowire. Following the approach of Ref. [16], we use here the high-conductance region (nanowire bottom) to estimate a lower limit for the nanowire 'intrinsic' resistance of ~2-5.10$^{9}$ Ω. This corresponds to a resistivity of 0.5-1 Ω.cm (taking a nanowire length of 1.5µm and diameter of 200nm, and assuming an ohmic contact at the gold-nanowire interface). This resistivity value would correspond to an equivalent doping concentration of 2-5.10$^{15}$ cm$^{-3}$ (assuming a *n*-type doping with P). These values are found one decade below that of Bauer *et al.* [16], but are here obtained after nanowire deoxidation.

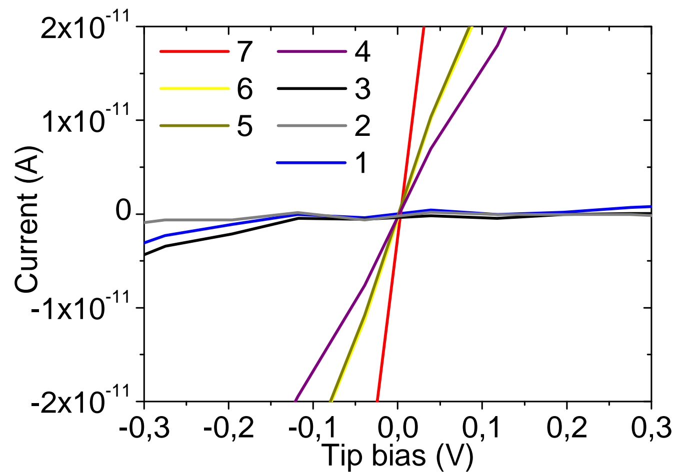


*Figure 2.13 Low-bias I(V) data from Figure 2.12.*

### Heat treatment of nanowires

The influence of heat treatments was also studied in vacuum. The oxide free sample has been heated in vacuum environment at 800 K during one hour, and cooled to room temperature. This step leads to a diffusion of the Au catalyst droplet, as visible from the comparison of the SEM image of Figure 2.14 with respect to as-grown nanowires (Figure 2.1). Average I(V) characteristics are presented, and compared with the as-grown and de-oxidized nanowire data. The gold diffusion is seen to increase the nanowire conduction level, above the level of the as-grown nanowires.

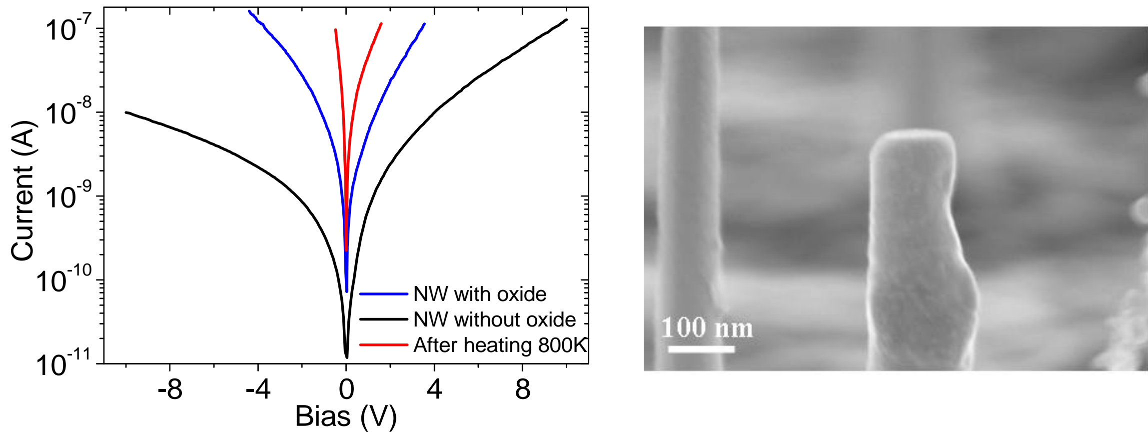


*Figure 2.14 Left: average of current taken from few positions on nanowire, before (blue curve), after etching (black curve) and after heating to 800 K (red curve). Right: SEM image of top of nanowire after heating and spontaneous cooling to room temperature. The "melted" gold droplet is visible on right side of nanowire (see text).*

**I(V) measurements as a function of temperature**

The transport characteristics have been performed as a function of temperature, using here a metal coated tip.

Low temperatures experiments have been performed on as-grown and de-oxidized nanowires, current-voltage characteristics averaged along the nanowire length are presented in Figure 2.15. We start first with the de-oxidized nanowires (Figure 2.15, top), for which the current is seen to drop (typically by 3 orders of magnitude between 300K and 90K), and would correspond to a thermally activated conduction process with energy ~80meV. This behaviour is in qualitative agreement with the transport through a semiconductor, although the interpretation of the thermal activation energy would need to be clarified. The behaviour of the as-grown nanowire is different (Figure 2.15, down). First, it shows more asymmetric I(V) characteristics even at 300K as for the same nanowire sample probed with a doped silicon tip (Figure 2.10). We attribute this to the metal tip (here a Pt/Ir metal plated cantilever tip) used in the experiments of Figure 2.15. The as-grown nanowire transport shows in addition less pronounced variations as a function of temperature (which would correspond to an activation energy of ~50meV). In addition, changes in the shape and curvature of the current-voltage characteristics are observed, at both positive and negative tip bias. We qualitatively attribute these observations to the combined transport properties between the metal-rich oxide layer (for

which the conductivity should increase at low temperatures) and the semiconducting nanowire.

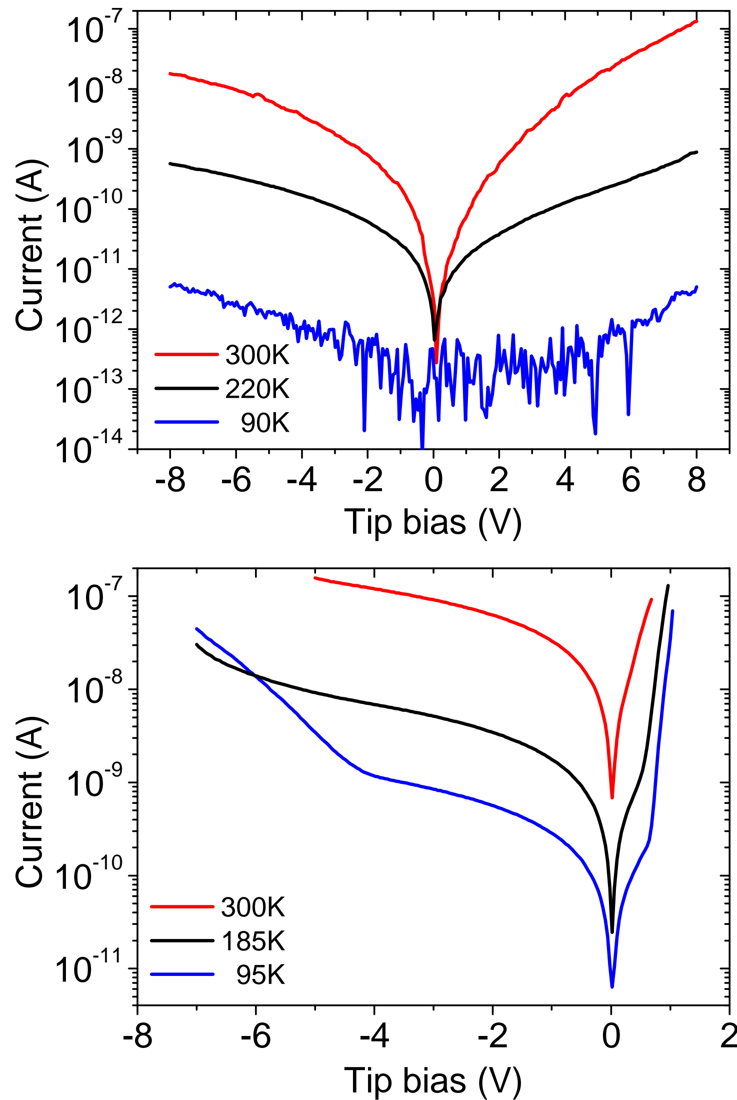


*Figure 2.15 Top: current-bias characteristics taken on nanowire after oxide etching, at 300K, 220K and 90K. Bottom: current-bias characteristics taken on nanowire before oxide etching, at 300K, 185K and 95K.*

## 2.3 Conclusion

The investigation of silicon nanowires by atomic force microscopy in ultra-high vacuum environment brings useful information about their electrical properties. Here we investigated the transport properties of single nanowires as a function of their surface states. It was shown that the conduction of as-grown intrinsic silicon nanowires is dominated by the presence of gold catalyst residues along their surface, which can be either partially suppressed (*e.g.* by a de-oxidation step), or enhanced (upon heat treatment).

# References:

[1] *"Investigation of SiGe-heterostructure nanowires"* - E. Giovine, A. Notargiacomo, L. Di Gaspare, E. Palange, F. Evangelisti, R. Leoni, G. Castellano, G. Torrioli and V. Foglietti, **Nanotechnology,** 12, 132–135 (2001)

[2] *"Study on Thermal Oxidation of Si Nanowires"* - J. L. Liu, Y. Lu, Y. Shi, S. L. Gu, R. L. Jiang, F. Wang, H. M. Bu, Y. D. Zheng, **Physica Status Solidi,** 168, 441 (1998)

[3] "*Si nanowires synthesized from silicon monoxide by laser ablation"* - Y. H. Tang, Y. F. Zhang, N. Wang, W. S. Shi, C. S. Lee, I. Bello, S. T. Lee, **Journal of Vacuum Science & Technology B,** 19, 1 (2001)

[4] *"Control of thickness and orientation of solution-grown silicon nanowires"* - J. D. Holmes, K.P. Johnston, R. C. Christopher Doty, B. A. Korgel, **Science,** 287, 1471-1473 (2000)

[5] *"Towards silicon-nanowire-structured materials by the intimate mixing of patterning the solid state and chemical reactions"* - Djamila Hourlier, Bernard Legrand, Christophe Boyaval, Pierre Perrot, **Journal of Nano Research,** 6, 215-224 (2009)

[6] www.wikipedia.org

[7] *"Structural and electrical properties of trimethylboron-doped silicon nanowires"* - K. Lew, L. Pan, T. E. Bogart, S. M. Dilts, E. C. Dickey, J. Redwing, Y. Wang, M. Cabassi, T. Mayer, S. W. Novak, **Applied Physics Letters,** 85, 15 (2004)

[8] *"High performance silicon nanowire field effect transistors"* - Y. Cui, Z. Zhong, D. Wang, W. U. Wang, C. M. Lieber, **Nanoletters,** 3, 2, 149-152 (2003)

[9] "*Silicon nanowires as enhancement-mode Schottky barrier field-effect transistors*" - S. MoKoo, M. D. Edelstein, Q. Li, C. A. Richter, E. M. Vogel, **Nanotechnology,** 16, 1482–1485 (2005)

[10] *"Nanowire nanosensors for highly sensitive and selective detection of biological and chemical species"* - Y. Cui, Q. Wei, H. Park, C. M. Lieber, **Science,** 293, 1289-1292 (2009)

[11] *"Detection, stimulation, and inhibition of neuronal signals with high-destiny nanowire transistor arrays"* - F. Patolsky, B. P. Timko, G. Yu, Y. Fang, A. B. Greytak, G. Zheng, C. M. Lieber, **Science,** 313, 1100-1004 (2006)

[12] *"Nanoscale avalanche photodiodes for highly sensitive and spatially resolved photon detection"* - O. Hayden, R. Agarwal, C. M. Lieber, **Nature Materials,** 5, 352-356 (2006)

[13] "*High-performance lithium battery anodes using silicon nanowires"* - C. K. Chan, H. Peng, G. Liu, K. McIlwrath, X. F. Zhang, R. A. Huggings, Y. Cui, **Nature Nanotechnology,** 3, 31-35 (2007)

[14] *“Breakdown enhancement in silicon nanowire p-n junctions”* - P. Agarwal, M. N. Vijayaraghavan, F. Neuilly, E. Hijzen, G. A. M. Hurkx, **Nanoletters,** 7, 4, 896-899 (2007)

[15] *“High density germanium nanowire assemblies: contact challenges and electrical characterization”* - D. Erts, B. Polyakov, B. Daly, M. A. Morris, S. Ellingboe, J. Boland, J. D. Holmes, **Journal of Physical Chemistry B,** 110, 820-826 (2006)

[16] *“Electrical properties of nominally undoped silicon nanowires grown by molecular-beam epitaxy”* - J. Bauer, F. Fleischer, O. Breitensten, L. Schubert, P. Werner, U. Gosele, M. Zacharias, **Applied Physics Letters,** 90, 012105 (2007)

[17] *“Silicon nanowire devices”* - S. Chung, J. Yu, J. R. Heath, **Applied Physics Letters,** 76, 15 (2000)

[18] *“Charge-injection mechanisms in semiconductor nanoparticles analyzed from force microscopy experiments“* - S. Barbet, T. Mélin, H. Diesinger, D. Deresmes, D. Stiévenard, **Physical Review B,** 73, 045318 (2006)

# Chapter III

## Electrostatic properties of doped silicon nanocrystals

## 3.1 Introduction

The investigation of the electronic properties of silicon nanocrystals is a very interesting and active field of science because of their remarkable fundamental properties and potential applications in the field of nanoelectronics. Some of these properties and applications will be presented in this chapter.

From an experimental point of view, silicon nanocrystals are a difficult field of investigation as compared to colloidal nanocrystals made from III-V or II-VI elements which are almost free of surface states, and thus allow an easy determination of their optical (*e.g.* colour of luminescence) or electronic (*e.g.* band-structure assessment) properties as a function of their size. There is however a large technological interest to use silicon, because it is the material of microelectronics, and it can thus be introduced at low technological cost into existing fabrication processes. One interest related to light-emitting optical nanodevices is the fact that quantum-confinement is expected to open the band-gap of silicon into the visible range. Another interest, related to the field of biology, is that silicon nanocrystals exhibit also much less toxicity issues as compared to III-V and II-VI materials.

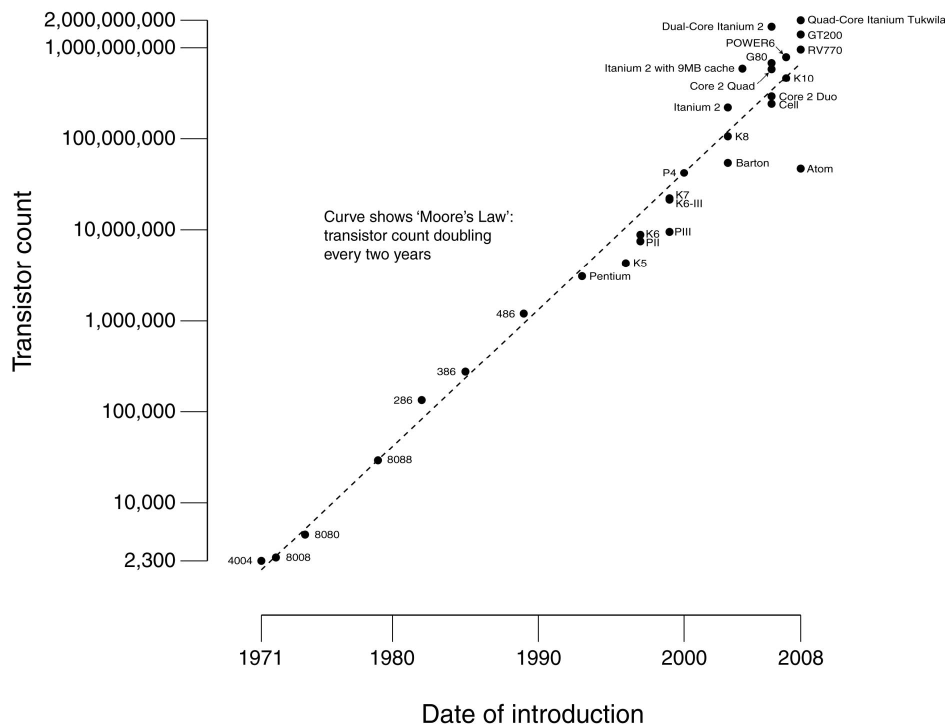


*Figure 3.1 Evolution of number of transistor per one electronic core (transistor count) and Moore's Law (doubling of the number of transistors every two years). From Ref. [1].*

The need to study silicon nanostructures is also obvious from the evolution of the microelectronics industry. This is illustrated in Figure 3.1, showing the shrink in device dimensions and the doubling of number of transistors per electronic core every two years. This graph shows that the electronic industry will reach a regime in which quantum confinement effects become important.

Silicon nanocrystals can therefore play great role in this evolution. A laboratory example of this is the use of nanocrystals in floating gate non-volatile memories [2]. Those devices look schematically like transistors (Figure 3.2), but with a difference with respect to the gate oxide, in which silicon nanocrystals are inserted. To store a bit of information, the source and drain are biased to accelerate carriers in the channel, and a gate potential is applied to achieve a "WRITE" sequence, which allows carriers to tunnel through the oxide and be trapped in the nanocrystals. This stored charge in the gate oxide nanocrystals shifts the voltage threshold of the device. This information can be used as "READ" sequence for the stored bit of information.

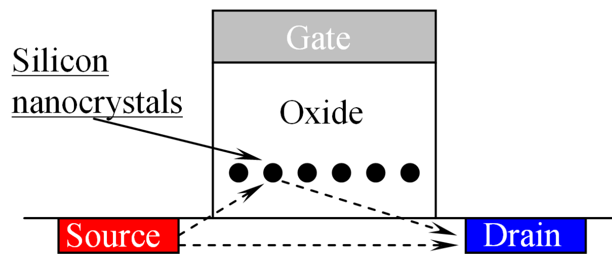


*Figure 3.2 Schematics of a floating gate non-volatile memory device based on silicon nanocrystals.*

Many another applications of silicon nanocrystals have been proposed, such as integrated silicon based light emitting diodes [3] or silicon nanocrystal-based photodetectors [4]. These applications of silicon nanocrystals are probably only the top of the iceberg.

In this chapter, I will in a first step review experiments aiming to detect: electrical transport, quantum confinement, doping levels and surface states of nanocrystals. I will then describe the experimental work done during my PhD, which consisted in probing the electrostatic and electronic properties of silicon nanocrystals (Si-NCs) by ultra-high vacuum KFM.

This chapter is organized as follows: section 3.1 is an introductory description to silicon nanocrystals containing: synthesis, applications, and electronic properties, and

finally a review of experiments on Si-NCs by electrostatic scanning-probe techniques (EFM and KFM). Section 3.2 and 3.3 contains my actual experimental results and their analysis, using numerical simulations of KFM signals. The description of the principle of the numerical calculations has been placed in the Annex A of the manuscript, for sake of clarity.

### 3.1.1 Synthesis of silicon nanocrystals

A great variety of production techniques has been developed for silicon nanocrystals. These methods can differ by the quantity of the produced nanocrystals, their size or their size dispersion. We present in this section a classification of these synthesis techniques with respect to the source of silicon: synthesis from solid sources, liquid sources and gas sources.

**Synthesis of nanocrystals from solid sources**

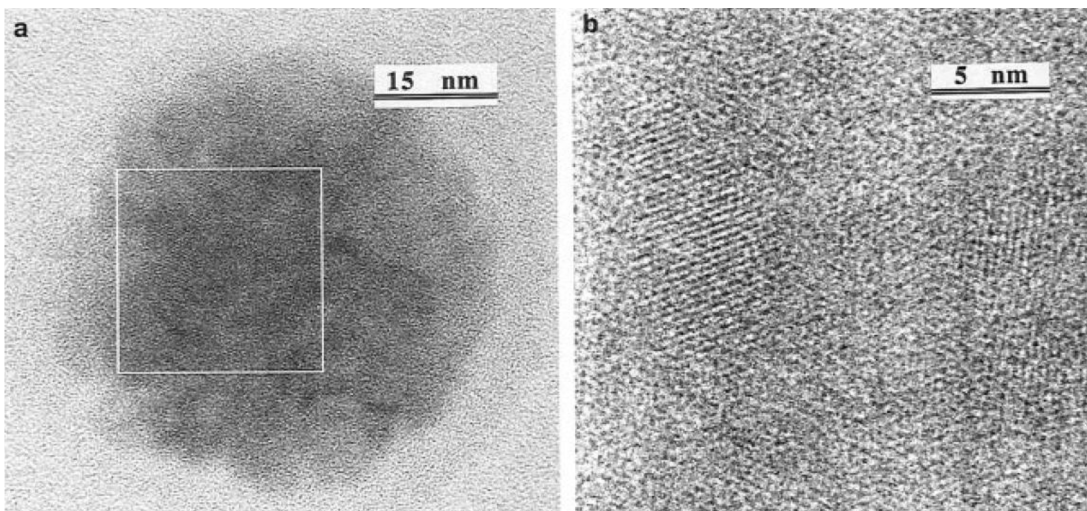


*Figure 3.3 a) High-resolution transmission electron micrograph of a cluster of Si crystallites prepared from porous silicon with an outer amorphous layer between 3 and 4 nm. b) An enlargement of the outline region shown in a), revealing the presence of nanocrystals. From Ref. [5].*

One of the methods of production of nanocrystals from solid source is ultrasonic dispersion of porous silicon, in which a silicon crystal sample is electrochemically etched into porous Si, and afterwards dispersed in a liquid solution like: methanol, toluene, acetonitrile, methylene chloride or water solvents. These processes result in suspensions of

Si nanocrystals. Luminescent crystallites from *n*-type or *p*-type silicon can be achieved using this technique. Numerous scientific works [5][6][7] have been written about silicon nanocrystals made from porous silicon (see transmission electron micrographs in Figure 3.3) and their photoluminescence. Currently, different sizes of the nanocrystals can be obtained by this method in a range between 1 nm up to a few micrometers [1].

B. Legrand *et al.* [8][9] from IEMN made experiments to produce silicon nanocrystals by thermal treatment of thin silicon layers (1-19 nm) on silicon dioxide. The formation of nanocrystals was studied as a function of temperature (500-900 °C). The density and size of the nanocrystals could be regulated from the thickness of the initial silicon layer, in the range from ~500 down to ~10 nanocrystals per $\mu m^2$, starting from a 1.3 nm up to 19 nm thick silicon layer, respectively. The size was found in the range of 5 to 800 nm, depending on the initial silicon thickness layer. This process results however in a noticeable size distribution for the nanocrystals, *e.g.* from 5 to 30 nm in the case of the smallest silicon layer thickness (~1nm) used in the experiments.

Laser vaporization controlled condensation (LVCC) is a process which relies on the coupling of the laser vaporisation of a semiconductor together with a controlled condensation from the vapour phase [10]. This method provides good size control (Carliste *et al.* produced *e.g.* nanocrystals with diameter in range of 5-6 nm). The disadvantage of LVCC, with respect to potential applications, is the small quantities of the produced nanocrystals (less than 1 mg per 24 hours).

To produce a larger amount of nanocrystals, Lam *et al.* first succeeded to do solid phase reactions [11][12]. He used a ball mill to induce reactions of graphite with silicon dioxide powders. After 7-10 days of ball-milling process, 10 g of nanocrystals could be obtained by this technique, however with a wide range of diameter from 1 to 50 nm.

**Synthesis of nanocrystals from liquid sources**

In 1992 Heath [13] proposed a solution phase synthesis of silicon crystals. Later this method has enabled to produce nanocrystals with different terminations of their surface. For this work, reactive Zintl[1] salts were used at mild conditions [11]. It proved

[1] Is a product of a reaction between group 1 (alkali metals) or group 2 (alkaline earths) and post transition metals or metalloids from group 13, 14, 15 or 16.

also here possible to produce larger quantities of nanocrystals (as in the solid-phase method by Lam *et al.*), but with a wider range of diameters, ranging from 5 nm to 3 μm.

English *et al.* [14] tested a mechanism of arrested precipitation in solvents to their critical values of pressure and temperature. Those critical conditions cause the degradation of chemical precursors (like diphenylsilane) to silicon, and a crystallization process starts in the nanocores. Only small quantities of nanocrystals can be produced by this method (0,07 to 1,4 mg of Si nanoparticles per batch of 250-500 mM). Diameters of nanocrystals from 1 to 10 nm were obtained.

**Synthesis of nanocrystals from gas sources**

In the past decade the gas-phase decomposition of silane ($SiH_4$) has been developed to produce nanocrystals. This method relies on pyrolysis[2] of disilane [15] and leads to dilute aerosols of Si nanocrystals. This aerosol is bubbled through ethylene glycol to create colloids. The control of size is achieved from the disilane concentration and (high) temperature of the process, but the distribution of the nanoparticles is rather wide, typically from 1 to 10 nm. This method gives small quantities of collected nanocrystals (less than 10 mg per 24 hours).

Many scientific groups [11] have also explored the synthesis of Si nanoparticles by $CO_2$ laser pyrolysis of silane ($SiH_4$). It is a method which permits to obtain gram-scale quantities of agglomerated silicon nanoparticles, with good control of size and of size distribution (Canon *et al.* [16] first developed this method). Huisken and co-workers [17] ameliorated this process by adapting a pulsed $CO_2$ to obtain luminescent particles.

Another method, which is close to industrial processes in silicon microelectronics, is Chemical Vapour Deposition (CVD), which is widely used to produce thin films of (or containing) silicon nanocrystals. In this process, the substrate is exposed to one or more volatile precursors, which react and/or decompose on the substrate surface to produce the desired deposit [1]. Mazen e*t al.* [18] have developed a two step CVD process which permits to dissociate the nucleation and the growth of silicon nanocrystals. By this technique they obtained nanocrystals of mono-crystalline quality. This process permits to control easily the size of the nanocrystals by modifying the duration of the second step.

[2] Chemical decomposition of condensed organic substances by heating.

The surface density of nanocrystals obtained by this method is ~$3 \times 10^{11}$ nanocrystals per $cm^2$.

Plasma techniques can also be used in conjunction with CVD, in the form of Plasma Enhanced Chemical Vapour Deposition (PECVD) [19]. One of the ways to obtain plasma from reactive gases is to apply an alternating-current (AC) at radio-frequency (RF) in the growth reactor (see Figure 3.4). The nanocrystals investigated in this manuscript have been fabricated using this technique by T. Nguyen-Tran and P. Roca i Cabarrocas, at the "Laboratoire de Physique des Interfaces et des Couches Minces" (LPICM-CNRS, Ecole Polytechnique, Palaiseau). We invite the reader to read the PhD manuscript of T. Nguyen-Tran [20] for a detailed description of the growth processes.

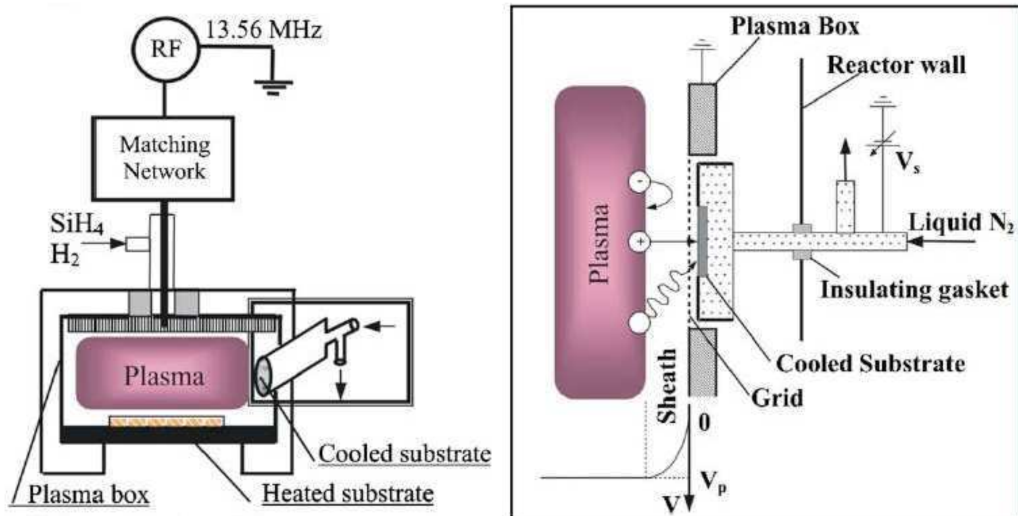


*Figure 3.4 Left: schema of PECVD reactor to fabricate Si nanocrystals. Right: the setup to extract positively charged nanocrystals and to control their kinetic energy. From Ref. [19].*

In our case silane ($SiH_4$) is inserted in the growth chamber, diluted in $H_2$ and Ar (ratios between $SiH_4$:$H_2$:Ar in proportions 1:10:10) for the growth of the intrinsic silicon nanocrystals. *n*-type doping and *p*-type doping are achieved respectively by adding phosphine ($PH_3$) or diborane ($B_2H_6$) in the growth chamber, the doping level being controlled by the flux ratio between $PH_3$ or $B_2H_6$ and silane. Three differently doped *n*-type nanocrystals have been prepared by adding $PH_3$ in the plasma, with phosphine to silane flux ratios of 1/250, 1/50 and 1/25, respectively, leading to a degenerate doping in the range of $10^{20}$-$10^{21}$ $cm^{-3}$. In the case of *p*-type nanocrystals, diborane has been used with a diborane to silane flux ratio of 1/250, leading to a nominal doping level of $10^{20}$ $cm^{-3}$.

As shown in Figure 3.4, the nanocrystals are collected from the plasma phase on the side of the reactor, and using an electrostatic control of the nanocrystal kinetic energy [20]. Nanocrystals can be transferred on any host-substrate, for instance *p*- or *n*-type doped silicon substrates. As shown in Figure 3.5, the deposited nanocrystals agglomerate into "grape-like" structures, with an average nanocrystal density of ≈100/μm$^2$. This density is well-suited to the study of individual nanocrystals. Transmission electron microscopy images (see Figure 3.6) reveal the crystalline properties of the deposited material.

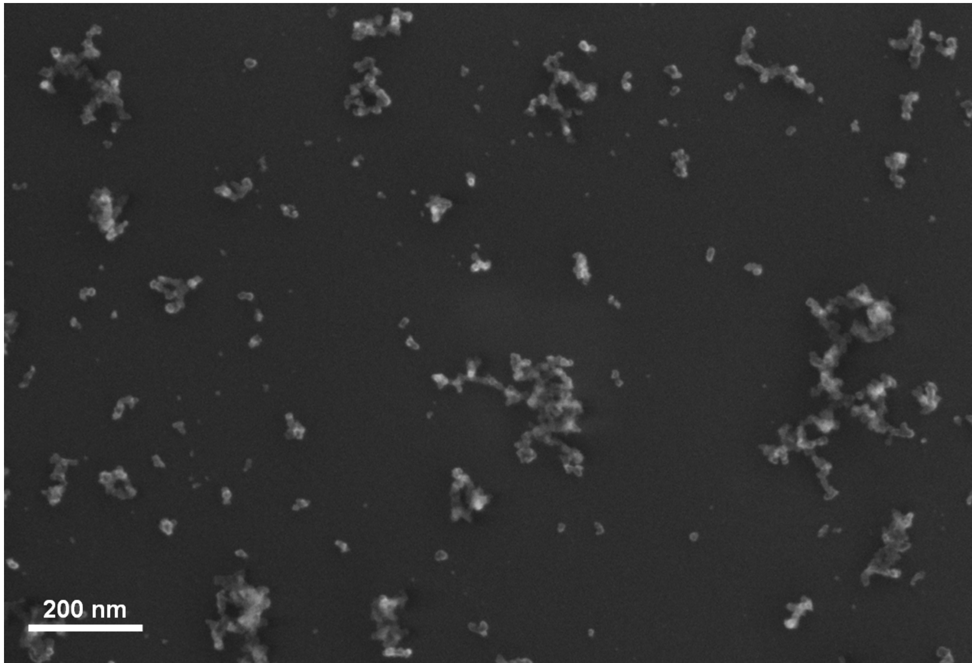


*Figure 3.5 Scanning electron micrograph of silicon nanocrystals fabricated by PECVD.*

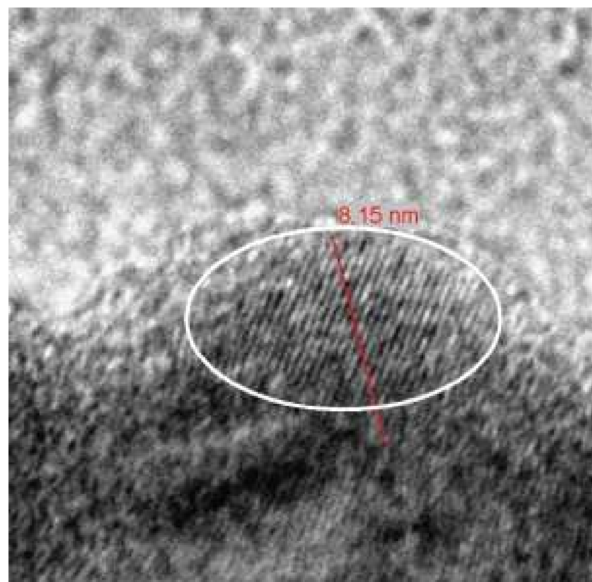


*Figure 3.6 TEM picture of a PECVD silicon nanocrystal with visible atomic planes. From Ref. [20].*

**Size-selection techniques**

To reduce the size distribution of the as-grown nanocrystals, G. Ledoux *et al.* [21] produced size-dispersed silicon nanocrystals with diameters between 2.5 and 8 nm by pulsed $CO_2$ laser pyrolysis of silane, and then found a way to deposit the nanocrystals on a substrate by continuously sweeping the diameter of the deposited nanocrystals along the substrate. This process is based on the different velocities acquired by nanocrystals as a function of the size, making travel of larger nanocrystals slower than small nanocrystals. A rotating molecular-beam chopper has been developed, which is synchronized with $CO_2$ laser as presented in Figure 3.7. The size-selection of the nanocrystals is proved from the nanocrystal photoluminescence (see paragraph 3.1.3) under a 266 nm UV laser irradiation, which reveals the size-dependent spectral photoluminescence shifts associated with quantum confinement.

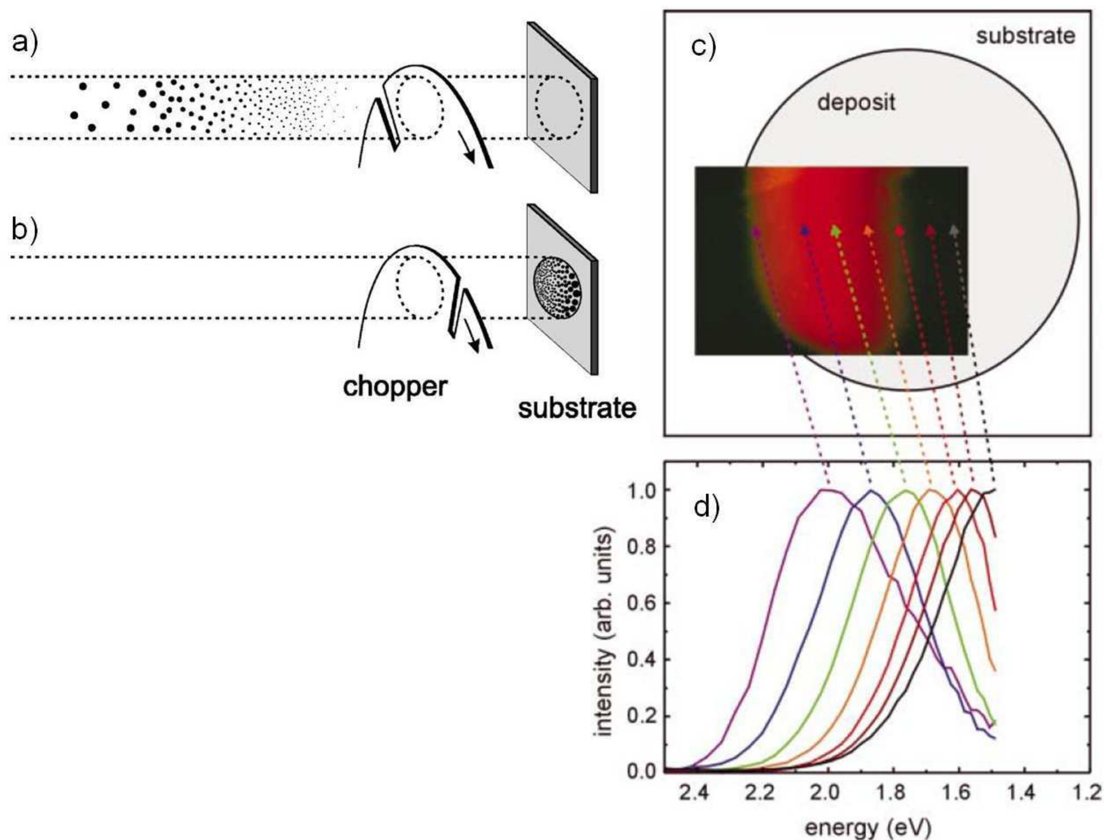


*Figure 3.7 Device to carry out deposition as a function of the nanocrystal size. Bigger nanocrystals have smaller velocity than smaller one. After deposition and light excitation nanocrystals have different photoluminescence properties which depend on their size. The panel a) illustrates the separation of the nanocrystals with different velocities in the pulsed beam. The panel b) reflects the situation in which the nanocrystals have passed the chopper slit. The panel c) shows a photograph of a part of the deposit illuminated by a simple UV lamp. The panel d) reports on the photoluminescence spectra taken at different positions on the deposit as indicated by the arrows.*

**Summary**

The methods to synthesize silicon nanocrystals have been summarized in the following table, and compared as for their “efficiencies”: size and size dispersions, quantity of nanocrystals, and doping possibilities. The PECVD method used here offers *(i)* the possibility to fabricate doped nanocrystals and *(ii)* a rather wide size dispersion range (1-60 nm) which will be exploited in a study of size-dependent charge transfer mechanisms (see section 3.3).

| **Phase** | **Method** | **Size of the nanocrystals** | **Quantity of synthesized nanocrystals** | **Additional comments** |
|---|---|---|---|---|
| **Solid** | **Ultrasonic dispersion of porous silicon** | from 1nm | “large” quantities (of the order of a few mg) | Rather wide size dispersion (e.g. 2-40 nm) possibility to use doped silicon |
| | **Thermal annealing of thin silicon layers** | 5 to 800 nm | 6 to 550 per $\mu m^2$ | Rather wide size dispersion (e.g. 5-30 nm) possibility to use doped silicon |
| | **Laser vaporization controlled condensation** | 5-6 nm | Of the order of one mg | Good size control |
| | **Ball-milling process** | 1-50 nm | 10 g | 7-10 days of synthesis |
| **Liquid** | **Solution phase synthesis using Zintl salts** | 5-3000 nm | Of the order of a few grams | wide size dispersion |
| | **Arrested precipitation of solvents** | 1-10 nm | 0,2 ml per bath of 250-500 mM | |
| **Gas** | **Dilute aerosol of Si nanocrystals** | 1-10 nm | 10 mg per 24 hours | |
| | **$CO_2$ laser pyrolysis of silane ($SiH_4$)** | 2,5 – 8 nm | Gram scale quantities | good control of size |
| | **Chemical vapour deposition** | 1nm | ~3 $\times 10^{11}$ Si-NC/$cm^2$ | |
| | **Plasma Enhanced Chemical Vapour Deposition** | 1-60 nm | ~500 per $\mu m^2$ | Rather wide size dispersion Possibility to produce doped nanocrystals |

## 3.1.2 Quantum confinement

Quantum confinement can be illustrated in the electron effective mass approximation, considering a simplified model of a direct band-gap semiconductor with two parabolic conduction and valence bands of effective masses $m_e$ and $m_h$, placed in an infinite potential well (Figure 3.8). The confinement induces quantum-confined levels inside the potential well, with energy levels defined by the Schrödinger equation. Quantum dots, in which quantum confinement leads to a few quantum-confined electronic states, are sometimes called artificial atoms for this reason.

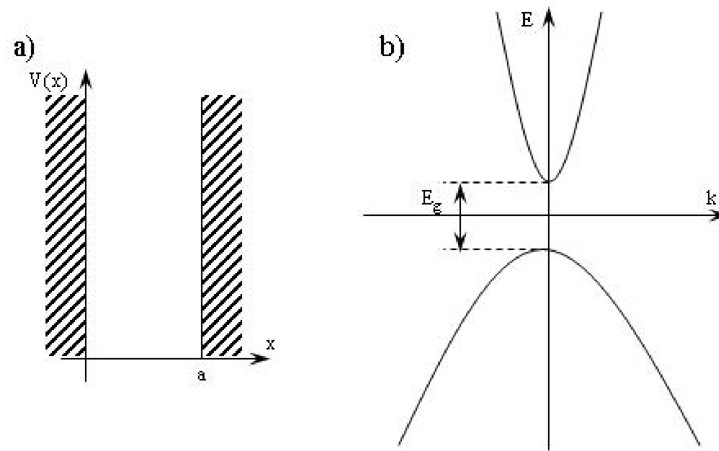


*Figure 3.8 a) Infinite square well potential for a particle in the box. b) Schematics for the conduction and valence bands in the effective mass approximation. From Ref. [2].*

The energy of electrons in the conduction band is $E_c=E_g + \hbar^2k^2/2m_e^*$ and the energy of holes in the valence band is $E_v=-\hbar^2k^2/2|m_h^*|$, where $E_g$ is the bandgap, $\hbar k$ the electron momentum, and the bulk valence band onset is taken as the reference for energies. Since the ground state for a "particle in a box" is $E_{box}= \hbar^2\pi^2/2m^*a^2$ (in which a is width of the well), for a confined system, $E_c^{confined}=E_g+ \hbar^2\pi^2/2m_e^*a^2$ and $E_v^{confined}=- \hbar^2\pi^2/2|m_h^*|a|^2$, leading to $E_g^{confined} = E_g + \hbar^2\pi^2/2a^2 (1/m_e^* + 1/|m_h^*|)$. This increase in the semiconductor band-gap due to quantum confinement (see Figure 3.9) has been one reason why the light emission from silicon nanocrystals has been intensively studied experimentally and theoretically. These nanocrystals where seen as potential structures able to build silicon-based optoelectronic devices like full-colour light-emitting diodes.

Nowadays, it is also possible to affirm that photoluminescence is associated with quantum confinement effects [21]. Niquet *et al.* [22] have presented in 2000 tight-binding

calculations which characterize silicon nanostructures (films, nanowires and nanocrystals) with quantum confinement in a large range of sizes (1-12 nm). By this method they obtained the energy for the onsets of the conduction and valence bands ($E_c$ and $E_v$) in silicon structures like: Si (100) and (110) films, [100]- and [110]- oriented square-based Si wires and cylinders, and for spherical and cubic silicon nanocrystals. We reported here below the phenomenological expressions for $E_v$ and $E_c$ obtained as a function of the characteristic dimension *d* of the nanostructure (see Ref. [22]):

$$E_v(d) = \frac{K_v}{d^2 + a_v d + b_v}$$

$$E_c(d) = \frac{K_c}{d^2 + a_c d + b_c} + E_g$$

where K, a, and b are adjustable parameters, $E_g$=1,143 eV is the bulk band gap. The values for K, a and b are provided here below for spherical, cubic and cylinder-shape nanocrystals:

| Type of nanocrystal | $K_v$ (meV nm$^2$) | $a_v$ (nm) | $b_v$ (nm$^2$) | $K_c$ (meV nm$^2$) | $a_c$ (nm) | $b_c$ (nm$^2$) |
|---|---|---|---|---|---|---|
| **Spherical** | -6234 | 3,391 | 1,412 | 5844,5 | 1,274 | 0,905 |
| **Cubic with (100)×(010)×(001) faces** | -3957 | 2,418 | 0,522 | 4401 | 1,138 | 0,889 |
| **(100) - oriented Si cylinders** | -3448.4 | 2.194 | 1.386 | 2811.6 | 1.027 | 0.396 |

Owing to these formulas, it is possible to plot $E_v$ and $E_c$ for spherical nanocrystals, cubic nanocrystals or cylinder-shape nanocrystals as a function of their diameter (the plot in Figure 3.9 is only for the spherical and cubic nanocrystals, for sake of clarity).

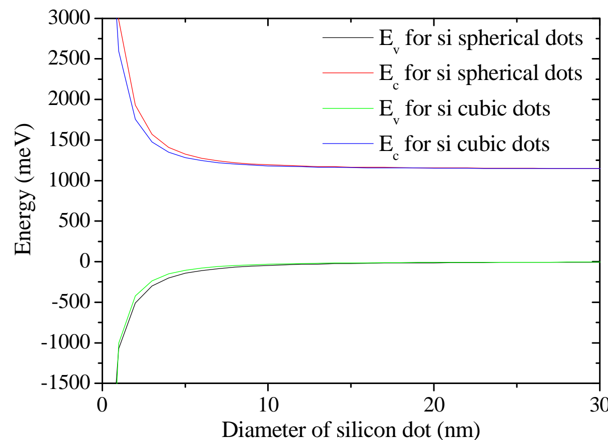


*Figure 3.9 Energy $E_v$ and $E_c$ for spherical and cubic ((100)×(010)×(001) faces) silicon nanocrystals.*

It is clearly visible from these plots that for nanocrystals smaller than 10 nm in diameter, the energy bands will spread out because of quantum confinement. For a nanocrystal with size 10 nm, the confinement energy is between 25 and 45 meV.

### 3.1.3 Photoluminescence and the role of oxygen

The word photoluminescence defines the radiation of photons subsequent to light absorption at higher energy. Canham [23] discovered red photoluminescence in porous silicon in 1990, in spite of the indirect band-gap of bulk silicon. This work has triggered extensive studies of the photoluminescence properties of silicon nanocrystals. For example, Nayfeh *et al.* [24] studied the electrochemical etching of silicon into colloid nanoparticles, which were afterwards reconstituted into films. They detected under 355 nm UV radiation a blue-dominated emission at 390 nm from colloids and film, observable by naked eye. These experiments prove that silicon nanocrystals have light-emitting properties. Their emission color due to quantum confinement effect depends on their size (see Figure 3.7 and 3.9), of interest to *e.g.* wavelength tunable lasers [25], as mentioned previously.

However, the study of nanocrystal surface states is also important for a better understanding of their electronic and optical properties. The comparison of porous silicon without oxygen and with oxygen has for instance been widely studied by Wolkin *et al.* [6], showing that oxygenated nanocrystals exhibit photoluminescence spectra which are red-shifted with respect to hydrogenated samples. Those two situations have also an influence on the carrier lifetime: a longer photoluminescence decay time occurs in the case of oxygenated samples. To check if these changes are caused by oxide, porous silicon was exposed to vacuum, argon, pure hydrogen, pure oxygen and air environments, but the change in its optical behaviour was observed only after exposure of the samples to air and oxygen.

These results suggest that electron-hole recombination can happen because of local states trapped at oxygen sites (Figure 3.10). The calculation of electronic states of silicon nanocrystals as a function of diameter provides three different situations: *(i)* for nanocrystals with diameter >3 nm, the optical recombination is independent of surface bonds; *(ii)* for diameters between 1.5 nm and 3 nm, the optical recombination involves electron states localized on the Si=O bond; and *(iii)* for smaller nanocrystals, both electron and hole become trapped on oxide.

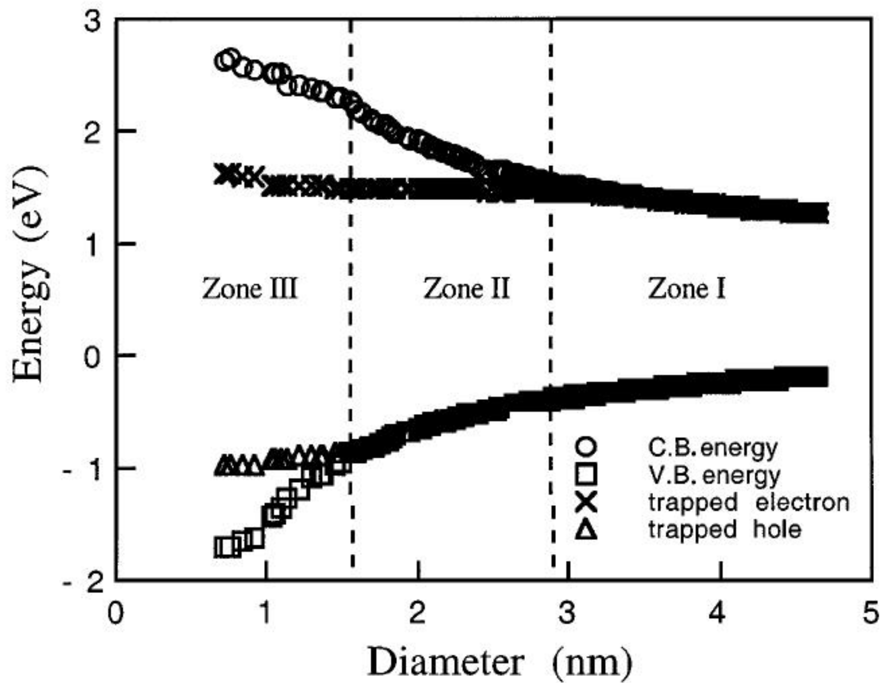


*Figure 3.10 Electronic states in Si nanocrystals as a function of their size and their surface passivation. The origin of energy is that of the valence band in bulk silicon. The trapped electron state is a p-state localized on the Si atom of the Si=O bond and the trapped hole state is a p-state localized on the oxygen atom. From Ref. [6].*

## 3.1.4 Doped silicon nanocrystals

Doped silicon nanocrystals have been studied widely by R. Lechner *et al.* [26], at the scale of thin nanocrystal films. They prepared samples with semiconducting layers made of silicon nanocrystals doped by boron (for *p*-type doping) and phosphorus (for *n*-type doping), see figure 3.11 for SEM images. The nominal doping concentrations are given by the relative gas concentrations: $[B]=2[B_2H_6]/[SiH_4]\cdot 5\times 10^{22}cm^{-3}$ and $[P]=[PH_3]/[SiH_4]\cdot 5\times 10^{22}\ cm^{-3}$. The intrinsic and P-doped (*n*-type) Si NCs have average sizes ranging from 4.3 to 45 nm, while B-doped (*p*-type) Si-NCs of 20 nm in diameter were used. The nanocrystal doping was studied from the conductivity of the nanocrystal films, and as a function of the film laser-annealing, enabling to create interconnected conductive films on the substrate. While the conductivity of the intrinsic samples stays at the level of $\sim 10^{-8}\ \Omega^{-1}cm^{-1}$, the conductivity of *n*-type and *p*-type annealed films exhibits a conductivity above a characteristic threshold of $\sim 10^{-1}\ \Omega^{-1}cm^{-1}$, attributed to the structural changes and melting of nanocrystals, creating a good lateral transport through the films. The nanocrystal film transport has also been studied as a function of the nanocrystal

doping level, both for “low-doping” (i.e. <$10^{19}$ $cm^{-3}$) and highly doped nanocrystals (*i.e.* with a nominal doping in the $10^{20}$-$10^{21}$ $cm^{-3}$ range), corresponding to the doping range of the nanocrystals studied individually in this PhD thesis.

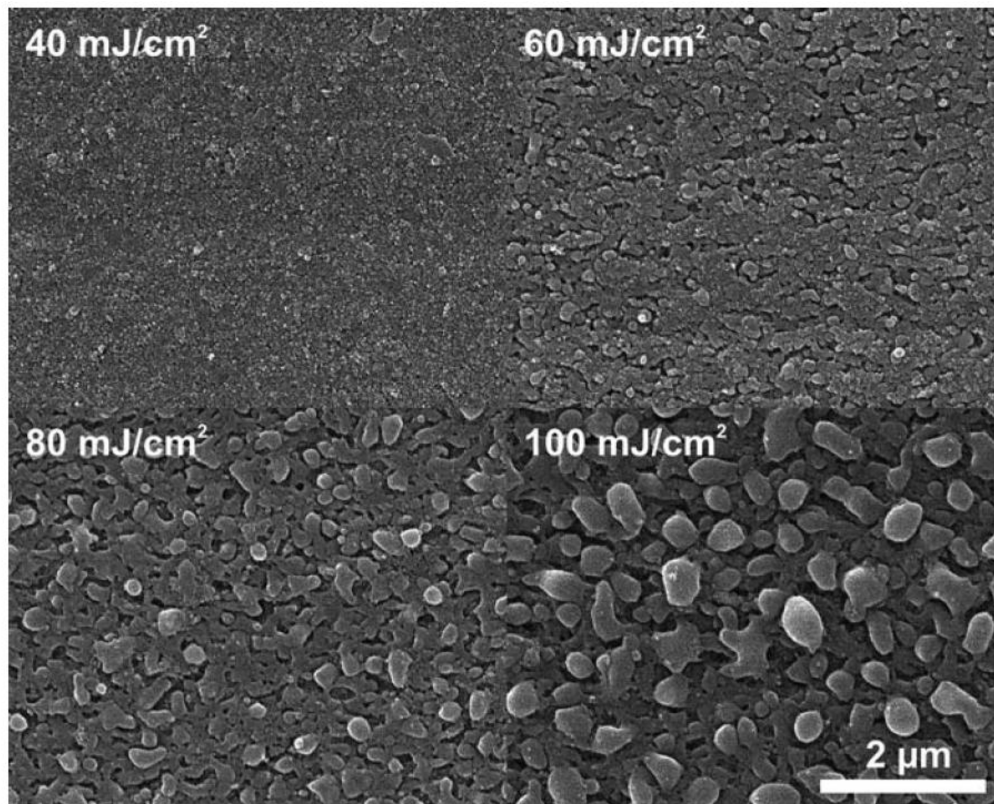


*Figure 3.11 Scanning electron micrographs (top view) of spin-coated films of undoped 20 nm Si NCs, after laser annealing at the indicated energy densities. From Ref. [26].*

### 3.1.5 Scanning probe microscopy experiments on silicon nanocrystals

We will not describe in this section the work done on colloidal nanocrystals or III-V semiconductor quantum dots, which have been widely investigated so far by scanning-tunneling microscopy and spectroscopy experiments, enabling to perform *e.g.* the spectroscopy of the quantum dot electronic levels and to probe the wave-functions of their confined electronic states [27][28] (see *e.g.* the introduction in chapter I). However in this section, we rather focus on scanning probe experiments performed on silicon nanocrystals, for which scanning-tunneling microscopy experiments [29] are not numerous, due to the difficulty to handle passivated silicon nanocrystals on metal surfaces.

Due to the interest of silicon nanocrystals in non-volatile memory device applications, the emphasis has been rather put in characterizing silicon nanocrystals by

electrostatic scanning-probe techniques such as EFM or KFM [2][30][31][32]. In such experiments, the oxide layer surrounding the nanocrystals helps to retain out-of-equilibrium charges and allows the controlled manipulation of its charge state using charge-injection techniques, but may also contribute itself to charge storage [33]. A model has also been proposed to quantitatively measure the charge state Q of individual nanocrystals based on the ratio between their capacitive and charge EFM signals [34]:

$$Q = -3f \frac{\Delta k_{charge}}{\Delta k_{\varepsilon}} \varepsilon_0 \varepsilon \frac{S}{z} V_{EFM}$$

where *f* is a form factor (for hemispherical nanoparticles *f*~0,4), $\Delta k_{charge}$ is the force gradient due to stored charge in the nanoparticle, $\Delta k_{\varepsilon}$ is the force gradient due to the capacitive effect associated with the nanoparticle, $\varepsilon_0$ is vacuum permittivity, ε is the nanoparticle relative static permittivity, S correspond to nanoparticle surface, z is surface tip distance, and $V_{EFM}$ polarization of the tip bias. Based on this model, it was demonstrated that Q~200 charges can be stored in a 40 nm silicon nanoparticle deposited on a conductive substrate, after charge injection with tip biased to <10V and with charge retention times of a few tens of minutes. The value of Q underlines the screening efficiency of the conductive substrate, and the relatively long discharging time constants obtained only with a native oxidation show that silicon nanocrystals are nanostructures of relevance to build nanoscale memory devices.

Until now, only a few publications have used KFM techniques (*i.e.* measurement of surface potentials) to study the electrostatic properties of charged nanocrystals, probably because the relationship between charge states and electrostatic potentials as measured from KFM is not straightforward. Salem *et al.* [35] have presented measurements on charged silicon nanocrystals followed by KFM imaging. They tentatively estimated their charge state and charging energy from the differences in surface potentials obtained before and after charging [36]. Results indicate a charging of ~1 to 3 electrons per nanocrystal, but the validity of the procedure may be discussed, since *(i)* it would fall within the practical limit of charge detection using ambient air atomic force microscopes (see Ref. [37]); and *(ii)* because KFM data in this reference are strongly correlated to the sample topography, which cannot exclude the KFM signals are free from instrumental artifacts.

All the above-mentioned studies show that the investigation of silicon nanocrystals by scanning probe techniques is yet only partially covered. The main difficulty is here the passivation and surface states of the nanocrystals, which can only be circumvented by

ultra-high vacuum experiments, even for electrostatic force measurements. It will be the aim of the following sections to describe such experiments.

## 3.2 Surface potential in air environment – why not possible?

Kelvin probe force microscopy measurements in air can provide undesired artifacts which can make difficulties in establishing correct measurements of the electrostatic properties of nanostructures. Apart from: undesired signals caused by the measurement process itself (for example the use of a lift mode) and a lower sensitivity (because of lower Q factor and larger tip surface distance), described more precisely in the introduction to this dissertation, measurements can be disturbed by such things like native oxide on nanocrystals or by an undesired charging of the sample surface.

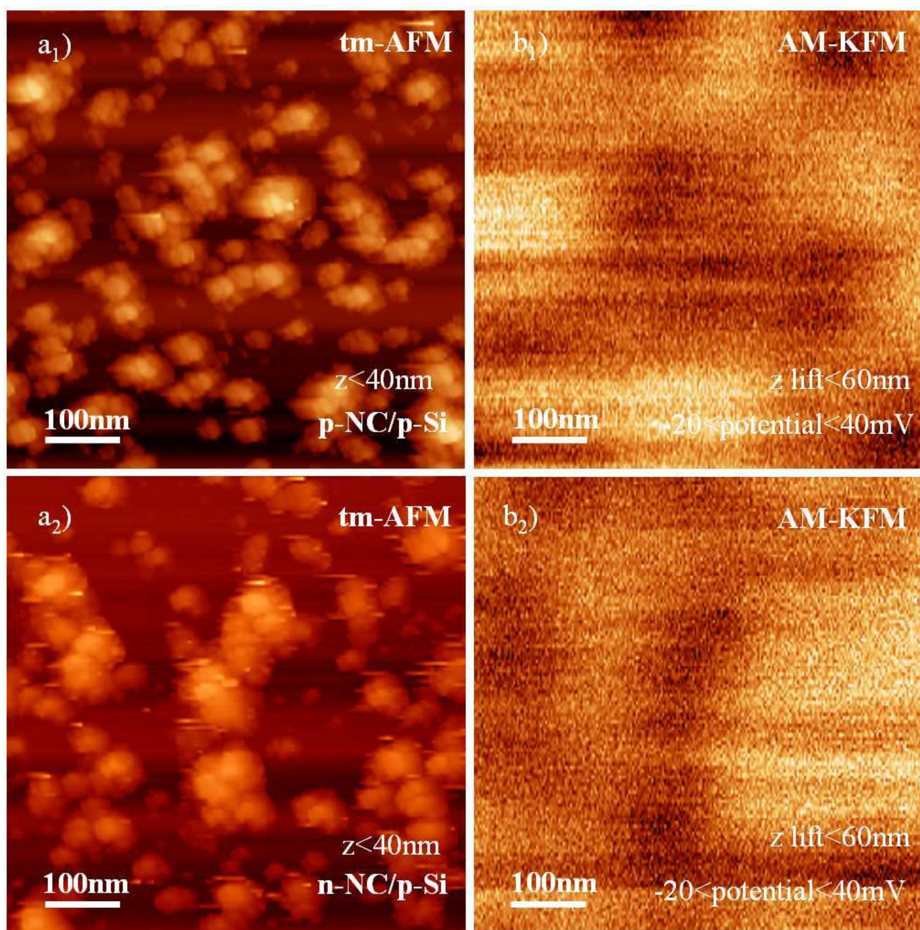


*Figure 3.12 Comparison between p-doped and n-doped nanocrystals deposited on a p-doped silicon substrate. AM-KFM were taken with 60nm linear mode in air using a Veeco system (see chapter I). The z scale in both topography images is 40nm and the surface potential scale in both KFM images is 60mV.*

Because of short time of silicon oxidation (less than 15 minutes) in ambient air, in this environment it is not possible to measure the properties of nanocrystals without oxide. To illustrate the measurements which can be obtained on an ambient air atomic force microscope, we show in Figure 3.12 $a_1$ and $a_2$ the comparison between *p*-type nanocrystals and *n*-type nanocrystals deposited on a *p*-type doped silicon substrate. The corresponding KFM images (here in a linear mode) are given in Figure 3.12 $b_1$ and 3.12 $b_2$. Nanocrystals cannot be individually probed in the surface potential images, because the fairly large tip-substrate distance used in the lift-mode (~80nm) decreases the lateral resolution in KFM. In addition, no significant difference can be observed between the two images, the KFM signal being correlated to the tip-substrate capacitance (which would be increased while scanning over the nanocrystals as *e.g.* in a linear-mode EFM image). These two features make it difficult to extract any relevant information from such ambient air KFM images.

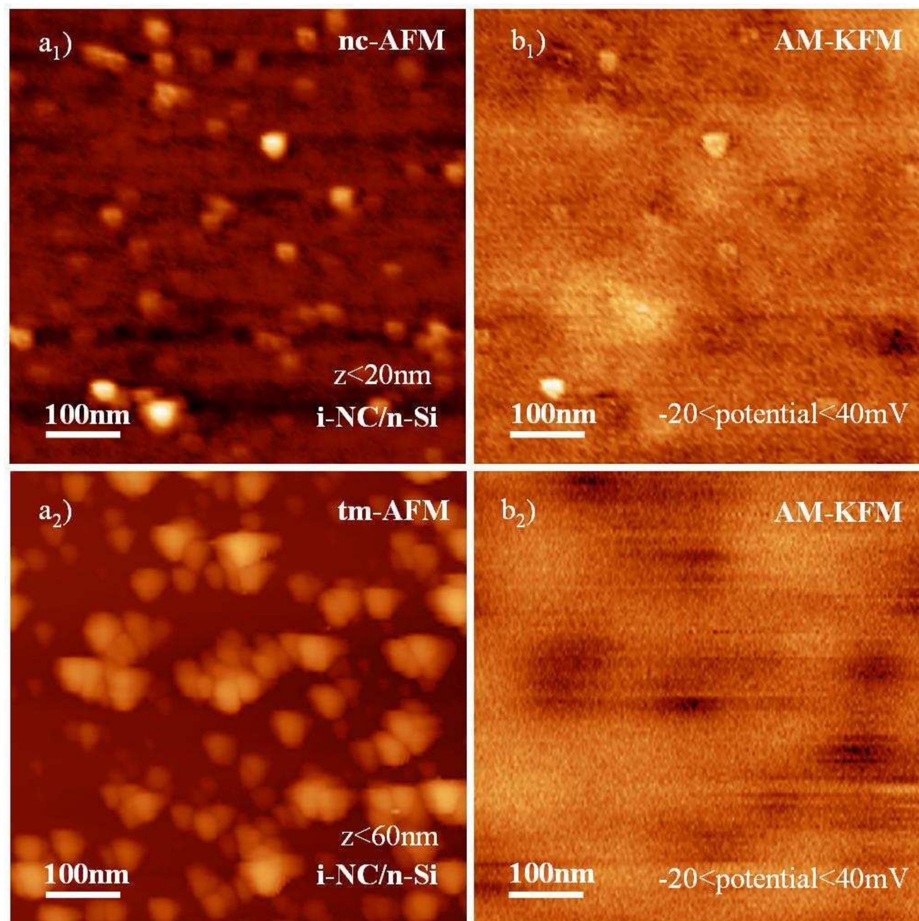


*Figure 3.13 Comparison of intrinsic nanoparticles deposited on n-type surface in vacuum and air.*

We present in Figure 3.13 a comparison between vacuum and air measurements on the same as-grown sample with intrinsic nanocrystals deposited on a *n*-type silicon substrate. No sample treatment has been performed here prior to KFM measurements in

UHV. The two KFM images in air and in UHV are drastically different. First as for the lateral resolution, which is improved due to much lower tip-substrate distance (~20 nm in vacuum in our scanning condition): this enables to probe the surface potential of individual nanocrystals. Then, as for the sign of the nanocrystal surface potential, which stays dominated by a negative signal in the ambient air microscope image (Figure 3.13 $b_2$) while it is *in general* positive in vacuum (Figure 3.13 $b_1$), but also shows a few nanocrystals with a negative charge. This fact excludes that the UHV KFM images are driven by instrumental artefacts.

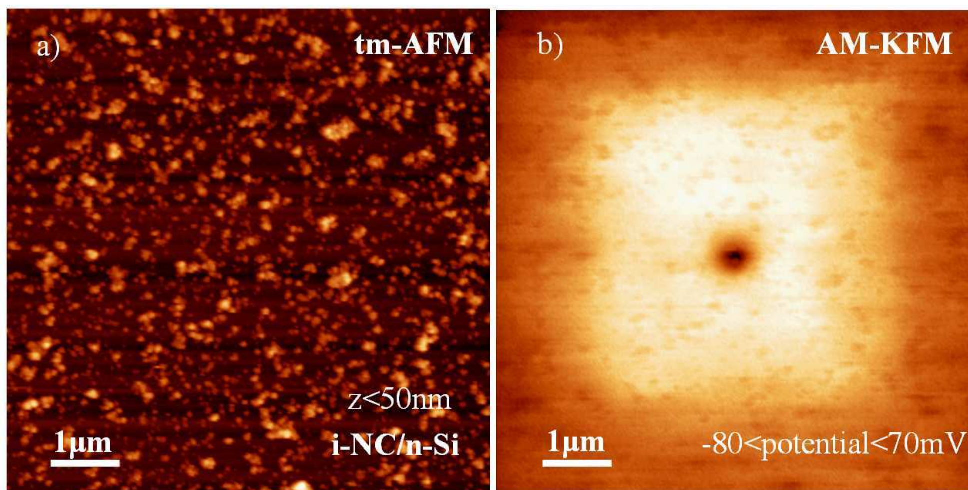


*Figure 3.14 Charging effect induced by a tapping mode. Intermittent contact mode topography a) and lift-mode KFM image b) of a sample of intrinsic nanocrystals. The KFM image shows a central dark spot (due to a charge injection at -12V, see text) and a bright central 5×5µm² area associated with previous topography scans. The AM-KFM image has been taken with scan lift=40nm (lift mode).*

Another problem connected with the presence of a native oxide is the trapping of surface charges. This can be first illustrated from Figure 3.13 $b_2$, in which the surface itself exhibits surface potential variations attributed to local variations in the oxide charge. This fact can become a technical problem in experiments conducted in ambient air or dry nitrogen, since the topography imaging is then performed in intermittent contact mode, and induces a continuous charging of the surface, in contrast with UHV experiments in which the surface is imaged in a non-contact mode. This is visible from Figure 3.14, which shows AFM and KFM images of intrinsic nanocrystals. In this image, a charge injection experiment has been carried out (tip injection bias -12V, see central dark potential spot in the KFM image), followed by two topography scans with size 5×5 µm², and finally a zoom-out corresponds to the images of Figure 3.14. It is seen from the KFM image that the

5x5µm² area has been (positively) charged during the first scans, showing the influence of the intermittent contact mode on the sample surface potential.

## 3.3 Charge transfer from doped silicon nanocrystals

In this section, the ionization of hydrogen-passivated phosphorus-doped and boron-doped silicon nanocrystals on silicon substrates is studied experimentally using Kelvin Force Microscopy in ultra-high vacuum environment. It will be demonstrated that the charge transfer from doped silicon nanocrystals follows an energy compensation mechanism, which is enhanced by quantum confinement. Results put forward the possibility to use doped nanocrystals as electron sources to achieve a controlled remote doping of nanostructures and devices with two-dimensional charge densities in the range of $2\times10^{11}$-$10^{14}$ cm$^{-2}$, or linear charge densities in the range of $8\times10^{5}$-$2\times10^{7}$ cm$^{-1}$.

### 3.3.1 Sample preparation and setup for experiments in ultra high vacuum

Silicon nanocrystals have been fabricated by plasma enhanced chemical vapor deposition, as described in section 3.1.1. The samples studied in this work consist in:

• nominally undoped (intrinsic) reference nanocrystals collected from the plasma chamber, and deposited on *p*-type or *n*-type silicon substrates

• *n*-type doped nanocrystals, deposited on *n*-type and *p*-type silicon substrates;

• *p*-type doped nanocrystals, deposited on *n*-type and *p*-type silicon substrates.

Reference samples will be hereafter labeled *i*-NC/*n*-Si and *i*-NC/*p*-Si, respectively, the *n*-type doped nanocrystal samples on *n*-type and *p*-type wafers will be termed *n*-NC/*n*-Si and *n*-NC/*p*-Si, and *p*-type doped nanocrystals on *n*-type and *p*-type wafers will be labeled *p*-NC/*n*-Si and *p*-NC/*p*-Si. Additionally, three *n*-NC/*n*-Si samples labeled $S_1$, $S_2$ and $S_3$ have been prepared by adding $PH_3$ in the plasma, with phosphine to silane flux ratios of 1/250, 1/50 and 1/25, respectively, with an expected degenerate doping in the range of $10^{20}$-$10^{21}$ cm$^{-3}$ [26][38]. Samples *p*-NC/*p*-Si and *p*-NC/*n*-Si were prepared with flux ratio 1/250 (nominal doping $10^{20}$ cm$^{-3}$), by adding $B_2H_6$ to $SiH_4$. The *n*-Si and *p*-Si substrates have a resistivity of 0,001-0,006 Ω.cm (this corresponds to doping $10^{19}$-$10^{20}$ cm$^{-3}$) and 0,03-1 Ω.cm (this corresponds to doping $2\times10^{16}$-$2\times10^{18}$ cm$^{-3}$) respectively.

The nanocrystals deposited on the surface exhibit a typical grape-like three-dimensional structure (see Figure 3.5), and do not prove stable upon intermittent contact mode or even non-contact mode topography imaging (they stick to the tip, which makes the topography unstable). To avoid this effect, a cleaning of the as-grown sample by isopropanol has been performed, followed by a drying in gaseous nitrogen. This step enables to achieve tapping mode imaging, with reasonably weak instabilities, as seen *e.g.* from the topography images of Figure 3.12. For the ultra-high vacuum experiments, all samples have been hydrogen-passivated in a diluted hydrogen fluoride (HF) in order to de-oxidize the surface and nanocrystals and minimize the influence of surface states. This process consists in dipping the samples in a diluted 1% HF solution during 5 seconds, and a rinsing in deionized water. The samples are subsequently loaded in the ultra-high vacuum chamber of the UHV chamber of the atomic force microscope operated at a base pressure of $10^{-10}$ mbar. A special care was taken to load sample within less than 10 minutes after HF treatment.

The charge state of nanocrystals is probed with a home-made Amplitude-Modulation Kelvin probe (AM-KFM) set-up, interfaced with a Nanonis controller (SPECS Zürich). Metal-plated cantilever tips were used (EFM PPP, Nanosensors), with 25 nm apex radius, and low-resonance frequency ($f_0 \approx 70$ kHz) and spring constant ($k \approx 3$ N.m$^{-1}$). The resonance at $f_0$ is mechanically excited to perform non-contact atomic force topography (nc-AFM) with a typical tip-substrate distance z=20 nm, while the first cantilever harmonic at $f_1 = 6{,}25 \times f_0 \approx 450$kHz is electrostatically excited with a $V_{dc} + V_{ac} \sin(2\pi f_1 t)$ voltage to simultaneously acquire the KFM data. Noting C(z) the tip-sample capacitance, the AM-KFM loop measures the surface potential $V_S$ by regulating the value of $V_{dc}$ so as to maintain at zero the cantilever oscillation amplitude at $f_1$, which is proportional to $dC/dz\ (V_{dc}-V_S) \times V_{ac}$. More details about the KFM set-up are provided in chapter I.

## 3.3.2 Intrinsic nanocrystals as reference samples

We describe first the experimental results obtained on the intrinsic reference samples (*i*-NC/*n*-Si and *i*-NC/*p*-Si). Simultaneously acquired nc-AFM and AM-KFM images are shown for both samples in Figure 3.15 a and 3.15 b, respectively. The upper

(resp. lower) images and schematics in Figure 3.15 correspond to the *i*-NC/*n*-Si (resp. *i*-NC/*p*-Si) samples.

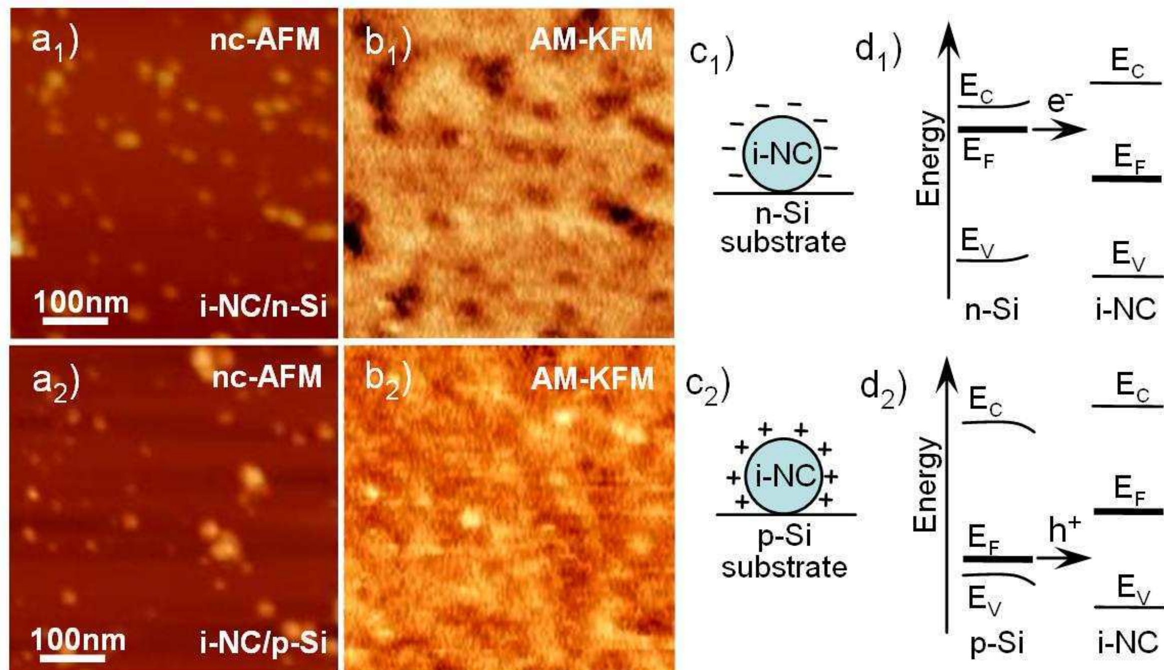


*Figure 3.15 $a_1$) and $a_2$) 500×500 nm² non-contact atomic force microscopy image of hydrogen-passivated intrinsic nanocrystal samples on n-type and p-type doped wafers. The z-scale is 40 nm. $b_1$) and $b_2$) simultaneously recorded amplitude-modulation Kelvin Force Microscopy images. The surface potential scale is 65 mV. $c_1$) and $c_2$) schematics of the charging of the nanocrystal surface states. $d_1$) and $d_2$) corresponding energy diagrams, prior to charge transfer (indicated by the arrows).*

On Figure 3.15 b one can see that nanocrystals appear - *in average* - respectively as dark features (negative potential) and bright features (positive potential) on *n*-Si and *p*-Si, corresponding to negative and positive charge states. This is further illustrated in Figure 3.16, in which the KFM signals are plotted as a function of the nanocrystal height h. KFM signals do not appear correlated to h, but exhibit rather strong fluctuations. We interpret this effect qualitatively as the charging of the nanocrystal surface states by the substrate free carriers. This is schematically illustrated in Figure 3.15 $c_1$ and 3.15 $c_2$, assuming the defects to be localized on the nanocrystal surface. The corresponding energy diagrams are shown in Figure 3.15 $d_1$ and 3.15 $d_2$ for the *i*-NC/*n*-Si and *i*-NC/*p*-Si samples, respectively. The hydrogen-passivated Si substrate is here represented with a Fermi level pinned close to the bands at the semiconductor-vacuum interface. The sign of the charge transfer is governed by the difference between the Fermi levels of the substrate and nanocrystals, as shown in Figure 3.15 $d_1$ and 3.15 $d_2$.

Assuming an intrinsic behaviour for the nanocrystals (*i.e.* with a Fermi level at midgap), this picture accounts for the negative (respectively positive) charge transfer and surface potentials observed *in average* for the i-NC/n-Si and i-NC/p-Si samples. The fluctuations of the surface potentials in Figure 3.16 are accounted by the variation of the actual Fermi level position in the nanocrystals governed by the nanocrystal surface or defect states, in spite of the hydrogen passivation. A few nanocrystals of the *i*-NC/*n*-Si (respectively *i*-NC/*p*-Si) samples are hence even observed in Figure 3.16 with positive (respectively negative) surface potentials.

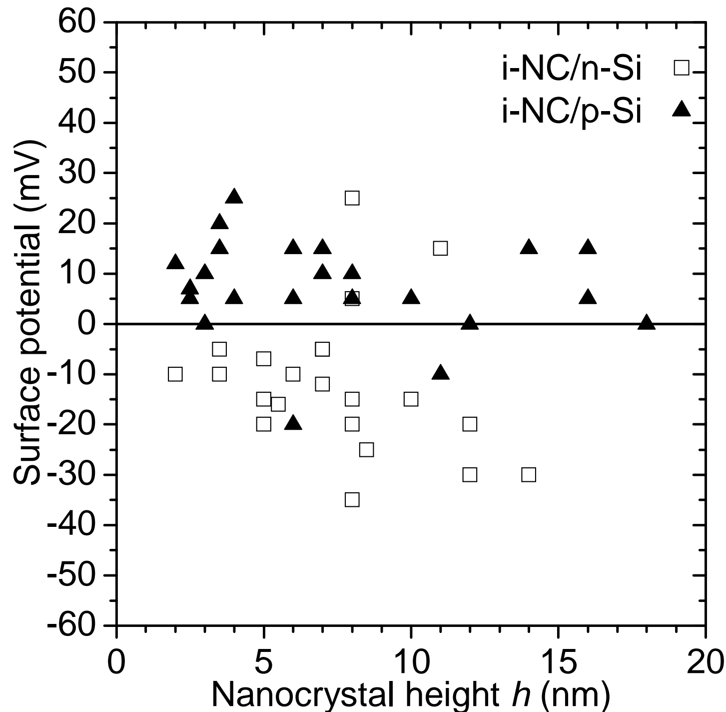


*Figure 3.16 Plot of the surface potentials for the i-NC/n-Si and i-NC/p-Si samples, as a function of the nanocrystal height.*

## 3.3.3 Characterization of *n*-doped nanocrystals

We now analyze KFM signals from the *n*-NC/*p*-Si and *n*-NC/*n*-Si samples. We do not report here on *n*-type doped nanocrystals on *p*-type substrate, which “disappeared” after the sample HF treatment (for unclear reasons, no nanocrystal could be found on this type of surface, in spite of repeated attempts). Thus, only the *n*-NC/*n*-Si samples $S_1$, $S_2$ and $S_3$ will be described, for which nc-AFM and AM-KFM images are shown in Figure 3.17 a and 3.17 b (here for the sample $S_2$), together with a plot of the KFM signals as a function of the nanocrystal height in Figure 3.17 c.

Remarkably, the nanocrystal surface potentials:

• are positive (Figure 3.17 b), in contrast with the *i*-NC/*n*-Si sample (Figure 3.15 $b_1$);

• exhibit much smaller fluctuations (Figure 3.17 c) as compared to the *i*-NC/*n*-Si sample (Figure 3.15 c);

• are a priori identical for the samples $S_1$, $S_2$ and $S_3$ (Figure 3.17 c), in spite of their different nominal doping levels.

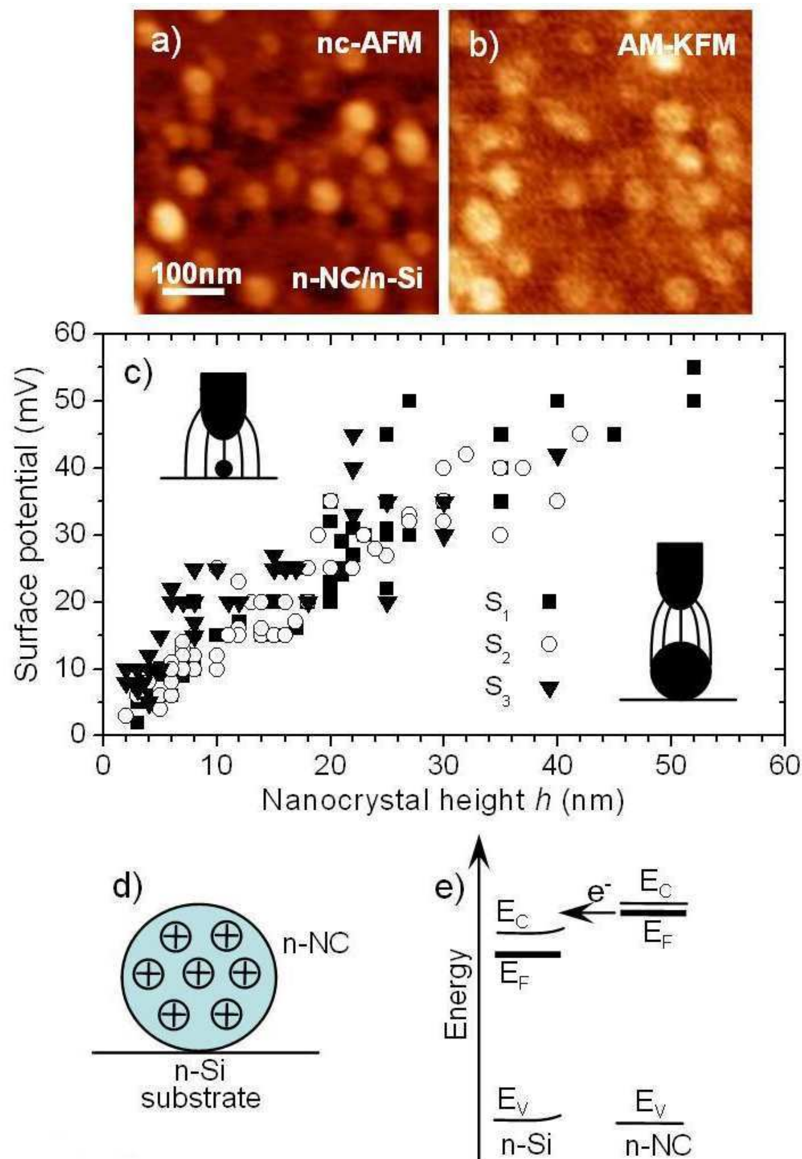


*Figure. 3.17 a) 500×500 nm² nc-AFM image (40 nm z-scale) and b) AM-KFM image (70 mV potential scale) of the n-NC/n-Si sample $S_2$. c) KFM surface potentials as a function of the nanocrystal height h for the three samples $S_1$, $S_2$ and $S_3$. d) Schematics of the ionized nanocrystal. e) Energy diagram prior to the charge transfer (indicated by the arrow). Insets: schematics of side-capacitance effects in KFM, leading to the averaging of the electrostatic potential for small nanocrystals.*

The reduction of the KFM fluctuations can be ascribed to an internal passivation of the nanocrystal surface states or defects by charges stemming from the nanocrystal donors, as pointed out in a recent works using electron paramagnetic resonance [26][38]. From an electrostatic point of view, this internal passivation mechanism generates an unoriented distribution of dipoles within the nanocrystals which shall not affect their surface potential, unlike for the *i*-NC/*n*-Si sample in which the net nanocrystal charge forms a dipole perpendicular to the substrate [39].

The positive charging of the nanocrystals is then understood as a partial ionization associated with a transfer of free electrons towards the substrate. This is sketched in Figure 3.17 d for a dopant ionization in the nanocrystal volume, without considering here the surface state charging effects, as discussed for intrinsic nanocrystals. The energy diagram associated with the charge transfer is proposed in Figure 3.17 e, assuming a degenerate nanocrystal doping. The sign of the charge transfer - here from the nanocrystal to the substrate unlike for the *i*-NC/*n*-Si sample - stems from the Fermi-level difference between the doped nanocrystal and substrate. An energy compensation mechanism can be expected, in which the electrostatic energy of the partially ionized nanocrystals equilibrates the initial difference in Fermi-levels. This accounts for the observation that the nanocrystal surface potentials look identical for the samples $S_1$, $S_2$ and $S_3$, in spite of their different nominal doping levels. This model also predicts that the charge transfer should be enhanced by quantum confinement (the doped nanocrystal Fermi level $E_F$ will rigidly follow the energy $E_C$ of the conduction band), which opens the nanocrystal band-gap and thus shifts its conduction band towards higher energies (see Figure 3.17 e).

## 3.3.4 Nanocrystal electrostatic potential for *n*-type doping

To verify this effect from experiments, we take advantage of the size distribution of the nanocrystals in the 2-60 nm range, and performed a quantitative electrostatic analysis in order to correct the AM-KFM measurements from side capacitance effects [40][41]. Side-capacitance effects are indeed a central issue for the extraction of quantitative information from KFM surface potentials, because the cantilever tip probes are actually sensitive to the electrostatic properties of the surface through a series of parallel capacitances as pointed out by Jacobs *et al.* [40]. This is described in details in the Annex A of the manuscript, but the net result of the side-capacitance effects is that the dc potential

regulated by the AM-KFM loop is not the value of the surface potential exactly under the apex of the tip, but is a weighted average over all potentials on the surface, in which the weighting factors are the derivatives of the side capacitances $C'_{it}$:

$$V_{dc} = \frac{\sum_{i=1}^{n} (C'_{it} \cdot V_i)}{\sum_{i=1}^{n} C'_{it}} \qquad (1)$$

This averaging effect is not predominant in nc-AFM for nanocrystals with large height h≥40 nm (see inset of Figure 3.17 c) for which the nanocrystal electrostatic potential ($\Delta V_0 \approx 150$ mV and $\Delta V_0 \approx 80$ mV for spherical or cylindrical nanocrystal shapes, see here below) is close to the measured KFM surface potential, but becomes important as soon as the nanocrystals diameter becomes smaller than the tip apex radius [40][41].

To actually determine the nanocrystal electrostatic potential from KFM signals, we performed a numerical calculation of the dc potential regulated by the AM-KFM loop. This potential can be deduced (see the Annex A of the manuscript for the definition), from the KFM signal which is a function of the *static* forces acting on the tip:

$$V_{dc} = -V_{stat} \times \frac{F_{V_{stat}\neq 0, Q\neq 0} - F_{V_{stat}\neq 0, Q=0} - F_{V_{stat}=0V, Q\neq 0}}{2F_{V_{stat}\neq 0, Q=0}}$$

In this expression:

- the force $F_{V_{stat}=0,\ Q\neq 0}$ is the electrostatic force at the tip, which is obtained with a grounded tip, and a charge Q placed in the nanocrystal;
- the force $F_{V_{stat}\neq 0, Q=0}$ is obtained with the tip polarized at a static bias $V_{stat}$ with respect to the surface, but without charge in the nanocrystal (Q=0);
- the total force $F_{V_{stat}\neq 0,\ Q\neq 0}$ is obtained with a the tip biased at $V_{stat}$ and in presence of charge in the nanocrystal.

This formula therefore enables to make a correspondence between surface potentials measured from KFM images and the actual nanocrystal electrostatic potentials, in presence of side-capacitance effects [40], and including the non-linear effects associated with the tip oscillation. The details of these calculations are provided in Annex A of the manuscript. We basically use a commercial Poisson solver (COMSOL) in axial symmetry. The tip is described as spherical-conical (25 nm apex radius and 15 degrees cone half-angle, a cantilever is also introduced in axial symmetry, with equivalent first capacitance

derivative with respect to experimental levers). Though the nanocrystals are expected to exhibit shapes close to spheres [42], the electrostatic analysis is hereafter conducted in spherical geometry (Figure 3.18 a), and in cylindrical geometry (Figure 3.18 b) with equal cylinder height and base diameter.

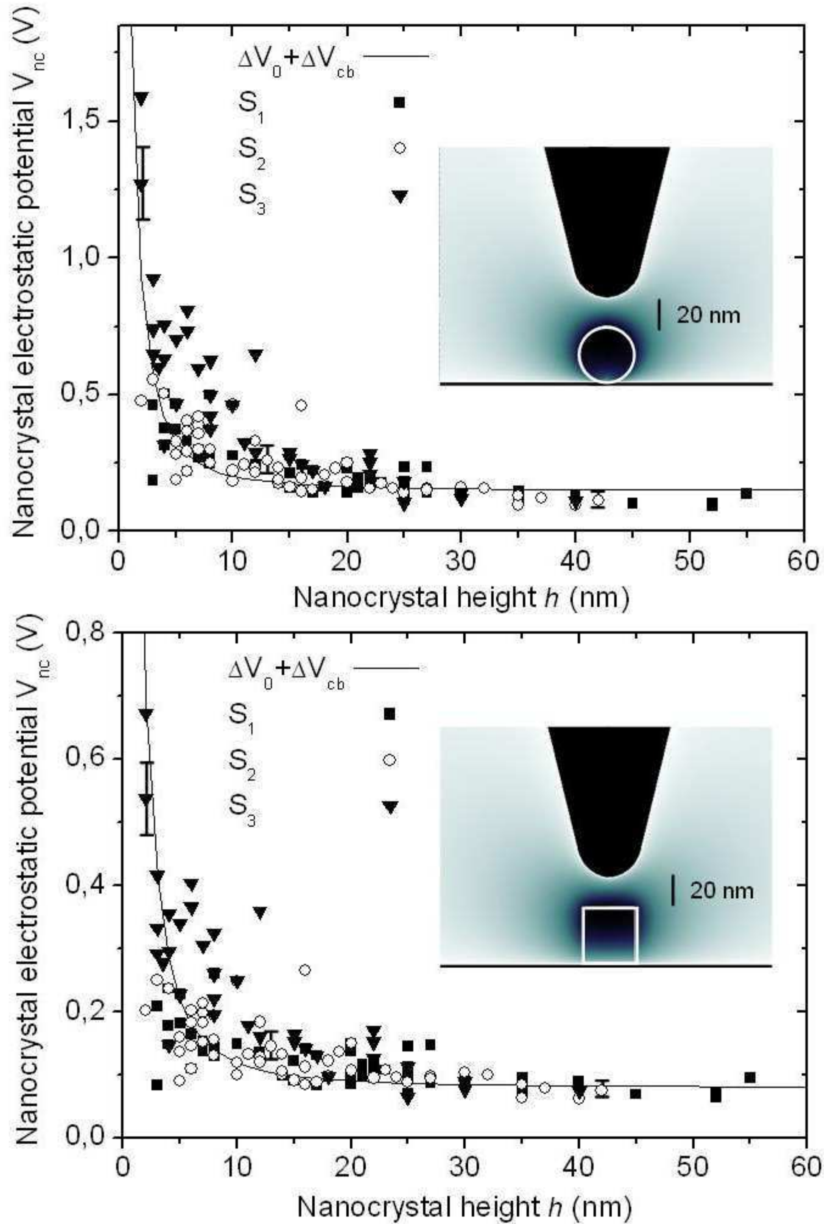


*Figure 3.18 Nanocrystal electrostatic potentials of samples $S_1$, $S_2$ and $S_3$ as a function of their height h, obtained using numerical calculations in a) spherical and b) cylindrical geometries (see insets). The lines correspond $\Delta V_0+\Delta V_{cb}$, in which $\Delta V_{cb}$ accounts for quantum confinement, and $\Delta V_0$=150 mV and $\Delta V_0$=80 mV in spherical or cylindrical geometries. Error bars correspond to the uncertainty in calculations with respect to tip-shape modelling (see text).*

The non-linearity of electrostatic forces with respect to the tip-substrate distance is taken into account by taking their average during the tip oscillation at $f_0$ due to much

smaller bandwidth of the KFM loop (typically 100-200 Hz) as compared to $f_0$ (see Annex A, section A 6). This oscillation leads to an increase of the $V_{dc}$ value as compared to the case of a non-oscillating tip. The calculated nanocrystal electrostatic potential is shown in Figure 3.18 (points) in which the error bars (10%) correspond to the maximum uncertainty in calculations while changing the tip-apex/tip cone angles in the range of 20-30 nm and 8-20 degrees.

The net result of Figure 3.18 is that the nanocrystal electrostatic potential is seen from Figure 3.18 a and 3.18 b to especially increase while reducing the nanocrystal height h below 10 nm, as expected from quantum confinement, and suggested by the equilibrium associated with the energy diagram in Figure 3.17 e.

To demonstrate this point quantitatively, we use the calculations of Ref. [22], providing phenomenological formula for the conduction band energy shift $\Delta V_{cb}$ due to quantum confinement, on the basis of parametrized tight-binding calculations. In practice, we compare the nanocrystal electrostatic potential extracted from experimental KFM data with $\Delta V_0 + \Delta V_{cb}$, in which $\Delta V_0$ is set to the electrostatic potential observed for nanocrystals with negligible quantum confinement, which can be attributed to the nominal difference of the nanocrystal and substrate Fermi levels. The values of $\Delta V_0 + \Delta V_{cb}$ (lines in Figure 3.18 a and 3.18 b) are seen to remarkably fit to the nanocrystal electrostatic potentials both in spherical and in cylindrical geometries (without any adjustable parameter). This clearly identifies the raise of electrostatic potential at small diameters as stemming from quantum confinement, independently of the assumption on the nanocrystal shape. Side-capacitance effects are thus responsible for the fact that the nanocrystal KFM signals do not vary much in the 2-40 nm range, in spite of quantum confinement. It also demonstrates that the nanocrystal charging follows an energy compensation mechanism similar to remote doping[3].

### 3.3.5 Ionisation of the *n*-doped nanocrystals

The nanocrystal ionization charge as a function of the nanocrystal height is now analyzed, and shown in Figure 3.19 (inset), in spherical geometry and for a homogeneous

[3] The nanocrystal ionization is insensitive to dopant freezing (see Annex B).

charge distribution in the nanocrystal[4]. The weak variations of the ionization charge indicate here that the enhancement of $\Delta V_0+\Delta V_{cb}$ at smaller sizes approximately matches the enhancement the nanocrystal Coulomb energy at small nanocrystal sizes. We also represented in Figure 3.19 the volume ionization of the nanocrystals. Since the ionization charge is almost constant (*i.e.* it is limited by an energy equilibrium and not by the number of available dopants), the volume charge follows a power-law behaviour in $h^{\alpha}$ with $\alpha$=2.7 close to 3, together with variations in the $5\times10^{16}$-$10^{21}$ $cm^{-3}$ range. The maximum charge density observed for the samples $S_1$, $S_2$ and $S_3$ is represented by dashed lines. It is expected to correspond to the regime of full ionization, and thus, to indicate the nanocrystal doping level. The densities (a few $10^{20}$ $cm^{-3}$) as well as their gradation between $S_1$, $S_2$ and $S_3$ are in agreement with the doping levels expected from growth conditions, although an actual measurement of the nanocrystal doping level would require a more statistical analysis.

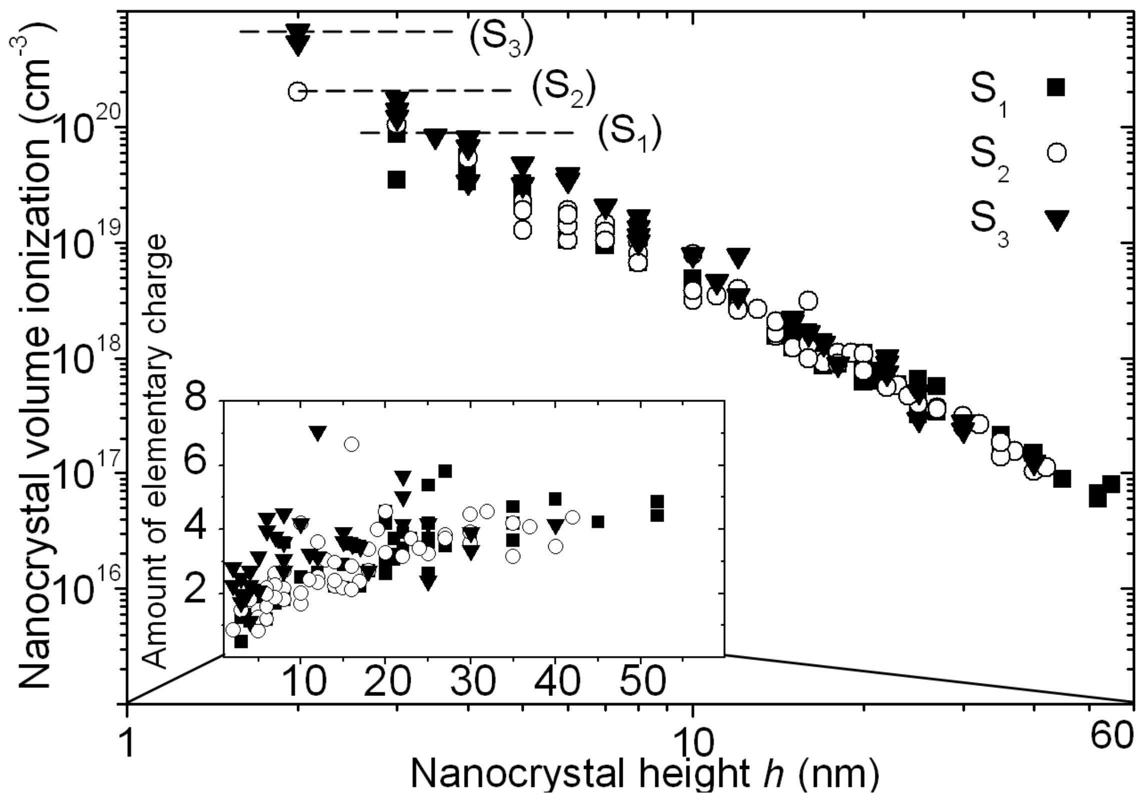


*Figure 3.19 Logarithmic plot of the volume charge of the ionized nanocrystals as a function of their height h, calculated in spherical geometry. The horizontal dotted lines indicate the maximum values for the three samples. The inset corresponds to the nanocrystal ionization charge.*

[4] This situation would correspond also to nanocrystals with core doping. A non-homogeneous charge distribution changes the nanocrystal surface dipole at fixed nanocrystal charge. At fixed KFM surface potential, it will therefore modify the nanocrystal charge, but not its average electrostatic potential as plotted in Figure 3.18.

To estimate the interest of such a doping with respect to nanodevices, we plotted in Figure 3.20 the equivalent surface and linear charge densities which would be obtained using doped nanocrystals as electron sources (see footnote 5). Such densities can be estimated by dividing the nanocrystal charge by the greater section of the nanocrystal ($=4r^2$ in the case of a two-dimensional assembly) and by its diameter (in the case of a linear chain). As seen from Figure 3.20, the corresponding two-dimensional and one-dimensional densities fall in the range of $2\times10^{11}$-$10^{14}$ $cm^{-2}$ and $8\times10^{5}$-$2\times10^{7}$ $cm^{-1}$ respectively, and are of strong interest for devices based on two-dimensional layers or one-dimensional conductors.

These results therefore put forward the possibility to use doped nanocrystals for external remote doping of one-dimensional or two-dimensional nanostructures or devices. Ultimately, ordered arrays of (e.g. colloidal) nanocrystals with core doping could also efficiently reduce the random disorder induced by ionized dopants in conventional remote doping, known to limit the transport properties of high-mobility electron gases.

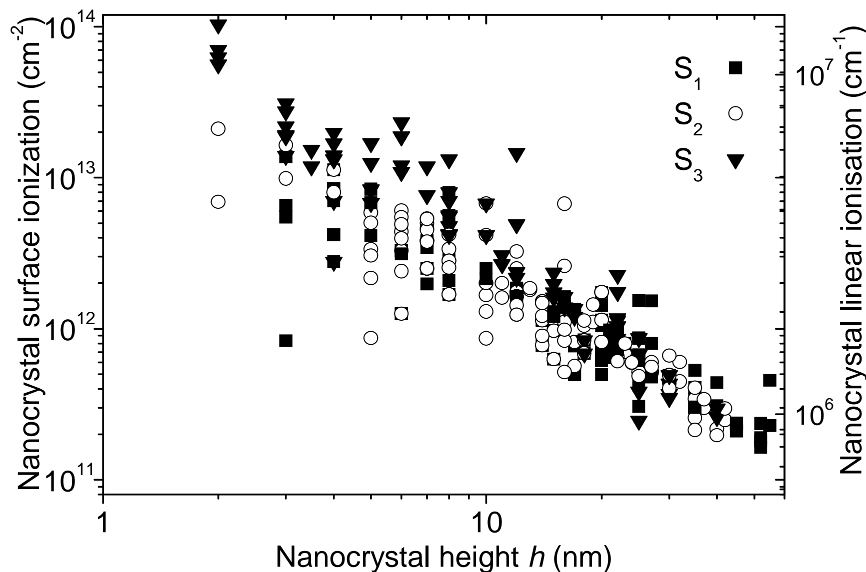


*Figure 3.20 Logarithmic plot of the surface (left scale) and linear (right scale) charge of the ionized nanocrystals as a function of their height h, calculated in spherical geometry.*

## 3.3.6 Characterization of *p*-doped nanocrystals

We show in this section the results obtained on *p*-type nanocrystals (*p*-NC/*n*-Si and *p*-NC/*p*-Si samples). In this situation, as discussed in the following, it did not prove possible to identify a similar charge transfer mechanism as for the *n*-type nanocrystals,

which we infer to stem from a lower doping or increased surface states for the *p*-type nanocrystals.

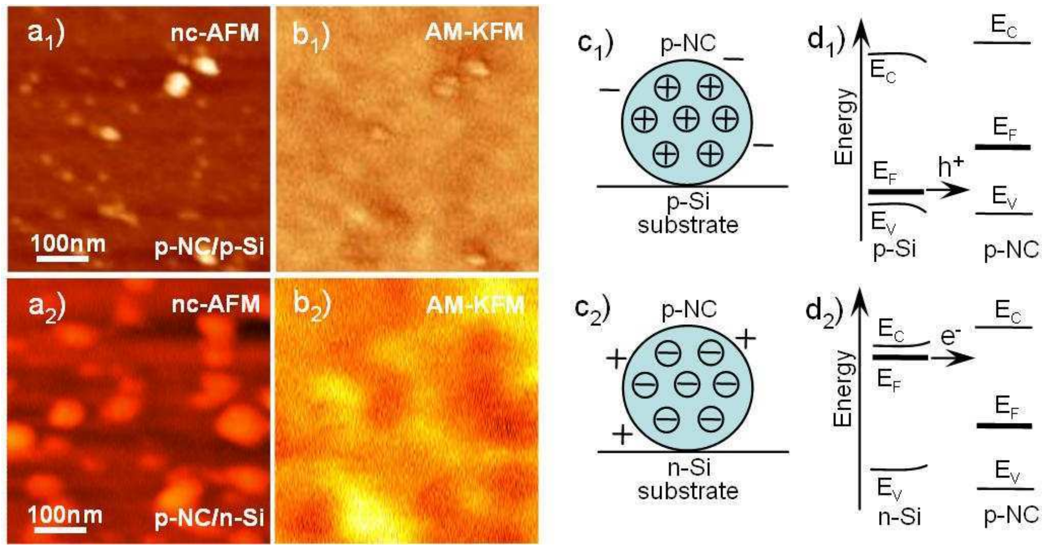


*Figure 3.21 $a_1$) and $a_2$) 500×500 nm$^2$ nc-AFM images (30 nm z-scale). $b_1$) and $b_2$) AM-KFM images (150 mV colour scale). $c_1$) and $c_2$) schematics of the nanocrystals with surface states. $d_1$) and $d_2$) energy diagrams prior to charge transfers. Charge transfers are indicated by the arrows.*

Ultra-high vacuum non-contact atomic force topography and AM-KFM images are presented in Figure 3.21 for hydrogen-passivated *p*-NC/*n*-Si and *p*-NC/*p*-Si samples. The surface potential of the *p*-NC/*p*-Si nanocrystals (Figure 3.21 $b_1$) is rather positive, with however the occurrence of a negative halo around the nanocrystals. This does not correspond to the charge transfer mechanism established for the *n*-type nanocrystals, which would lead here to negatively charged nanocrystals. Here, rather, the positive charge is transferred from the surface to the nanocrystal. For the *p*-NC/n-Si sample, the nanocrystal surface potentials are negative (Figure 3.21 $b_2$), also in agreement with a charge transfer from the substrate to the nanocrystal. This altogether leads to the energy diagrams presented in Figure 3.21 $d_1$ and 3.21 $d_2$, in which the nanocrystal Fermi level is positioned within the gap of the nanocrystal. Such a picture means that the *p*-type doped nanocrystals behave in practice like intrinsic nanocrystals. This implies that the internal passivation of surface states by the free carriers released by the dopants (as in the case of *n*-type doped nanocrystals) is not effective enough, which can be due: *(i)* either to a lower effective doping of the *p*-type nanocrystals[5]; or *(ii)* to an increase of the surface states of the

[5] A tentative explanation for this weaker doping level in the case of *p*-type nanocrystals would be to consider a doping compensation introduced by a contamination by residual oxygen atoms at the nanocrystal surface.

nanocrystals which prevents to observe a charge transfer towards the substrate as in the case of *n*-type nanocrystals.

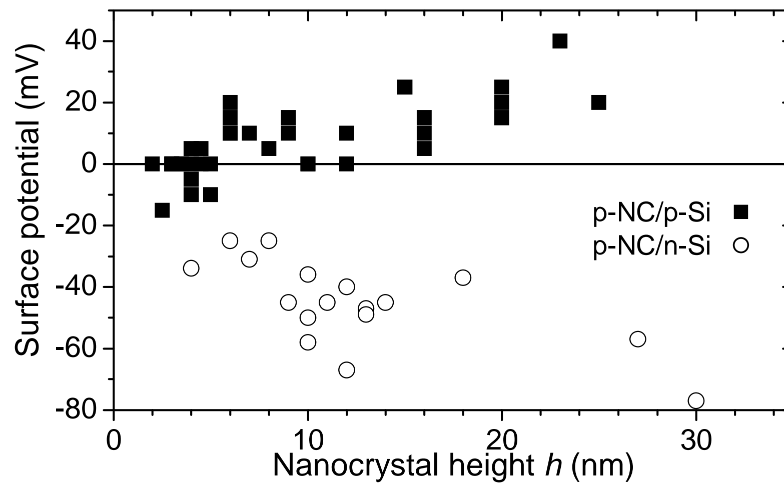


*Figure 3.22 KFM surface potential as a function of height h for the samples p-NC/p-Si and p-NC/n-Si.*

To check for this, we monitored the fluctuations in the nanocrystal surface potential (see Figure 3.22), both for the *p*-NC/*n*-Si and *p*-NC/*p*-Si samples. The fluctuations appear to be smaller than for the intrinsic nanocrystals (Figure 3.16), but larger as compared to the *n*-NC/*n*-Si samples $S_1$, $S_2$ or $S_3$ (Figure 3.17 c). This effect is summarized graphically in Figure 3.23, in which the fluctuations of the intrinsic, *n*-doped, and *p*-doped nanocrystal samples have been calculated, and represented as histograms. It is obvious from this graph that the *p*-type doped nanocrystals samples provide an intermediate situation between the *n*-doped nanocrystals for which surface states are internally passivated, and intrinsic samples, which exhibit stronger surface potential fluctuations.

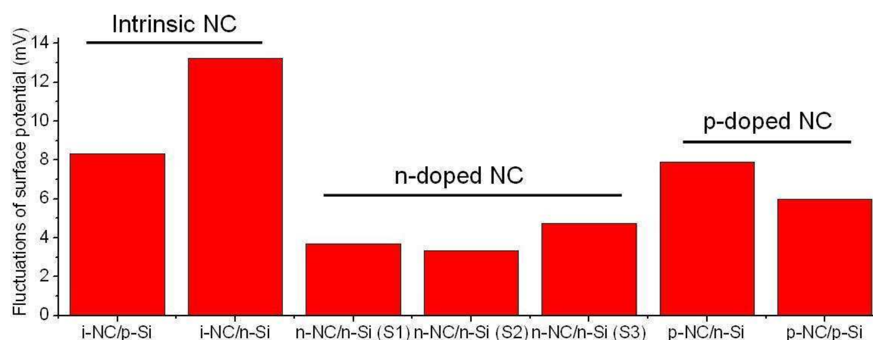


*Figure 3.23 Fluctuations of surface potential for intrinsic and doped nanocrystal samples.*

### 3.3.7 Electrostatic potential of intrinsic nanocrystals

Using the same setup of KFM simulation as for the case of *n*-doped nanocrystals, we now calculate from the experimental data of Figure 3.16 the electrostatic potential of the intrinsic nanocrystals on *n*-type and *p*-type substrates. We start with the *i*-NC/*n*-Si sample and use the mechanism of Figure 3.15 $d_1$ to predict the maximum electrostatic potential which can be achieved, assuming that the nanocrystal and substrate Fermi levels will coincide after charge transfer. The average negative charging of the nanocrystals corresponds to a situation in which the nanocrystal Fermi level prior to charge transfer falls below the Fermi level of the substrate. The maximum energy difference is thus $E_g+\Delta V_{vb}$ (assuming the bulk substrate Fermi level to coincide with its conduction band), in which $\Delta V_{vb}$ is the nanocrystal valence band energy shift associated with quantum-confinement. Similarly, a positive charging can be expected, however provided the substrate Fermi level would fall below the nanocrystal Fermi level before charge transfer. The maximum energy difference is $\Delta V_{cb}$ in which $\Delta V_{cb}$ is the nanocrystal conduction band energy shift associated with quantum confinement. These two limit values $-(E_g+\Delta V_{vb})$ and $+\Delta V_{cb}$ define the lower and upper values expected for the nanocrystal electrostatic potential, in case of a negative or positive nanocrystal charging, respectively. As seen from Figure 3.24, the electrostatic potential derived from experimental data of Figure 3.16 (assuming a spherical nanocrystal shape) fall within these two values.

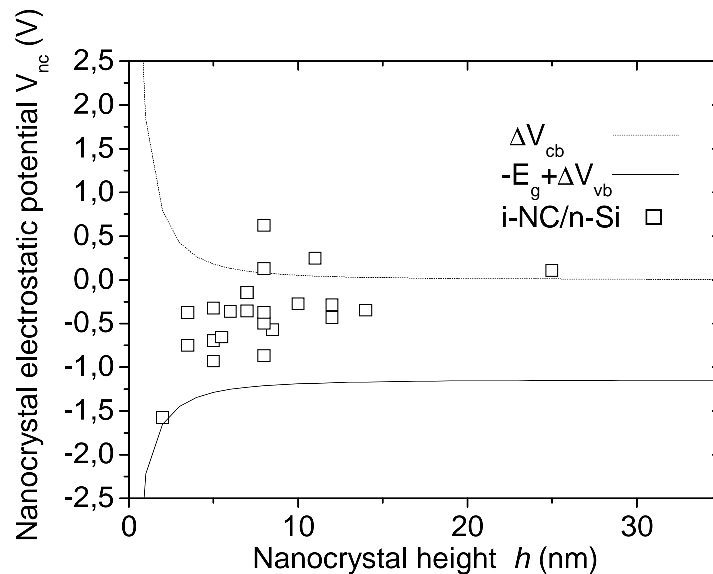


*Figure 3.24 Plot of the nanocrystal electrostatic potential for the i-NC/n-Si sample, as a function of the nanocrystal height. The lines correspond to the values of $\Delta V_{cb}$ and $-(E_g+\Delta V_{vb})$ (see text).*

Similar limits can be defined for the intrinsic nanocrystals deposited on *p*-type silicon, starting from the mechanism of Figure 3.15 $d_2$. A positive charging can be

expected, with an upper limit corresponding to $+(E_g+\Delta V_{cb})$, while a negative charging can be expected with a limit of $-\Delta V_{vb}$. Experimental values derived from the KFM data of Figure 3.16 also fall within this energy range. In both cases (Figure 3.24 and Figure 3.25) the limits for the positive and negative charging are also in agreement with the dissymmetry of the electrostatic potential observed for the intrinsic nanocrystal charging, when deposited on *n*-type or *p*-type substrates.

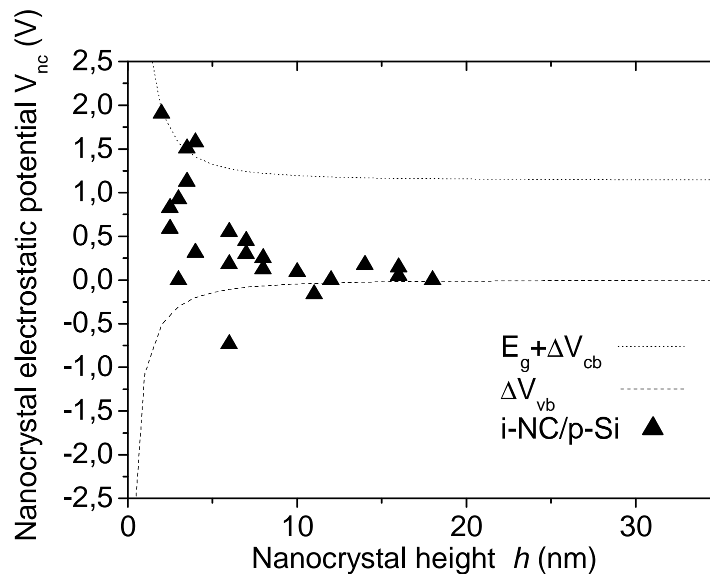


*Figure 3.25 Plot of the nanocrystal electrostatic potential for the i-NC/p-Si sample, as a function of the nanocrystal height. The lines correspond to the values of $E_g+\Delta V_{cb}$ and $-\Delta V_{vb}$ (see text).*

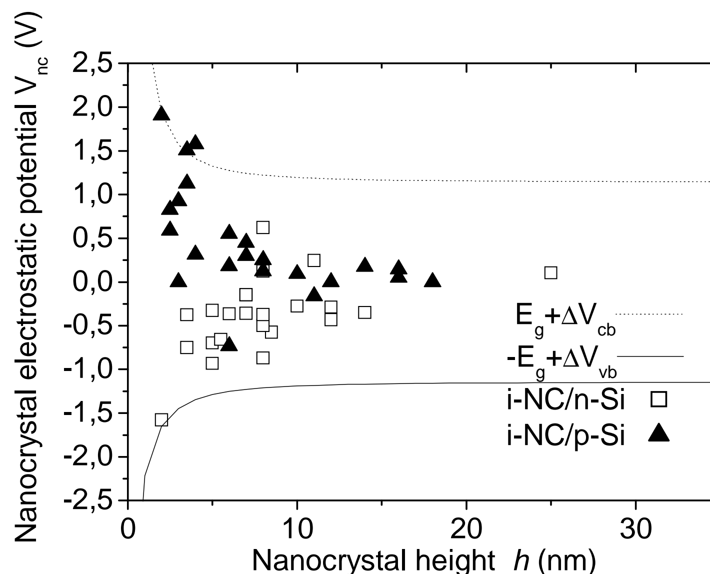


*Figure 3.26 Plot of the nanocrystal electrostatic potentials for the i-NC/n-Si and i-NC/p-Si samples, as a function of the nanocrystal height. The lines correspond here to the maximum positive and negative electrostatic potential values $E_g+\Delta V_{cb}$ and $-(E_g+\Delta V_{vb})$ (see text).*

We now compare the electrostatic potentials of the two *i*-NC/*p*-Si and *i*-NC/*n*-Si samples in Figure 3.26, together with their upper and lower charging limits $E_g+\Delta V_{cb}$ and $-(E_g+\Delta V_{vb})$. It is seen that, the experimental values for the nanocrystal electrostatic energy fall to zero for large-size nanocrystals (h≥15nm), while they almost saturate the upper and lower charging limits in the case of small-size nanocrystals (h≤5nm). We interpret this effect as the fact that the charge transfer associated with the mechanisms of Figure 3.15 $d_1$ and 3.15 $d_2$ is limited by energy differences only *provided a sufficient number of surface states can be populated*. This suggests that the charge transfer will be limited by the number of available surface states in the case of large-size nanocrystals (h≥15nm) while it is limited by the nanocrystal electrostatic energy in the case of small-size nanocrystals (h≤5nm). The surface state charge densities for nanocrystals of diameter 10-30 nm is estimated in the range $10^{11}$-$10^{12}$ $cm^{-2}$, corresponding to a few elementary charges per nanocrystal.

## 3.3.8 Nanocrystal electrostatic potential for *p*-type doping

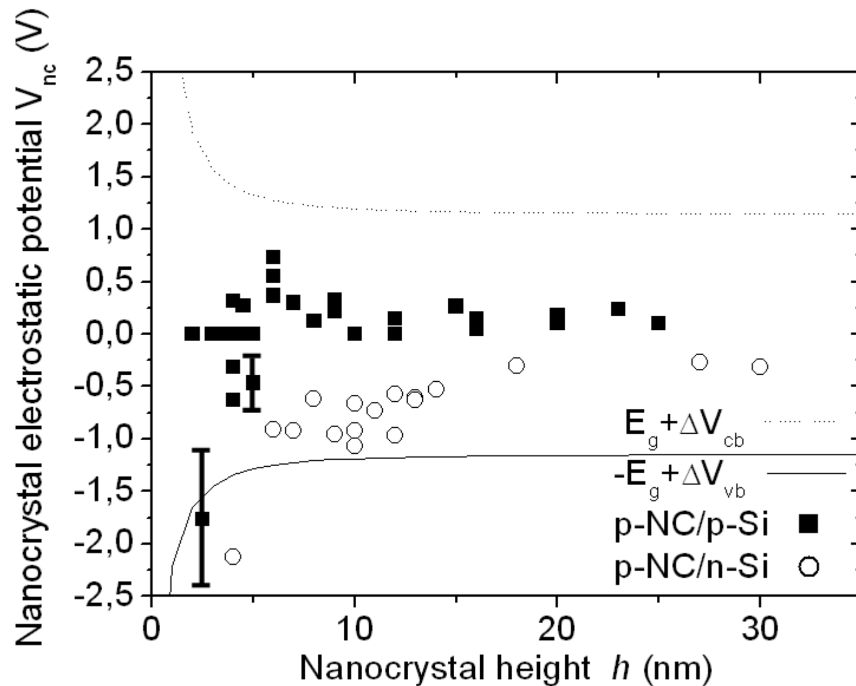


*Figure 3.27 Nanocrystal electrostatic potential of samples p-NC/p-Si and p-NC/n-Si as a function of their height h, calculated assuming spherical nanocrystal shapes. The lines correspond to a calculation of the quantum confinement effects on the nanocrystal conduction band (dotted line) and valence band (full line), using respective shifts $\Delta V_1$=250mV and $\Delta V_2$=1143mV for large diameter nanocrystals. Error bars correspond to uncertainty in reading of the surface potential.*

We calculated the electrostatic potential of the ionized *p*-type doped nanocrystals, assuming a spherical nanocrystal shape, and following the approach of section 3.3.4 for the *n*-type doped nanocrystals, and of section 3.3.7 for the intrinsic nanocrystals. The experimental values are presented in Figure 3.27, both for the *p*-NC/*n*-Si and *p*-NC/*p*-Si samples.

Since the charge transfer for the *p*-type nanocrystals stems from the substrate, as in the case of the intrinsic nanocrystals, we also represented in Figure 3.27 the upper and lower limits for the electrostatic potential energy – ($E_g+\Delta V_{vb}$) and $E_g+\Delta V_{cb}$ as in Figure 3.26. It is striking from the comparison between Figure 3.27 and Figure 3.26 that the *p*-type doped nanocrystals *do not however* behave like intrinsic nanocrystals:

- *(i)* the fluctuations in the electrostatic potential are much smaller in Figure 3.27 as compared to Figure 3.26 - in agreement with Figure 3.23 - which indicates a passivation of the surface states by the nanocrystal doping;
- *(ii)* the electrostatic potential of the *p*-type nanocrystals on *p*-type Si is not enhanced for small-size nanocrystals, in contrast with the case of the *i*-NC/*p*-Si sample (see Figure 3.26), and exhibit rather either positive and negative values for nanocrystal diameters less than 5nm.

These observations could be explained by considering the *p*-type nanocrystals as low-doped, *e.g.* due to a lower nominal doping or increased surface states as compared to *n*-type nanocrystals. Such a behaviour could explain: *(i)* the sign of the charge transfers as in the schematics of Figure 3.21 $d_1$ and 3.21 $d_2$; *(ii)* the lower electrostatic potential fluctuations as compared to the intrinsic nanocrystal samples. Assuming also that the Fermi level in the *p*-type doped nanocrystal follows rigidly the valence band energy shift due to quantum confinement, one also predicts that the nanocrystal Fermi level will cross that of the *p*-type substrate when the nanocrystal size is reduced, which can tentatively explain the occurrence of negative charge features for some small-size *p*-type doped nanocrystals on *p*-type substrate, as discussed above.

## 3.4 Conclusions

We have demonstrated the mechanisms of ionization and charge transfer from intrinsic and doped nanocrystals towards doped silicon substrates. It was shown that intrinsic nanocrystals import a substrate charge to fill surface states, but that this

mechanism is reversed in the case of *n*-type doped nanocrystals on *n*-type substrates for which *(i)* surface states are internally passivated (*i.e.* using free carriers available from internal nanocrystal donors) and *(ii)* transfer a charge towards the substrate in an energy compensation mechanism similar to remote doping, but however enhanced by quantum confinement. Experimental results provide a measurement of the nanocrystal band-gap opening induced by quantum confinement in the 2-50nm range, in agreement with parametrized tight-binding calculations. They also put forward the possibility to use doped nanocrystals as electron sources to control the doping of nanostructures and nanodevices. An ultimate goal to would be *e.g.* to use ordered arrays of nanocrystals (for example: core-doped colloidal nanocrystals) to efficiently reduce random disorder induced by ionized dopants in conventional remote doping, known to limit the transport of high-mobility electron gases.

# References:

[1] www.wikipedia.org

[2] "*Synthesis, passivation and charging of silicon nanocrystals*" - Thesis by E. A. Boer

[3] "*Silicon-based visible light-emitting devices integrated into microelectronic circuits*" - K. D. Hirschamn, L. Tsybeskov, S.P. Duttagupta, P.M. Fauchet, **Nature,** 384, 338-341 (1996)

[4] *"Progress towards silicon optoelectronics using porous silicon technology"* - L. T. Canham, T. I. Cox, A. Loni, A. J. Simons, **Applied Surface Science**, 102, 2, 436-441 (1996)

[5] *"Characterization of silicon nanoparticles prepared from porous silicon"* - R. A. Bley, S. M. Kauzlarich, J. E. Davis, H. W. H. Lee, **Chemical Materials,** 8, 1881-1888 (1996)

[6] *"Electronic states and luminescence in porous silicon quantum dots: The role of oxygen"* - M. V. Wolkin, J. Jorne, P.M. Fauchet, G. Allan, and C. Delerue, **Physical Review Letters,** 82, 1 (1999)

[7] *"Luminescent colloidal silicon suspensions from porous silicon"* - J. L. Heinrich, C. L. Curtis, G. M. Credo, M. J. Sailor, K. L. Kavanach, **Science**, 255, 5040, 66-68 (1992)

[8] *"Thermally assisted formation of silicon islands on a silicon-on-insulator substrate"* - B. Legrand, V. Agache, T. Melin, J. P. Nys, V. Senez, D. Stievenard, **Journal of Applied Physics**, 91, 1 (2001)

[9] *"Formation of silicon islands on a silicon on insulator substrate upon thermal annealing"* - B. Legrand, V. Agache, J. P. Nys, V. Senez, and D. Stievenard, **Applied Physics Letters,** 76, 22 (2000)

[10] *"Evidence for changes in the electronic and photoluminescence properties of surface-oxidized silicon nanocrystals induced by shrinking the size of the silicon core"* - J. A. Carlisle, M. Dongol 1, I. N. Germanenko, Y. B. Pithawalla, M. S. El-Shall, **Chemical Physics Letters,** 326, 335–340 (2000)

[11] *"Process for producing luminescent silicon nanoparticles"* - M. T. Swihart, X. Li, Y. He, **Provisional patent application**, US 7,371,666 B2 (2008)

[12] *"Large-scale synthesis of ultra fine Si nanoparticles by ball milling"* - C. Lam, Y. F. Zhang, Y. H. Tang, C. S. Lee, I. Bello, S. T. Lee, **Journal of crystal growth,** 220, 466-470 (2000)

[13] *"A liquid-solution-phase synthesis of crystalline silicon"* - J. R. Heath, **Science**, 258, 5085, 1131 - 1133 (1992)

[14] *"Size tunable visible luminescence from individual organic monolayer stabilized silicon nanocrystal quantum dots"* - D. S. English, L. E. Pell, Z. Yu, P. F. Barbara, B. A. Korgel, **Nanoletters,** 2, 7, 681-685 (2002)

[15] *"Electronic spectroscopy and photophysics of Si nanocrystals: Relationship to bulk c-Si and porous Si"* - L. E. Brus, P. F. Szajowski, W. L. Wilson, T. D. Harris, S. Schupper, P. H. Citrin, **Journal of the American Chemical Society**, 117, 2915-2922 (1995)

[16] *"Sinterable ceramic powders from laser-driven reactions: I, process description and modeling"* - W. R. Cannon, S. C. Danfortch, J. H. Flint, J. S. Haggerty, R. A. Marra, **Journal of the American Ceramic Societ**y, 65, 7, 324-330 (1982)

[17] *"Structured films of light-emitting silicon nanoparticles produced by cluster beam deposition"* - F. Huisken, B. Kohn, **Applied Physics Letters** 74, 3776 (1999)

[18] *"A two steps CVD process for the growth of silicon nano-crystals"* - F. Mazen, T. Baron, A. M. Papon, R. Truche, J. M. Hartmann, **Applied Surface Science**, 214, 359 - 363 (2003)

[19] *"Soft landing of silicon nanoparticles in plasma enhanced chemical vapour deposition"* - N. Chaabane, V. Suendo, H. Vach, P. Roca i Cabarrocas, **Applied Physics Letters,** 88, 203111 (2006)

[20] *"Synthèse et contrôle de la taille de nanocristaux de silicium par plasma froid. Application dans les domaines de l'optoélectronique et de la nanoélectronique"* - Thesis by T. Nguyen-Tran (2007)

[21] *"Photoluminescence of size-separated silicon nanocrystals: Confirmation of quantum confinement"* - G. Ledoux, J. Gong, F. Husken, O. Guillois, C. Reynaud, **Applied Physics Letters**, 80, 25 (2002)

[22] "*Method of tight-binding parametrization: Application to silicon nanostructures"* - Y. M. Niquet, C. Delerue, G. Allan, M. Lannoo, **Physical Review B**, 62, 8 (2000)

[23] *"Silicon quantum wire array fabrication by electrochemical and chemical dissolution of wafers"* - L. T. Canham, **Applied Physics Letters**, 57, 1046 (1990)

[24] *"Stimulated blue emission in reconstituted films of ultrasmall silicon nanoparticles"* - M. H. Nayfeh, N. Barry, J. Therrien, O. Akcakir, E. Gratton, G. Belomoin, **Applied Physics Letters,** 78, 8 (2001)

[25] *"Single-exciton optical gain in semiconductor nanocrystals"* - V. I. Klimov, S. A. Ivanov, J. Nanda, M. Achermann, I. Bezel, J. A. McGuire, A. Piryantiski, **Nature,** 447, 441 - 446 (2007)

[26] *"Electronic properties of doped silicon nanocrystal films"* - R. Lechner, A. R. Stegner, R. N. Pereira, R. Dietmueller, M. S. Brant, A. Ebbes, M. Trocha, H. Wigges, M. Stutzmann, **Journal of Applied Physics,** 104, 053701 (2008)

[27] “*Identification of atomic-like electronic states in indium arsenide nanocrystal quantum dots*” - U. Banin, Y. Cao, D. Katz, O. Millo, **Nature,** 400, 542-544 (1999)

[28] *“Wave-function mapping of InAs quantum dots by scanning tunneling spectroscopy”* - T. Maltezopoulos, A. Bolz, C. Meyer, C. Heyn, W. Hansen, M. Morgenstern, R. Wiesendanger, **Physical Review Letters**, 91, 196804 (2003)

[29] *“Probing the size and density of silicon nanocrystals in nanocrystal memory device applications”* - T. Feng, H. Yu, M. Dicken, J. R. Heath, H. A. Atwater, **Applied Physics Letters,** 86, 033103 (2005)

[30] *“Charge injection in individual silicon nanoparicles deposited on a conductive substrate”* - T. Mélin, D. Deresmes, D. Stiévenard, **Applied Physics Letters**, 81, 26 (2002)

[31] “*Charge-injection mechanisms in semiconductor nanoparticles analyzed from force microscopy experiments”* - S. Barbet, T. Mélin, H. Diesinger, D. Deresmes, D. Stiévenard, **Physical Review B**, 73, 045318 (2006)

[32] *“Charging of single Si nanocrystals by atomic force microscopy”* - E. A. Boer, L. D. Bell, M. L. Brongersma, H. A. Atwater, **Applied Physics Letters,** 78, 3133 (2001)

[33] *“Electric force microscopy of individually charged semiconductor nanoparticles”* - H. Diesinger, T. Mélin, S. Barbet, D. Deresmes, D. Stiévenard, **Physica Status Solidi**, 203, 6, 1344-1247 (2006)

[34] *“Electric force microscopy of individually charged nanoparticles on conductors: An analytical model for quantitative charge imaging”* - T. Mélin, H. Diesinger, D. Deresmes, D. Stiévenard, **Physical Review B,** 69, 035321 (2004)

[35] *“Probing electron charging in nanocrystalline Si dots using Kelvin probe force microscopy”* - M. A. Salem, H. Mizuta, S. Oda, **Applied Physics Letters** 85, 15 (2004)

[36] *“Single-electron devices and their applications*” - K. Likharev**, Proceedings of the IEEE,** 87, 606 (1999)

[37] *“Charge, polarizability, and photoionization of single semiconductor nanocrystals”* - T. D. Krauss and L. E. Brus, **Physical Review Letters**, 83, 23 (1999)

[38] *“Electronic transport in phosphorus-doped silicon nanocrystal networks”* - A. R. Stegner, R. N. Pereira, K. Klein, R. Lechner, R. Dietmueller, M. S. Brandt, M. Stutzmann, H. Wiggers, **Physical Review Letters**, 100, 026803 (2008)

[39] *“Probing nanoscale dipole-dipole interactions by electric force microscopy”* - T. Mélin, H. Diesinger, D. Deresmes, and D. Stiévenard, **Physical Review Letters**, 92, 166101 (2004)

[40] *“Resolution and contrast in Kelvin probe force microscopy”* - H. O. Jacobs, P. Leuchtmann, O. J. Homan, and A. Stemmer, **Journal of Applied Physics**, 84, 3 (1998)

[41] *"Lateral resolution and potential sensitivity in Kelvin probe force microscopy: Towards understanding of the sub-nanometer resolution"* - F. Krok, K. Sajewicz, J. Konior, M. Goryl, P. Piatkowski, M. Szymonski, **Physical Review B**, 77, 235427 (2008)

[42] *"Synthesis of silicon nanocrystals in silane plasmas for nanoelectronics and large area electronic devices"* - P. Roca i Cabarrocas, Th. Nguyen-Tran, Y. Djeridane, A. Abramov, E. Johnson, G. Patriarche, **Journal of Physics D: Applied Physics,** 40, 2258-2266 (2007)

# Summary

The aim of this PhD was to use atomic force microscopy in ultra-high vacuum in order to characterize the electronic properties of individual nanostructures, here semiconductor nanowires or nanocrystals. The questions which have been addressed were:

- to probe the local transport in nanostructures;
- to characterize the influence of surface states (gold residues in case of a catalytic growth, oxide, or residual surface states for hydrogen-passivated silicon nanostructures) on the nanostructure transport or electrostatic properties;
- to investigate charge transfers at the nanoscale;
- to probe band-structure effects such as quantum confinement.

Silicon nanowires grown by metal-catalyzed chemical vapour deposition (CVD) on doped (111) silicon substrates have been characterized locally using conducting AFM in ultra-high vacuum. Local current-voltage characteristics have been taken as a function of the position along tilted nanowires. It is shown that the conduction along as-grown intrinsic nanowires is dominated by gold residues associated with the catalytic growth, which can be partially removed by chemical de-oxidation and recovered upon thermal annealing.

Amplitude-modulation Kelvin probe microscopy has also been used to investigate hydrogen-passivated phosphorus-doped and boron-doped silicon nanocrystals grown by plasma enhanced chemical vapor deposition (PECVD) on silicon substrates. We have demonstrated the mechanisms of ionization and charge transfer from intrinsic and doped nanocrystals towards doped silicon substrates. It was shown that intrinsic nanocrystals import a substrate charge to fill surface states, but this mechanism is reversed in the case of *n*-type doped nanocrystals on *n*-type substrates for which *(i)* surface states are internally passivated (using free carriers available from internal nanocrystal donors) and *(ii)* transfer a charge towards the substrate in an energy compensation mechanism similar to remote doping, which is however enhanced by quantum confinement. Experimental results provide a measurement of the nanocrystal band-gap opening induced by quantum confinement in the 2-50nm range, in agreement with parametrized tight-binding calculations. They also put forward the possibility to use doped nanocrystals as electron sources to control the doping of nanostructures and nanodevices.

We have finally developed numerical simulations to derive the dc bias regulated by a Kelvin loop from the calculation of static force fields. The calculations enable to take into

account *(i)* the effect of side-capacitances in amplitude modulation KFM; and *(ii)* the non-linear effects associated with the tip oscillation (if any) in KFM experiments. Results have been used to extract the electrostatic potential of ionized silicon nanocrystals with size in the 2-50nm range from experimental KFM data.

To summarize, in this thesis I have presented AFM experiments in UHV environment, as an efficient way to characterize nanostructures like nanowires or nanocrystals, with a sensitivity able to detect a few charges, and adequate to see the influence of surface states and quantum confinement effects. This opens new perspectives in the field of *nano-characterization on insulators*, for which the use of a mechanical probe can be now foreseen as a tool to perform local electronic spectroscopy measurements, including single-electron effects and quantum band structure. Electrical techniques derived from atomic force microscopy appear well-suited to study future quantum devices made from nanostructures.

# Annex A

## Description of the numerical calculations used to analyze Kelvin force microscopy experiments

# A 1 Introduction

As described in the introduction of this manuscript (Chapter I), Kelvin force microscopy allows to measure the average surface potential below the atomic force microcopy tip apex, which consists in a weighted average of the local surface potentials below the tip with respect to capacitance derivatives [1]. To derive quantitative information from KFM signals, *e.g.* on individual nanostructures, it is therefore necessary to take side-capacitance effects into account, which can be done using numerical simulations of the systems under investigation.

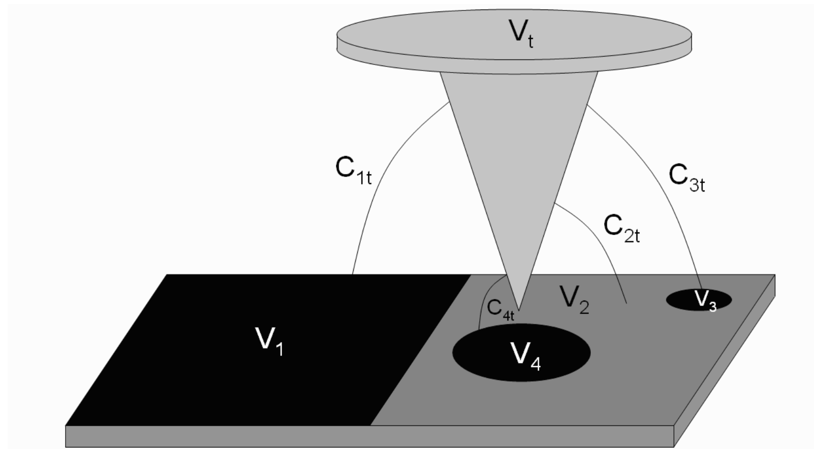


*Figure A 1 Model of the KFM setup in which electrostatic interactions are represented by mutual capacitances $C_{ij}$ between the cantilever tip and the (possibly) inhomogeneous surface. From Ref. [1].*

Jacobs *et al.* [1] first introduced the approach of side capacitances (see Figure A 1), in which the tip feels the surface through its apex, cone and cantilever, the surface being also possibly inhomogeneous. It was shown analytically that the surface potential measured by KFM (*i.e.* by nullifying the force component at the electrostatic actuation angular frequency ω) is a weighted average over all the local potentials on the surface, in which the capacitance derivatives $C'_{it}$ (with respect to the tip-substrate distance z) are the weighting factors[1]:

$$V_{dc} = \frac{\sum_{i=1}^{n} (C'_{it} \cdot V_i)}{\sum_{i=1}^{n} C'_{it}}$$

[1] This formula applies for amplitude-modulation KFM (AM-KFM), in which the KFM loop extracts a surface potential by nullifying the cantilever oscillation which is proportional to the excitation force, and thus, to the first derivatives of the tip-substrate capacitances. In the case of frequency-modulation KFM (FM-KFM), the signal taken into account by the KFM loop is the cantilever frequency shift upon an ac modulation of the tip bias, which is proportional to force gradients, and thus to the tip-substrate second capacitance derivatives. A similar formula would then be established, based on second capacitance derivatives.

Considering the Figure A 1, the potential spot on the right from the tip will have a smaller weighting factor because of its smaller size and larger distance from the tip, as compared to the spot under the tip and to electrode with the step of potential on the left side of the tip. Thus, this potential will have a smaller contribution in the measured KFM signal. In addition, if the tip is moved to the left towards the stepped electrode, the weight $C'_{1t}$ will increase, while $C'_{2t}$ and $C'_{3t}$ will decrease. Therefore, the ideal step in the surface potential will appear as a smoothed step in the KFM potential image due to side-capacitance averaging effects.

Jacobs *et al.* [1] performed numerical simulations of these effects using a "multiple multipole" program, which solves Maxwell's equations and calculates the charge $Q_t$ at the tip for a given set of electrodes with potentials $V_i$. Considering here only the two contributions of the spot of potential $V_1$ below the tip and of the step potential $V_2$ on the left side, the $V_{dc}$ potential obtained by KFM can be written:

$$V_{dc} = \frac{C'_{1t}V_1 + C'_{2t}V_2}{C'_{1t} + C'_{2t}}$$

where the capacitances $C'_{1t}$ and $C'_{2t}$ depend on the location of the tip and diameter of the disk for the potential spot.

The tip charge $Q_t(z)$is given by:

$$Q_t = C_{1t}(V_t - V_1) + C_{2t}(V_t - V_2)$$

If the value of $Q_t(z)$ is known, $C_{1t}$ and $C_{2t}$ can be found by selecting boundaries $V_t=V_2=0$, $V_1\neq0$ and $V_t=V_1=0$ and $V_2\neq0$ respectively:

$$C_{1t} = -\frac{Q_t(z)}{V_1}$$

$$C_{2t} = -\frac{Q_t(z)}{V_2}$$

The derivatives of $C'_{1t}$ and $C'_{2t}$ can then be calculated by introducing a small height change $\Delta z$ of the tip and computing the variation of the capacitances:

$$C'_{1t} = \frac{\left[C_{1t}\left(z+\Delta z\right) - C_{1t}(z)\right]}{\Delta z}$$

$$C'_{2t} = \frac{\left[C_{2t}\left(z+\Delta z\right) - C_{2t}(z)\right]}{\Delta z}$$

These derivatives are the weighted factors of $V_1$ and $V_2$ in the measured $V_{dc}$ potential. These factors will depend on the geometry of the tip, and of its distance from the charges.

Charrier *et al.* [2] have proposed more recently three-dimensional simulations of a KFM system, taking into account a "real size" tilted cantilever (Figure A 2). They compared the output of the calculations with experiments performed on a µm-size device, so as to investigate the influence of the cantilever orientation with respect to the sample (*i.e.* cantilever set orthogonal or parallel to the device under investigation). A dependence was obtained for sufficiently large structures (or devices) and tip-substrate distances, so that the side-capacitance associated with the cantilever becomes non-negligible.

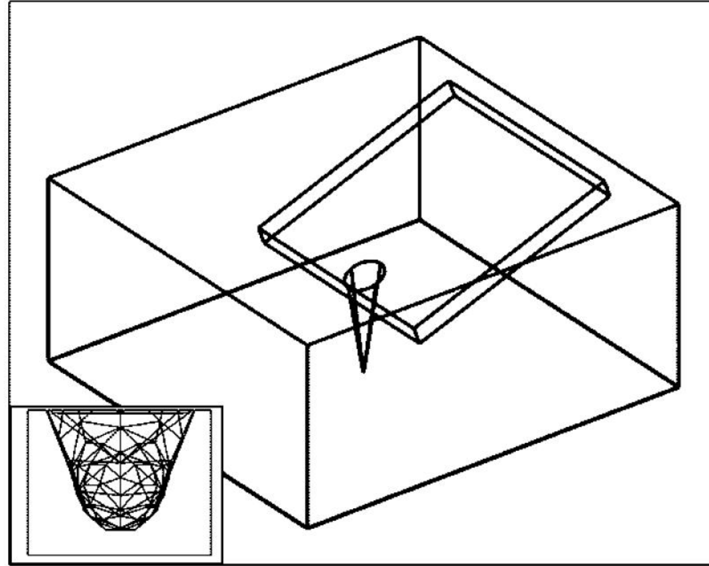

*Figure A 2 Three-dimensional drawing of the tip – consisting of the cantilever, cone, and apex - in a vacuum box which determines the calculation space. The box size is 50 µm × 65 µm (surface) × 25 µm (height). The inset is a zoom on the tip meshing, showing that the apex is defined here as a finite combination of tetrahedrons, which can lead to a limitation in resolution. From Ref. [2].*

Brunel *et al.* [3] recently followed the approach of Jacobs, but proposed a fully experimental approach to extract the weighted average of surface potentials, in the case of a carbon nanotube field effect transistor (CNTFET) device operated in ambient air (tip-substrate distance z~80nm). In this case, four types of capacitances were considered (Figure A 3): $C_{NT}$ is the tip nanotube-capacitance associated with the nanotube potential $V_{NT}$, $C_G$ is the tip-backgate capacitance associated with the backgate bias $V_G$, and finally $C_D$ and $C_S$ are the capacitive coupling between tip drain and source contact pads at the potentials $V_D$ and $V_S$. If $C = C_{NT} + C_G + C_D + C_S$, the potential $V_{KFM}$ regulated by the KFM loop (here, amplitude-modulation KFM in air) can be written as $V_{KFM} = \alpha_{NT}V_{NT} + \alpha_G V_G + \alpha_D V_D + \alpha_S V_S$, where $\alpha_{NT}=(\partial C_{NT}/\partial z)/(\partial C/\partial z)$, $\alpha_G=(\partial C_G/\partial z)/(\partial C/\partial z)$, $\alpha_D=(\partial C_D/\partial z)/(\partial C/\partial z)$, and $\alpha_S=(\partial C_S/\partial z)/(\partial C/\partial z)$ are the normalized capacitance gradients associated with $C_{NT}$, $C_G$, $C_D$ and $C_S$. In this work,

the values of the α coefficients (*i.e.* the weighting coefficient in the determination of the nanotube surface potential) have been determined phenomenologically, without calculating $C_{NT}$, $C_G$, $C_D$ and $C_S$. The values of the weight coefficients are equal $\alpha_{NT}$=0,19, $\alpha_G$=0,70, $\alpha_S$=0,10 and $\alpha_D$=0,01. All α coefficients were calculated with accuracy ±0,02. This shows that the nanotube potential in such experiments is only consist to ~20% of the KFM signal.

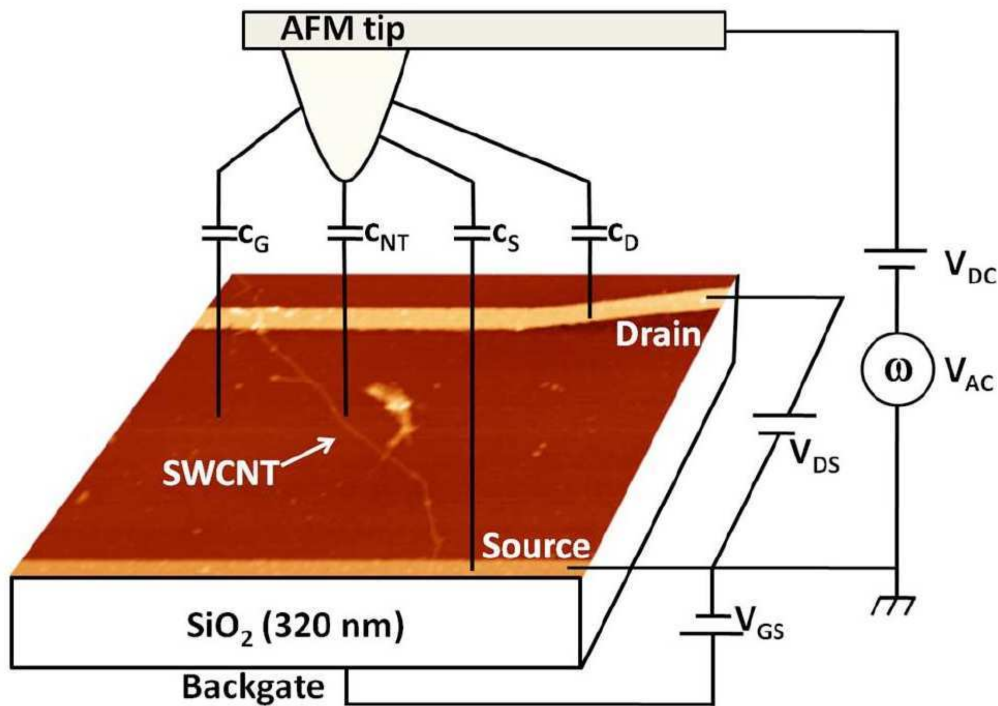


*Figure A 3 Schematics of the KFM detection setup, showing the 5 × 5 μm² atomic force microscopy topography image of a CNTFET in backgate geometry. Source, drain, and gate potentials are denoted $V_S$, $V_D$, and $V_G$, respectively. The tip/nanotube $C_{NT}$ and side capacitances $C_G$, $C_D$, and $C_S$ are represented schematically. From Ref. [3].*

Finally, Krok *et al.* [4] pointed out the role of side-capacitance effects in non-contact atomic force microscopy studies of KBr islands by frequency-modulation KFM. It was found that for islands with comparable or smaller size as the tip apex, the surface potential measured by KFM only becomes a fraction of the real island surface potential value. In this case, two effects have been pointed out, which can influence the measurement of surface potentials. The first one is associated with side-capacitance effects, in line with the work of Jacobs *et al.* [1]. The second effect is the averaging of the potential over the whole tip trajectory, since here both the KFM loop and the topography control loop are operated simultaneously. This effect will be discussed in the following, in the case of our experiments.

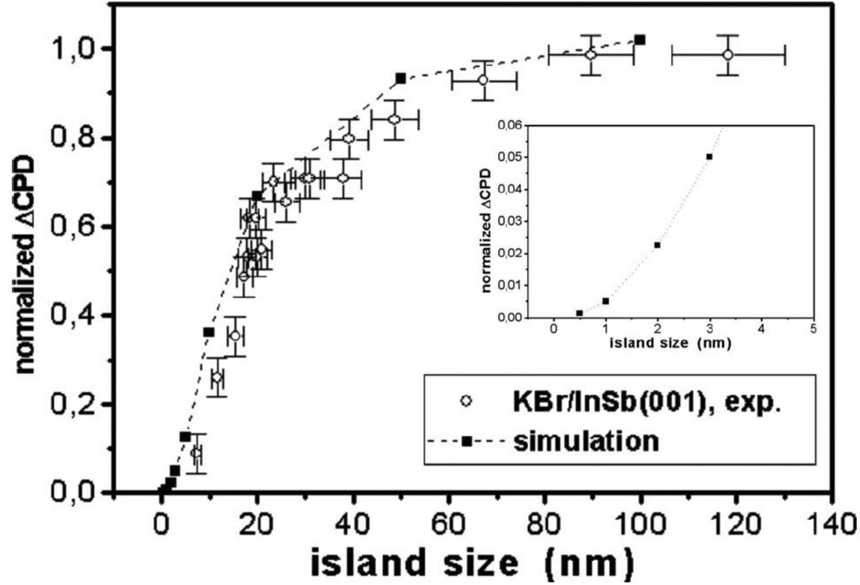


*Figure A 4 Measured $V_S$ (ΔCPD) by frequency modulation Kelvin force microscopy (FM-KFM) over KBr islands versus their size (open circles). The values are normalized (0 mV≡0 and −210 mV≡1) in order to compare with the numerical calculations (solid circles). The calculations were performed for square islands of surface potential $V_{island}$=1 V. In the simulations, the tip of radius $r_{tip}$=20 nm vibrates with an amplitude of A=40 nm and the closest tip-surface approach is set to $z_{min}$=1 nm. The inset represents a zoom for small island sizes. From Ref. [4].*

## A 2 Principle of calculation of surface potentials from static force fields

In this paragraph, we describe our developments to calculate surface potentials from static force fields. In the following, vectors will be indicated by **bold fonts**.

The surface potential measured by an amplitude-modulation KFM loop is the $V_{dc}$ value which cancels the z-component of the electrostatic force $\mathbf{F_\omega}$ at the electrostatic actuation angular frequency ω:

$$F_\omega = \frac{\partial C}{\partial z} V_{AC} \sin(\omega t)(V_{dc} - V_S)$$

Since we are not interested in describing here the contact potential difference stemming from differences in substrate and tip work-functions, we will assume $V_s$=0. We rather wish to describe the surface potential $V_{S,Q}$ generated by a fixed charge Q inside a nanostructure. From a physical point of view, such a static charge interacts with the tip capacitive charges at the

angular frequency ω, which generates a force component proportional to Q at the angular frequency ω. This force will be taken into account by the KFM loop as an effective surface potential $V_{S,Q}$, (*i.e.* it will be compensated by a $V_{dc}=V_{S,Q}$ value on the tip). $V_{S,Q}$, is here expected to be dependent on the tip-substrate distance z.

We start with the expression of electrostatic force as function of the electric field **E** on the tip:

$$\mathbf{F_{tot}}=\tfrac{1}{2}\,\varepsilon_0 \iint \mathbf{E}^2\mathbf{dS}$$

where the two-dimensional integral describes the surface of the tip probe.

If the tip bias is now the tip electrostatic excitation voltage $V(t) = V_{dc} + V_{ac}\sin(\omega t)$ at the angular frequency ω, the total field in presence of a surface (or nanostructure) charge Q can be written, due to the superposition theorem:

$$\mathbf{E} = \mathbf{E}_{dc} + \mathbf{E}_Q + \mathbf{E}_{ac} \sin(\omega t)$$

in which $\mathbf{E_Q}$ corresponds to the electrostatic field generated by the charge Q, in absence of electrostatic excitation. The 1ω component of the force can be easily calculated:

$$\mathbf{F_{1\omega}}=\varepsilon_0 \iint (\mathbf{E}_{dc} + \mathbf{E}_Q)\, \mathbf{E}_{ac}\, \mathbf{dS} \qquad (1)$$

In the above formula, there is a positive sign in front of $\mathbf{E}_Q$, because the electric field is here considered on the tip, in contrast with the negative sign before the potential $V_s$ in the usual expression for $\mathbf{F_{1\omega}}$ since the potential $V_s$ is taken on the surface.

To calculate the mixed integral in the expression of $\mathbf{F_{1\omega}}$, a simulation of three static forces will need to be done in the following (*i. e.* with a static bias $V_{stat}$ applied to the tip):

- the force $\mathbf{F_{Vstat=0V,\,Q\neq0}}$ obtained with a grounded tip ($V_{stat}=0$), and with a charge $Q\neq0$.
- the force $\mathbf{F_{Vstat\neq0,Q=0}}$ obtained with the tip polarized with $V_{stat}\neq0$, but without additional charge in the tip-substrate capacitance (Q=0).
- the total force $\mathbf{F_{Vstat\neq0,\,Q\neq0}}$ obtained when the tip is polarized with $V_{stat}\neq0$, and in presence of a surface or nanostructure charge $Q\neq0$.

The superposition theorem leads here to:

$$\mathbf{F_{Vstat\neq0,\,Q\neq0}} = \mathbf{F_{Vstat\neq0,\,Q=0}} + \mathbf{F_{Vstat=0,\,Q\neq0}} + \varepsilon_0 \iint \mathbf{E}_Q\cdot\mathbf{E}_{stat}\,\mathbf{dS} \qquad (2)$$

where $\mathbf{E}_Q$ and $\mathbf{E_{stat}}$ are the electric fields on the tip for ($V_{stat}$=0V; $Q\neq0$) and ($V_{stat}\neq0$; Q=0), respectively. This expression can be used to replace the mixed term in Eq. (1) by a set of static force components. More precisely, the first term in Eq (1) (purely capacitive term) can be written as $2(V_{ac}V_{dc}/V_{stat}^2)\,\mathbf{F_{Vstat\neq0,Q=0}}$, while the second term (mixed integral) corresponds

to the double product of $\mathbf{F}_{\mathbf{Vstat\neq0,Q\neq0}}=\frac{1}{2}\varepsilon_0\iint(\mathbf{E}_{\mathbf{stat}}+\mathbf{E}_{\mathbf{Q}})^2\mathbf{dS}$ multiplied by $V_{ac}/V_{stat}$, and can thus be replaced using the development of Equation (2).

Working now with the z-projection of electrostatic forces, the KFM condition $F_{1\omega}=0$ leads to the following equation:

$$0=\frac{2V_{dc}F_{V_{stat}\neq0,Q=0}}{V_{stat}}+F_{V_{stat}\neq0,Q\neq0}-F_{V_{stat}\neq0,Q=0}-F_{V_{stat}=0V,Q\neq0} \qquad (3)$$

so that the surface potential which is measured by KFM can be expressed as a function of static force fields only, using :

$$V_{dc}=-V_{stat}\times\frac{F_{V_{stat}\neq0,Q\neq0}-F_{V_{stat}\neq0,Q=0}-F_{V_{stat}=0V,Q\neq0}}{2F_{V_{stat}\neq0,Q=0}} \qquad (4)$$

This expression can be used to conveniently simulate surface potentials, since it only involves a set of static forces which can be obtained easily from a Poisson solver[2]. Keeping in mind that the regulated value of the surface potential $V_{dc}$ is a phenomenological description of the total electrostatic force $F_{Vstat\neq0,Q\neq0}$ in the form of $A + B \times (V_{stat} - V_{dc})^2$ (here with a bias $V_{stat}$ at the tip), Equation (2) can be also understood as the cross-term interaction, between the surface charge Q and capacitive charges at the tip (hence, the force $F_{Vstat\neq0,Q\neq0}$ when corrected from the purely capacitive and image charge force components $F_{Vstat\neq0,Q=0}$ and $F_{Vstat=0,Q\neq0}$), normalized by twice the capacitive force $F_{Vstat\neq0,Q=0}$. Our formula extends the procedure used by Charrier *et al.* [2] who calculated the static electrostatic force as a function of $V_{stat}$ in order to extract the surface potential from a parabolic force fit.

## A 3 Simulations using Comsol Multiphysics

Numerical simulations have been performed using a commercial Poisson solver (Comsol Multiphysics version 3.4). By this system it is possible to graphically model the KFM geometry (Figure A 5). Once the surface charge and boundary conditions are defined, Comsol will solve the Poisson equation using finite elements, enable to plot the electric potential between the tip and surface (Figure A 6), and to calculate electrostatic forces on the tip. All simulations have been done using a cylindrical symmetry, and taking a disk-shape

[2] Since Equation (2) is also independent of the value of $V_{stat}$ used to compute the static forces, one may also use in practice $V_{stat}=1V$, and take the following expression:

$$V_{dc} = -(F_{Vstat=1V,\,Q\neq0} - F_{Vstat=1V,\,Q=0} - F_{Vstat=0V,\,Q\neq0})/\,2F_{Vstat=1V,\,Q=0}$$

cantilever with equivalent capacitance gradient as compared to experimental cantilevers[3]. Simulations using a three-dimensional geometry would also be available in Comsol, but however less convenient due to limited computational resources [2]. We checked that the output of the simulations did not depend on the meshing introduced in Comsol.

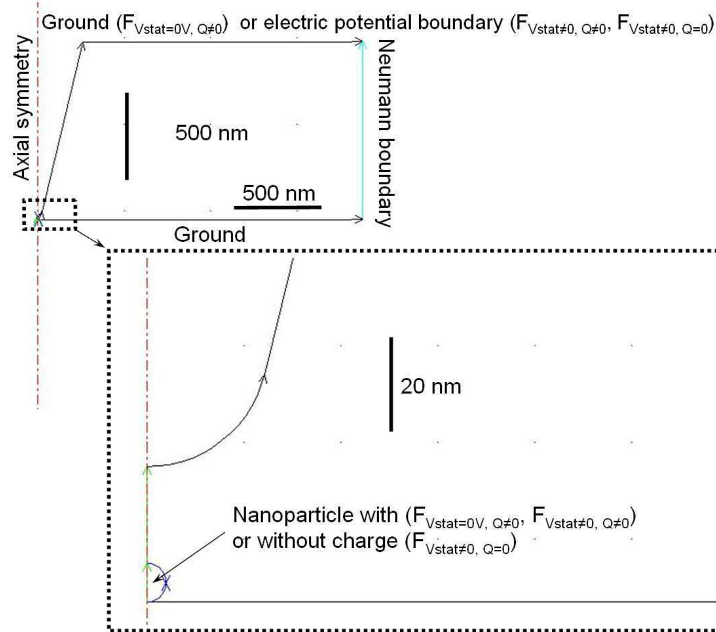


*Figure A 5 Drawing of KFM system with boundaries in Comsol solver. Top: full simulation, in which the upper boundary corresponds to an effective cantilever. Bottom: zoom close to the tip apex.*

By changing boundaries and the nanostructure charge, this solver permits to simulate the z component of three forces: $\mathbf{F_{Vstat\neq0,\ Q\neq0}}$, $\mathbf{F_{Vstat\neq0,\ Q=0}}$, $\mathbf{F_{Vstat=0V,\ Q\neq0}}$ from which the $V_{dc}$ values can be calculated, as discussed above. Boundary conditions consist in *(i)* grounding the surface (considered as a metal) ; *(ii)* setting the tip bias to V ; *(iii)* introducing Neumann boundary conditions (zero radial electric field) on the radial edge of the simulation box.

Tips with radius of apex equal 25nm and 15° of angle were used in this simulation. The error arising when changing the size and angle of the tip has been estimated. Shifting the radius of the tip from 20 to 30 nm and the angle from 10° to 20° generates a 5% of difference in $V_{dc}$ at most. The average distance between tip and surface was set to 20nm. The oscillation of the tip has also been introduced to take into account the non-linearities of the Coulomb

[3] The full cantilever (here EFM PPP, Nanosensors) of 225µm length, 28µm width, tip substrate distance ~13.5µm and 15° tilt-angle with respect to the substrate (when mounted in the VT-AFM holder) has been replaced in the calculations by a much smaller cantilever so as to avoid meshing issues such as in the work of Charrier *et al.* [2]. We took here a cantilever reproducing the experimental cantilever capacitance gradient with respect to the surface ($5{,}4\times10^{-11}$ F/m) in the form of a disk of height 1.04µm with respect to the surface, and radius 1.45µm.

force fields (see section A 5). The nanocrystal ionization has been described in the simulation as a homogeneous charge spread in the nanocrystal volume.

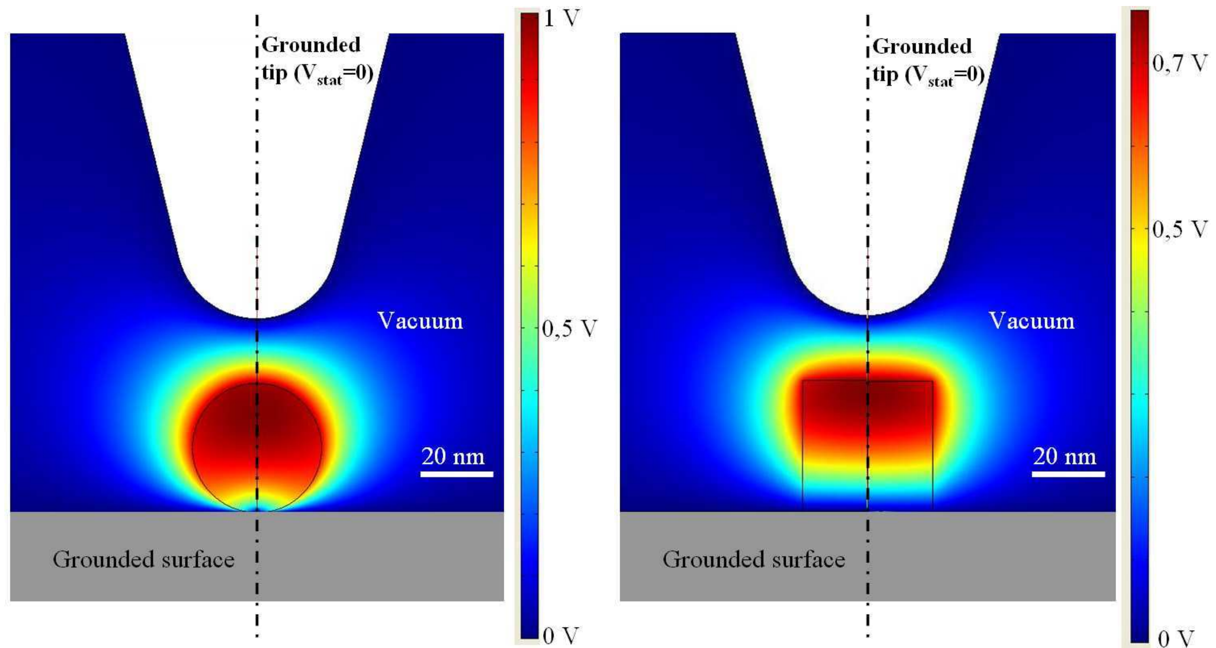


*Figure A 6 Solution of Poisson equation (electric potential) in the graphical interface of Comsol. The images show the grounded tip and a charged nanocrystal (treated here as a dielectric medium with a homogeneous charge) on a grounded surface, for a spherical (left) or cylindrical (right) shape.*

A cross section of the electric potential along the tip-substrate z axis can be extracted from the potential plot of Figure A 6, and is illustrated in Figure A 7, here for a charged nanocrystal (of spherical or cylindrical shape), and for a grounded tip condition. In both graphs, the nanocrystal electrostatic potential is dominated by the (here) negative curvature induced by its positive charge, leading to a positive maximum nanocrystal potential. This potential generates a non-zero electric field at the tip, resulting in image forces. This field is precisely the quantity which would be compensated by a dc bias in a static version of a Kelvin force apparatus, enabling to measure the nanocrystal electrostatic potential. Nanocrystals with different shapes can give dissimilar values of potential. The maximum of potential which can be read from cross-sections taken from the Figure A 6 for spherical and cylindrical shape is different in the order of 25% (Figure A 7). For our work, we will define nonetheless the nanocrystal electrostatic potential as the volume average of the electrostatic potential obtained from the simulations with a grounded tip and a charged nanocrystal (the charge is considered as spread over the nanocrystal volume). This choice is arbitrary, but this value was found to

differ from the surface average electrostatic potential and from the maximum value of the nanocrystal electrostatic potential by ~10%.

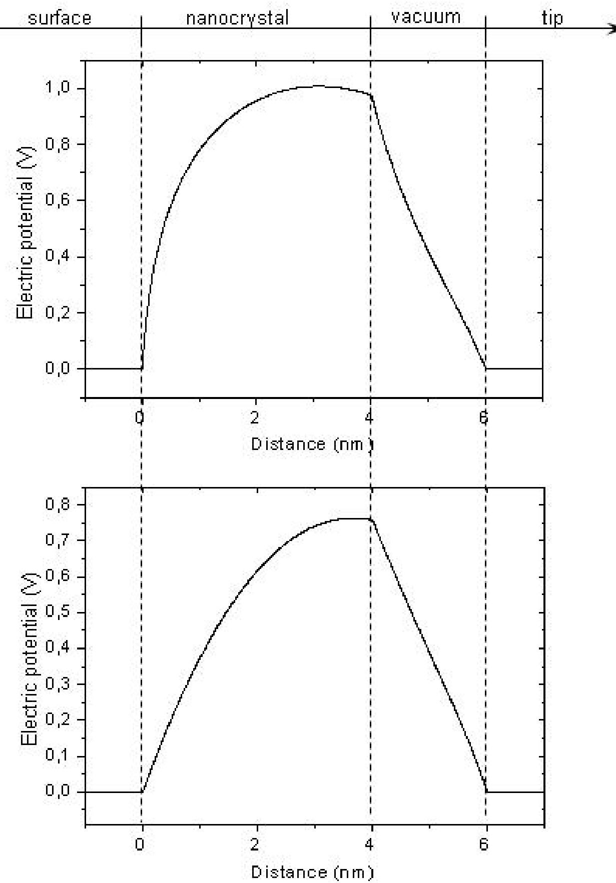


*Figure A 7 Cross-sections of the electrostatic potential taken form spherical (top) and cylindrical (bottom) nanoparticles with charge density=$10^{18}$ $cm^{-3}$. The data are extracted from Figure A 6.*

## A 4 Illustration of side-capacitance effects

We first illustrate the influence of side-capacitance effects in Figure A 8 in the case of a charged disk (with adjustable base diameter) within in a thin (10nm) dielectric layer. The interest of this simulation is that an analytical solution for the surface potential can be obtained in the case of a homogeneously charged thin layer, and in the limit of planar capacitances [5]: $V_s=\rho h^2/2\varepsilon_0\varepsilon_r$, in which h is the layer thickness, $\rho$ its volume charge and $\varepsilon_r$ its relative dielectric constant. This value is taken to normalize the calculated $V_{dc}$ potentials in Figure A 8. Two situations are shown. First a situation with a "flat tip" (here, in practice, with a tip-substrate distance 400nm), showing that the normalized electrostatic potential monotonically increases from 0 to 1 when the charged area base diameter is increased from 0 to the cantilever diameter ($2 \times 1.45\mu m$). The parabolic behaviour can be here assigned to the

fact that side-capacitance effects are governed by the surface of the charged area, but not its diameter.

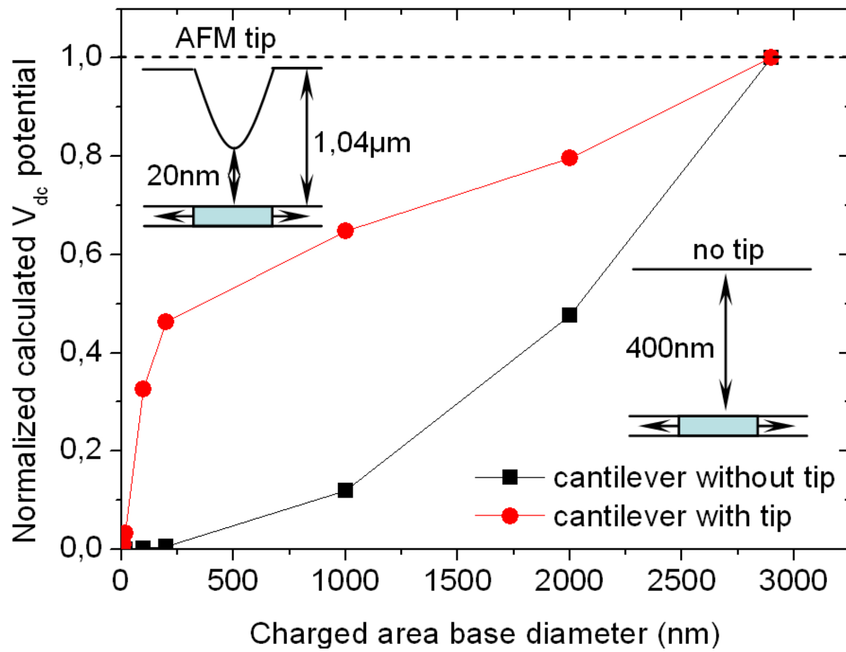


*Figure A 8 Calculation of $V_{dc}$ potential for a cylindrical area within a dielectric layer of with fixed height=10nm. The simulation was done for a cantilever with (red curve) and without tip (black curve).*

A similar calculation is then performed with a tip on the cantilever (see inset). This enhances the surface potential felt by the tip apex. However, for a disk of diameter 100nm, the contribution of the disk to the average calculated surface potential is only typically 30%, meaning that side capacitance effects take a significant part in KFM signals, even for short tip-substrate distances such as those used during non-contact topography imaging.

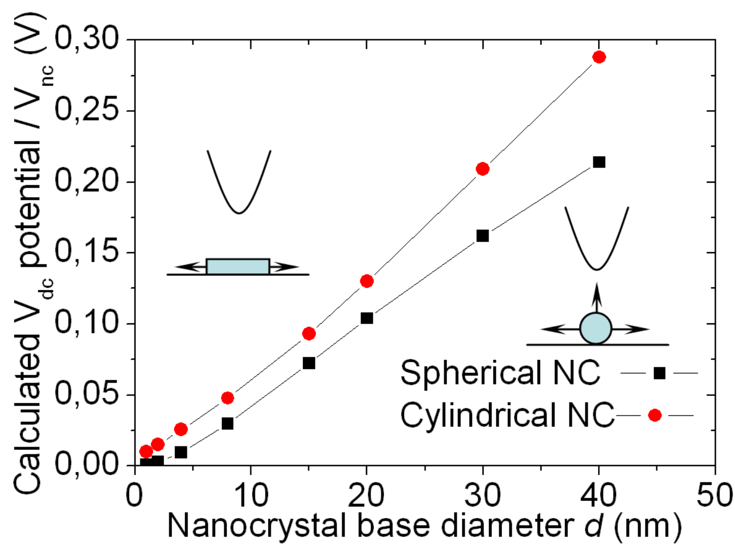


*Figure A 9 Calculated surface potential divided by the average nanocrystal electrostatic $V_{nc}$ for spherical and cylindrical (with fixed height h=8 nm) nanocrystals (see text).*

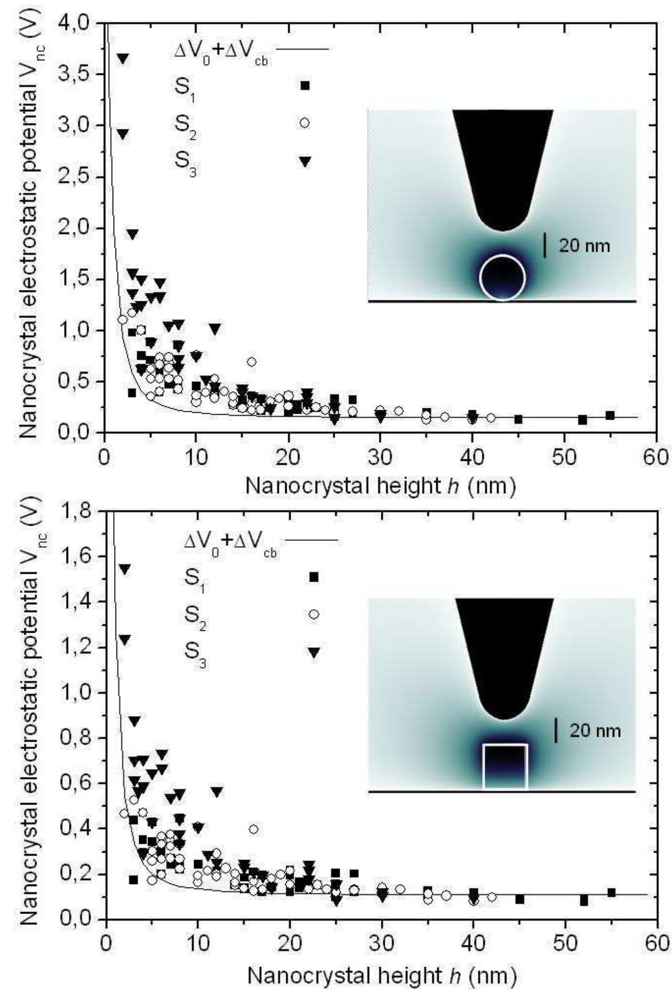


*Figure A 10 Nanocrystal electrostatic potential as a function of the nanocrystal height derived from raw KFM data when assuming a static tip at 20nm above the nanocrystals. Data points correspond to the n-type doped nanocrystal samples $S_1$, $S_2$ and $S_3$ and the full line corresponds to the increase of the electrostatic potential expected from quantum-mechanical calculations (see chapter III).*

To further illustrate side-capacitance effects in our KFM measurements on nanocrystals, we calculated the ratio between the potential regulated by the KFM loop (as calculated from Eq. 4) and the value of the nanocrystal electrostatic potential $V_{nc}$ (as defined in A 3). Results have been plotted in Figure A 9, first for a nanocrystal with cylindrical shape (in that case, the nanocrystal has a fixed height h=8nm and "grows" laterally when the nanocrystal base diameter is increased), then for a nanocrystal with spherical shape (in that case, the tip is also lifted from the surface when the nanocrystal diameter is increased, since we use a fixed tip-nanocrystal distance). The tip-surface distance is set to a fixed value of 20nm. In both cases, it is seen that the $V_{dc}$ output of the KFM loop decreases drastically when using smaller nanocrystals, which illustrates the need to take into account side-capacitance

effects in the quantitative interpretation of KFM experiments in vacuum. For nanocrystals typically smaller than the atomic force microscopy tip apex, the surface potential measured by KFM is thus only a fraction[4] of the "real" surface potential [1][2][4].

The conclusion of these simulations is that the real electrostatic potential of the nanocrystals used in the Chapter III of this manuscript can only be extracted from numerical simulations, provided side-capacitance effects are taken into account, due to the size range (2-50nm) of the investigated nanocrystals. Results are shown in Figure A 10, and show that the fairly flat raw KFM data (see Chapter III) for samples $S_1$, $S_2$ and $S_3$ (partially ionized *n*-type doped nanocrystals) correspond to a strongly enhanced electrostatic potential for small-size nanocrystals (up to a factor 7-10), in fair agreement with quantum mechanical expectations (full line, see chapter III), although no tip oscillation has been taken into account here.

## A 5 Calculations in the case of an oscillating tip

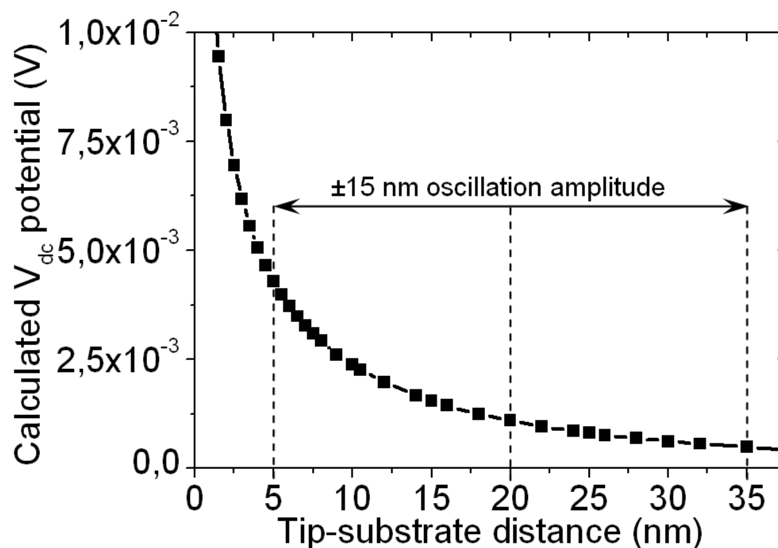


*Figure A 11 Simulation of the $V_{dc}$ potential regulated by the KFM loop as a function of the tip-nanocrystal distance, for a charged nanocrystal (charge density=$10^{18}cm^{-3}$) of height h=8nm and spherical shape, without tip oscillation. This plot illustrates the non-linearity of the KFM signal. The horizontal arrow shows our experimental scanning conditions (20nm tip-substrate distance and ±15nm oscillation amplitude).*

[4] This effect is stronger for the nanocrystals with cylindrical shape, since only the nanocrystal base diameter is changing here (but not their height). In the spherical case, a change in capacitances is also introduced by the fact that the tip is lifted by the increase in the nanocrystal diameter, since it follows the nanocrystal topography.

In the AM-KFM scheme used in our non-contact atomic force microscopy experiments, the KFM surface potential is explored by nullifying the cantilever oscillation amplitude at its second resonance frequency, but it is however oscillating at its first resonance frequency which is used for the non-contact topography control loop. Physically, since the KFM loop bandwidth (typically 200 Hz) is small compared to the first resonance frequency (60 kHz), this means that the surface potential seen by the KFM loop is a time-average of the surface potential which would be instantaneously be measured during the tip oscillation.

The calculation of the $V_{dc}$ potential must therefore be corrected by taking into account the tip oscillation. To illustrate this effect, we first presented in Figure A 11 the value of $V_{dc}$ potential which would be measured (without tip oscillation) as a function of the tip-nanocrystal distance, for a spherical nanocrystal of height h=8nm, and a charge density $10^{18}$ $cm^{-3}$. The dc potential is seen to increase non-linearly when the tip-substrate distance is reduced, meaning that the averaging of the KFM potential during the tip oscillation has to be taken into account properly in the simulations for our scanning conditions (±15nm oscillation for an average tip-substrate distance of 20nm, see horizontal arrow in Figure A 11).

The effect of the tip oscillation can be taken into account in our calculations by coming back to Equation (3). This in-line equation can be integrated over time (*i.e.* over the tip oscillation), by keeping $V_{dc}$ independent of time, as explained above. This enables to derive $V_{dc}$ as a function of the static electrostatic forces, in analogy with Equation (3):

$$V_{dc} = -\frac{\int F_{V_{stat}\neq 0, Q\neq 0}dt - \int F_{V_{stat}\neq 0, Q=0}dt - \int F_{V_{stat}=0V, Q\neq 0}dt}{2\int F_{V_{stat}\neq 0, Q=0}dt}$$

where the integrals stand for a cantilever oscillation period.

## A 6 Illustration of non-linear effects

To illustrate the evolution of the regulated KFM signal as a function of the tip-oscillation amplitude, we performed simulations for the same charged nanocrystal as in Figure A 11 (height h=8nm; spherical shape, charge density $10^{18}$ $cm^{-3}$), for a set of three average tip-surface distances (20nm, 6nm and 2.5nm), and by varying, for each tip-substrate distance, the ratio of the oscillation amplitude with respect to the tip-substrate distance. The

measured KFM signal is seen to be both enhanced by closer tip-substrate distances, but also by larger oscillation amplitudes, in qualitative agreement with Figure A 12. In our scanning conditions (20nm average substrate distance and ±15nm oscillation amplitude), the magnitude of the enhancement in the KFM signal for the nanocrystal is 87% with respect to a situation with no oscillation: this effect is a strong correction to be taken into account in the analysis of experimental data, which depends in addition on the nanocrystal diameter.

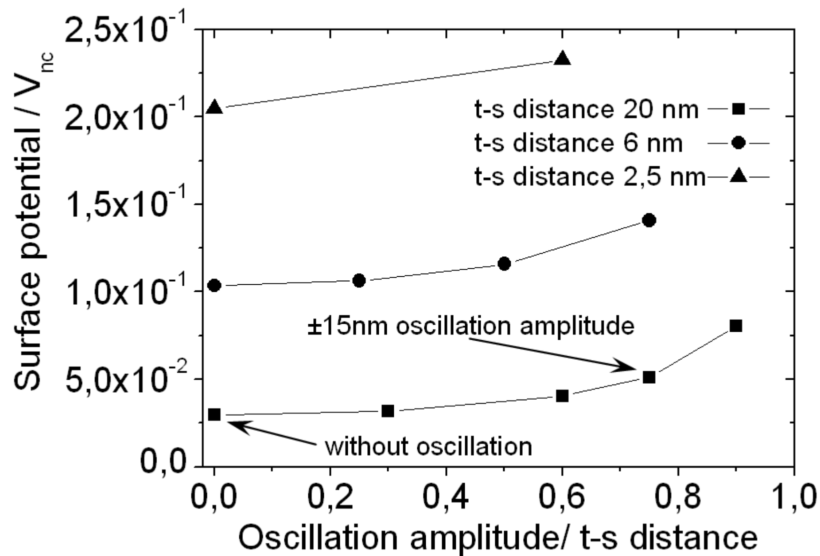


*Figure A 12 Surface potential normalized by the average nanocrystal potential $V_{nc}$ for a spherical nanocrystal (height h=8nm and volume charge $10^{18}$ $cm^{-3}$) as a function of the tip oscillation amplitude (this amplitude is here normalized by the tip substrate (t-s) distance for the sake of clarity).*

Figure A 14 shows now the nanocrystal electrostatic potential calculated from experimental data, and taking now into account non-linear effects, for the same set of *n* doped nanocrystals deposited on *n* doped surface as in Figure A 10. The oscillation of the tip (±15nm) has been here included to the calculations. This effect enhances the values of $V_{dc}$ (as compared with the case with a static tip) for a fixed nanocrystal electrostatic potential (see Figure A 12), and thus leads in practice so smaller values of the nanocrystal electrostatic potential $V_{nc}$ starting from the fixed experimental KFM data (see Figure A 10).

## A 7 Measurement of the minimum tip-substrate distance

In this section we show the experimental data used to measure the minimum tip-surface distance in the experiments of chapter III (this parameter is introduced in the simulations), which has been estimated from force-curve experiments.

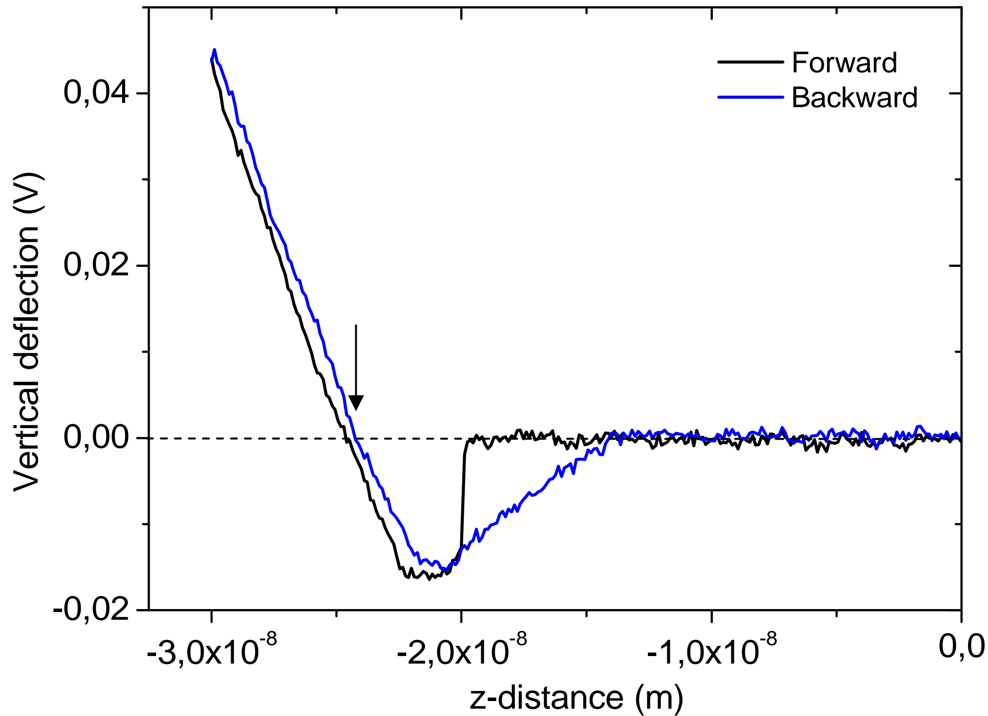


*Figure A 13: Experimental force curve obtained with the EFM tips used in the experiments of chapter III. The starting point (z=0) corresponds to the position of the EFM tip operated in non-contact mode (Δf=-5Hz, oscillation amplitude here of A=20nm). The mechanical excitation of the cantilever is switched off, and the force curve is then acquired (black curve: approach curve; blue curve: retract curve). The surface position corresponds here to z~-24.5nm (see arrow), corresponding to a minimum tip-substrate distance of ~4-5nm.*

A force curve (approach-retract curve) is shown in Figure A 13, in which the initial position of the tip with respect to the substrate (z=0) corresponds to the non-contact scanning conditions (here Δf=-5 Hz and an oscillation amplitude A=20 nm). The approach-retract curve is recorded after stopping the z-controller feedback loop and the cantilever mechanical excitation. This plot enables to find the position at which the tip is parallel to the surface prior to its deflection in the repulsive regime (arrow in Figure A.13). This position is here z=-24.5nm, which gives the minimum spacing between the surface and the tip of 4.5 nm. This curve gives also the slope of deflection on the photodetector with respect to the increase on the piezoelectric, in repulsive regime, which is ~130 nm/V which is used to set the cantilever oscillation amplitude to its desired value (here A=20nm).

# A 8 Conclusion

We have provided in this annex a description of the simulations used to derive the dc bias regulated by a Kelvin loop from the calculation of static force fields. The calculations enable to take into account *(i)* the effect of side-capacitances in amplitude modulation KFM; and *(ii)* the non-linear effects associated with the tip oscillation (if any) in KFM experiments. Results have been used to extract the electrostatic potential of ionized silicon nanocrystals with size in the 2-50nm range from the experimental KFM data.

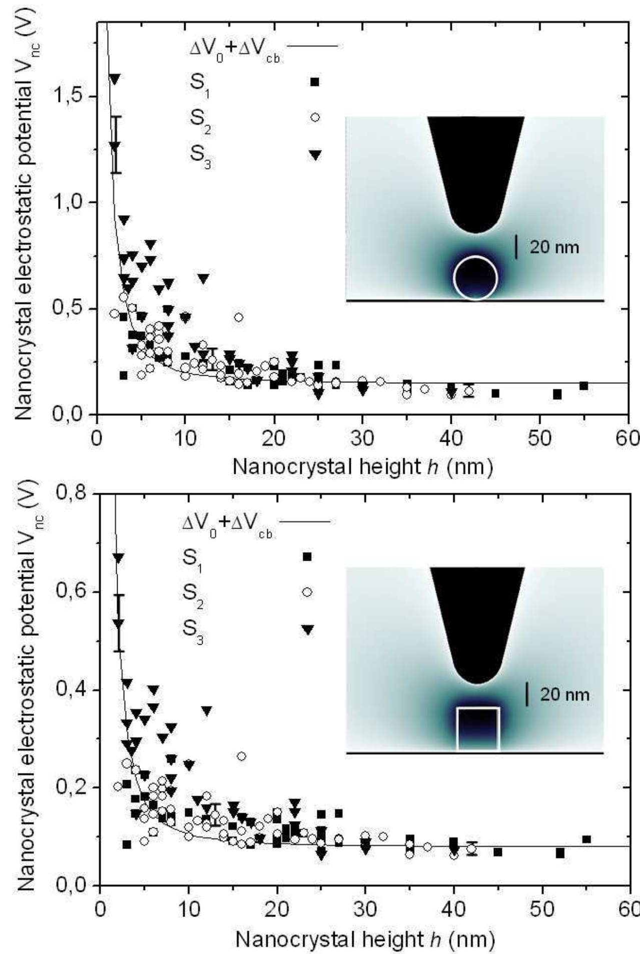


*Figure A 14: Nanocrystal electrostatic potential for oscillating tip for samples $S_1$, $S_2$ and $S_3$ (see Figure A 10), calculated from experimental KFM data, and taking into account the tip oscillation amplitude (±15nm) around the 20nm tip-substrate distance. Data have been calculated for two types of shapes for the nanocrystals: spherical and cylindrical.*

# References:

[1] "*Resolution and contrast in Kelvin probe force microscopy*" - H. O. Jacobs, P. Leuchtmann, O. J. Homan, and A. Stemmer, **Journal of Applied Physics**, 84, 3 (1998)

[2] "*Real versus measured surface potentials in scanning Kelvin probe microscopy*" - D. S. H. Charrier, M. Kemerink, B. E. Smalbrugge, Tjibbe de Vries, R. A. J. Janssen, **ACS Nano**, 2, 622-626 (2008)

[3] "*Determination of the electrostatic lever arm of carbon nanotube field effect transistors using Kelvin force microscopy*" D. Brunel, D. Deresmes, and T. Mélin, **Applied Physics Letters**, 94**,** 223508 (2009)

[4] "*Lateral resolution and potential sensitivity in Kelvin probe force microscopy: Towards understanding of the sub-nanometer resolution*" F.Krok, K.Sajewicz, J. Konior, M Goryl, P. Piatkowski, and M. Szymonski, **Physical Review B**, 77, 235427 (2008)

[5] "*Electric force microscopy of individually charged nanoparticles on conductors: An analytical model for quantitative charge imaging*" T. Mélin, H. Diesinger, D. Deresmes, D. Stiévenard, **Physical Review B**, 69, 035321 (2004)

# Annex B

## Silicon nanocrystals after high temperatures treatments, and measurements at low temperatures

# B 1 High temperatures treatments

*p*-NC/*p*-Si and *p*-NC/*n*-Si samples and their surface potentials were measured after heat treatment. These measurements were conducted because the *p*-type samples did not show an "effective" doping as compared to *n*-type nanocrystals, and with the hope to activate the dopants upon a heat treatment. The samples *p*-NC/*p*-Si and *p*-NC/*n*-Si were heated to 500 K inside vacuum during one hour and cooled down to room temperature at which the KFM measurements were performed.

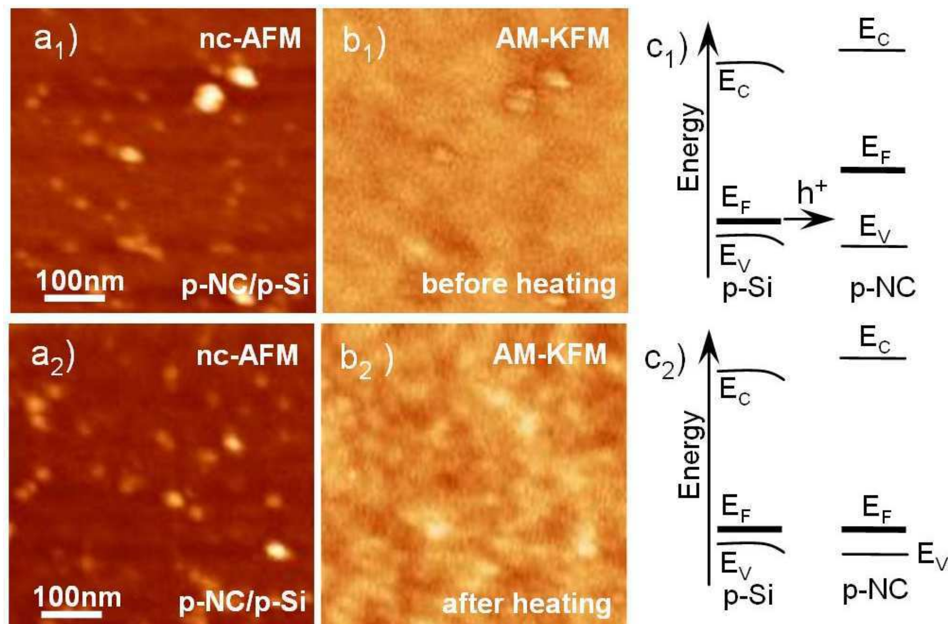


*Figure B 1 $a_1$) and $a_2$) 500×500 $nm^2$ non-contact AFM images (30 nm z-scale) of p-type doped nanocrystals on p-type wafer. $b_1$) and $b_2$) simultaneously recorded AM-KFM images (150 mV potential scales) before and after heating of sample to 500 K, respectively. $c_1$) and $c_2$) proposed energy diagrams prior to charge transfers (indicated by the arrow).*

The comparison between the KFM signals of the sample *p*-NC/*p*-Si before heating (Figure B 1 $b_1$) and after heating (Figure B 1 $b_2$) shows that the weak positive charge state observed before heating becomes imperceptible while the substrate background now shows surface potential features which are not correlated to the nanocrystal topography. We explain this point tentatively by either a reduction of surface defects of the *p*-doped nanocrystals, or an activation of dopants upon heating, corresponding to lowering of the nanocrystal Fermi level, as shown in Figure B 1 $c_{1,2}$.

This heat treatment has brought unexpected changes of the surface potential of the *p*-NC/*n*-Si sample. Assuming a similar behaviour as in the experiment of Figure B 1, the KFM signal of the *p*-NC/*n*-Si sample would be expected to be negative after heating, due to enhance electron transfer. The result (see Figure B 2 $b_1$) was exactly opposite: the nanocrystal surface potential became positive after the heat treatment (Figure B 2 $b_2$). Here again, the surface KFM potential of the substrate itself exhibits a granular structure, meaning that the substrate surface states have changed as well. We therefore would explain the KFM images after heat treatment to a different evolution of the hydrogenated *n*-type and *p*-type substrates upon heat treatments.

.

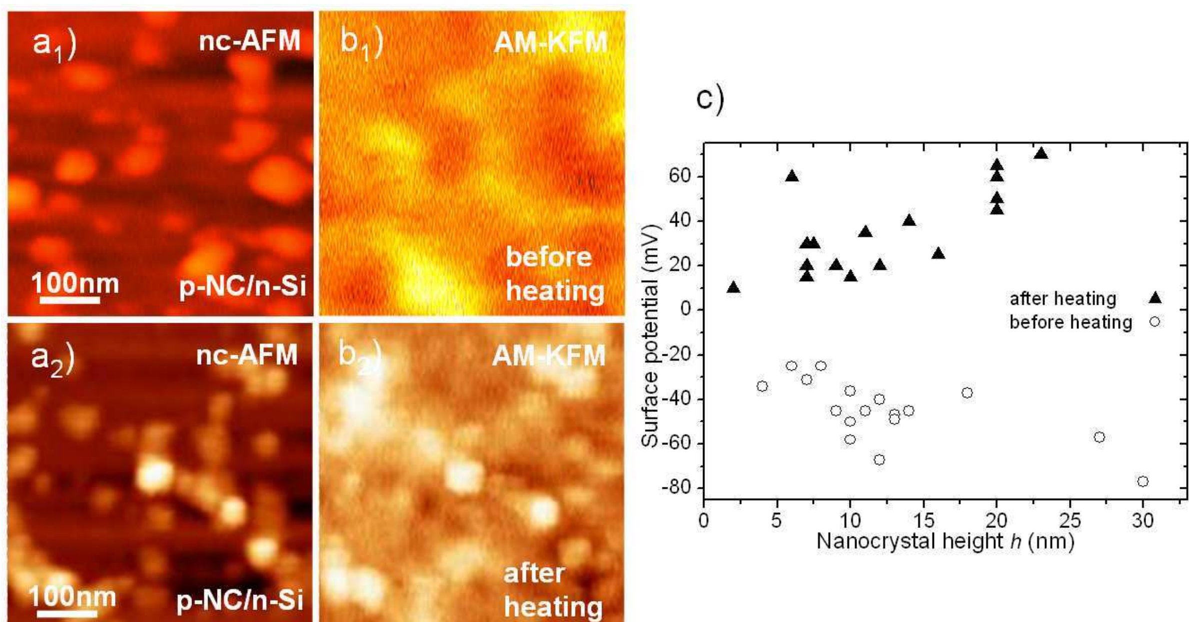


*Figure B 2 $a_1$) and $a_2$) 500×500 $nm^2$ nc-AFM images (30nm z-scale) of p-type doped nanocrystals on n-type wafers. $b_1$) and $b_2$) simultaneously recorded AM-KFM images (150 mV potential scale) before and after heating to 500 K, respectively. c) Comparison of KFM surface potential from sample p-NC/n-Si before (circles) and after heating (triangles) as a function of the nanocrystal h.*

## B 2 Measurements in low temperatures

Measurements using low temperatures were also achieved on *n*-type nanocrystals. Here the aim was to check that the charge transfer mechanism proposed in Chapter III was similar to a remote-doping mechanism, *i.e.* that the charge transfer cannot be frozen at low

temperatures. The *n*-NC/*n*-Si sample $S_1$ has been characterized for this purpose at temperatures: 25 K (Figure B 3 $b_2$) using liquid helium, 100 K using liquid nitrogen, and at room temperature (Figure B 3 $b_1$) as a reference. The surface potential of the sample *p*-NC/*p*-Si were measured at 25 K and 300 K. The AFM and KFM images do not correspond to the same surface area at low and room temperature, but are shown together for sake of comparison.

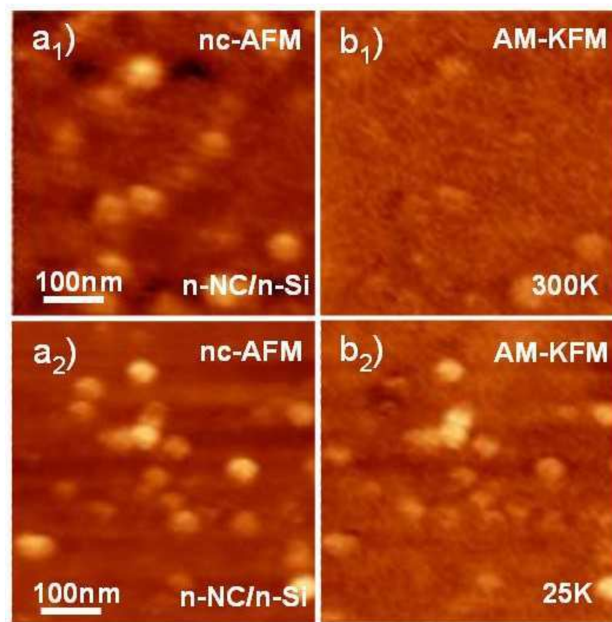


*Figure B 3 $a_1$) and $a_2$) 500×500 nm$^2$ nc-AFM images (30 nm z-scale) of n-NC/n-Si $S_1$ sample. $b_1$) and $b_2$) AM-KFM images at temperatures of 300 K and 25 K (85mV colour scale).*

For both samples *n*-NC/*n*-Si and *p*-NC/*n*-Si, the measurements done at low temperature are very similar to room temperature measurements, and show an increase - *in average* - of the KFM signal (Figure B 4). Additionally on *n*-NC/*n*-Si sample no significant difference between 25 K and 100 K can be observed. The increase in the KFM signal at low temperature might be related to a change in the screening of the nanocrystal charge of the semiconductor substrate. Additionally, an analysis of the nanocrystal surface potential fluctuations was made, by measuring the standard deviation from the linear fit of the nanocrystal surface potential as a function of their height. The values of the fluctuations are much higher at the low temperatures, as can be directly seen in Figure B 4 (left). The sample $S_1$ standard deviation equals 8.5 and 10 for the 20 K and 100 K, respectively, since in the room temperature this value is equal to 4.5. The same analysis was done for the *p*-NC/*p*-Si sample, without however enough data points to compare the values with the sample $S_1$. It is nonetheless visible from Figure B 4 (right) that the

fluctuations at low temperature are also higher as compared to room temperature in the case of *p*-NC/*p*-Si sample. We do not have yet an interpretation for this increase in surface potential fluctuations.

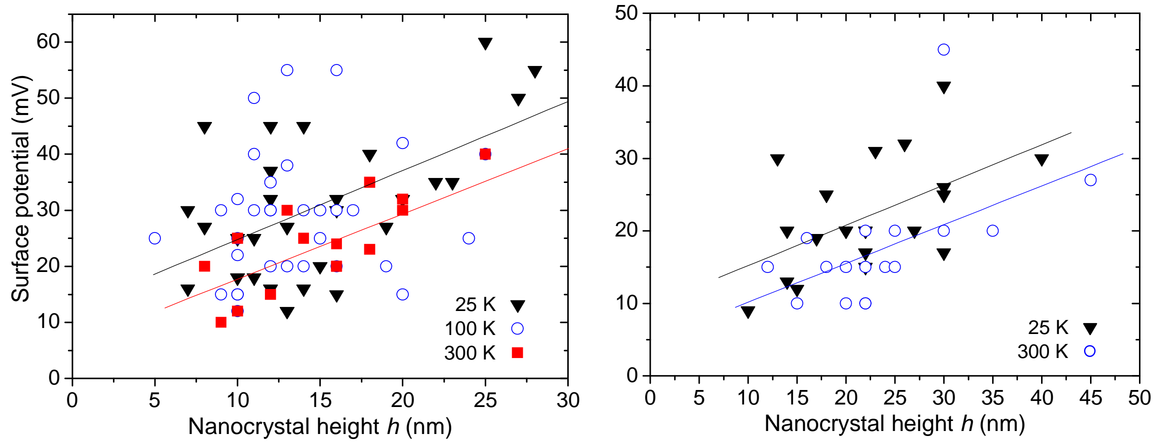


*Figure B 4 Nanocrystal electrostatic potentials with averaging trends from: n-NC/n-Si $S_1$ sample (left) taken in three temperatures 25 K, 100 K and 300 K, p-NC/p-Si sample (right) in temperatures 25 K and 300 K.*

# Annex C

## Amplitude-modulation KFM measurements on doped silicon nanowires

## C 1 Preparation of samples

Silicon undoped and doped nanowires (NWs) prepared by VLS on doped silicon substrates have been measured by amplitude modulation Kelvin force microscopy (AM-KFM) in ultra high vacuum. The aim was to detect the transfer of charge between the NWs and the substrate, and provide a qualitative evidence for doping. The measurement principle is identical to the work done in Chapter III in the case of silicon nanocrystals. The interpretation is however not straightforward, and will stay here at a qualitative level.

**Preparation of the nanowires**

Intrinsic, *p*-doped and *n*-doped silicon NWs have been grown by metal-catalyzed chemical vapour deposition on (111) silicon substrates (growth made by D. Hourlier). Nanowires have been harvested from their substrates and dispersed in isopropanol using an ultrasonic bath during a few minutes, and then deposited onto *p*-type and *n*-type silicon substrates with gold markers prepared using electron beam lithography (see Figure C1).

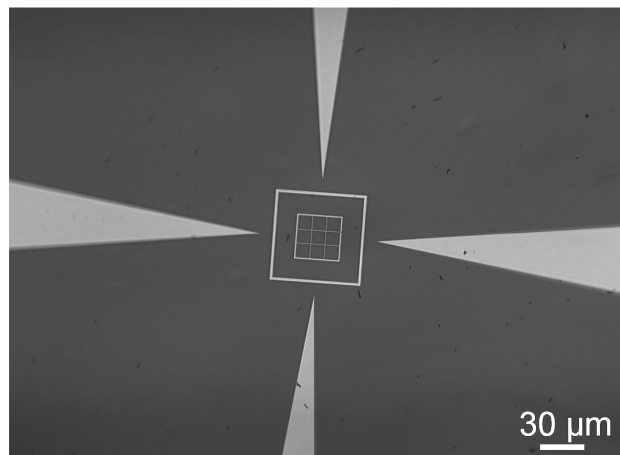


*Figure C 1 Optical view of sample with gold markers and deposited silicon nanowires.*

Measurements are made twice: first, after deposition (*i.e.* both the nanowires and silicon are covered by native oxide), and in a second step, after a 5 second HF/$NH_4F$ etch as previously described. Reference samples will be hereafter labeled *i*-NW/*n*-Si, *i*-NW/*p*-Si (intrinsic NWs deposited on the *n*-type and *p*-type surfaces), *n*-NW/*n*-Si, *n*-NW/*p*-Si (*n*-doped NWs deposited on the *n*-type and *p*- type surfaces), *p*-NW/*n*-Si, *p*-NW/*p*-Si (*p*-doped NWs deposited on the *n*-type and *p*-type surfaces). The de-oxidized nanowires will be labeled additionally with a capital letter E (for example *n*-NW/*n*-Si [E]).

## C 2 Amplitude modulation Kelvin force microscopy measurements

The surface potential of NWs is probed with a home-made (AM-KFM) set-up, which has been described in Chapter I. For silicon nanowires, here of diameters ranging from 50nm to 450nm, it proved very difficult to set all regulation loops (cantilever oscillation amplitude and phase, surface tip distance and regulated DC bias) in simultaneous non-contact topography and AM-KFM, during a full image acquisition. Cross-sections were recorded instead, as illustrated in Figure C 2. Such measurements are repeated along the nanowire length, providing a set of KFM data as a function of their diameter, due to the conical shape of the investigated nanowires.

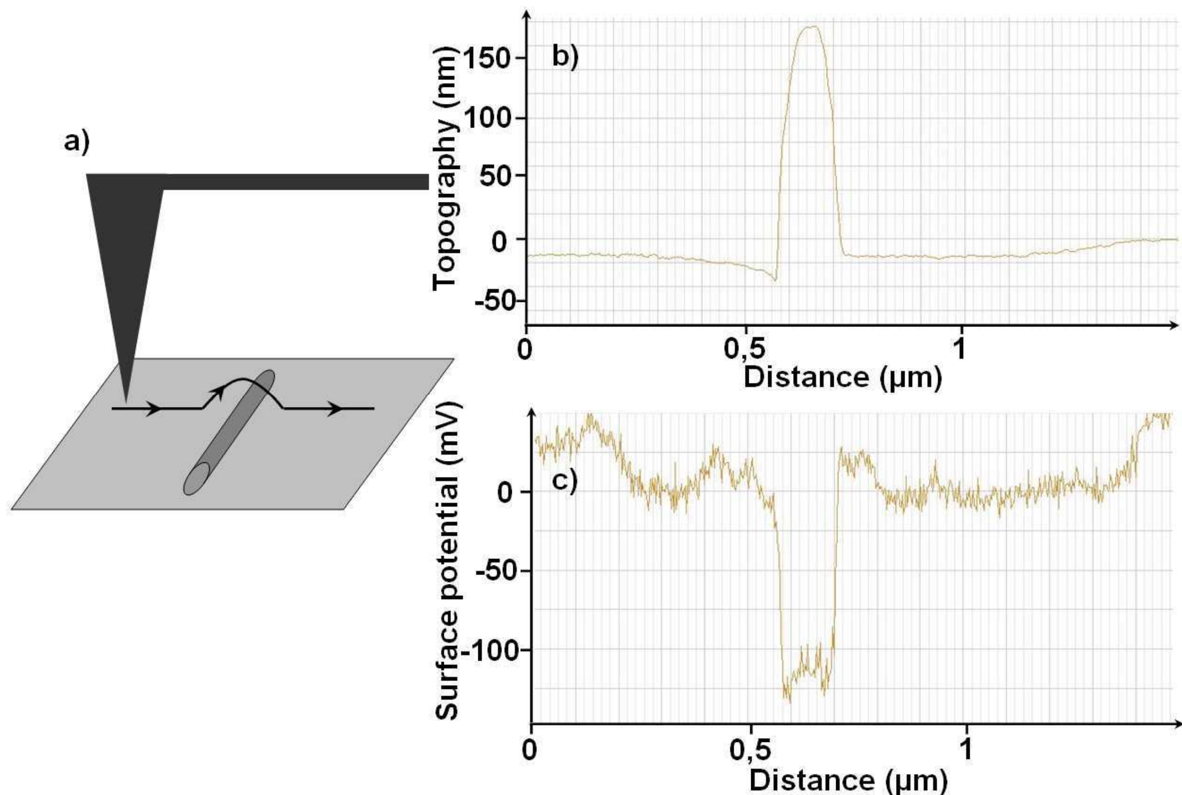


*Figure C 2 a) Schematics of the scan across the nanowire, and example of collected data: b) topography and c) surface potential.*

The raw surface potential data of a full set of intrinsic and doped nanowires is shown in Figure C 3, in which the various cross-sections along a given nanowire are represented as a function of the nanowire diameters. In this plot, empty symbols represent samples before de-oxidation, and full symbols represent the samples after etching. The

interpretation of experimental data is fairly complicated, because the nanowires have different diameters and diameter variations due to doping. It is not clearly understood yet why the KFM signal (here the difference in surface potential between the nanowire and surface) exhibits an almost systematic negative average component (also visibly increasing with the nanowire diameter), upon which some systematic behaviors can be observed. For instance, the *i*-NW/*n*-Si shows a higher surface potential as compared to the *i*-NW/*p*-Si, either before or after the $SiO_2$ etch step. On the other hand the *p*-NW/*n*-Si exhibits a clearly higher surface potential as compared to the *n*-NW/*p*-Si sample (but not of opposite sign) before de-oxidation, while the situation is reversed after de-oxidation.

We infer that the difficulty of the interpretation (as compared to the silicon nanocrystal samples) is due *(i)* to the large topography of the nanowires, for which any cross-coupling with the topography might occur in KFM signals ; *(ii)* to the nanowire surface states. Although some systematic behaviors can be observed (as described above), more investigation is needed to understand in details their electronic properties in relation with their growth.

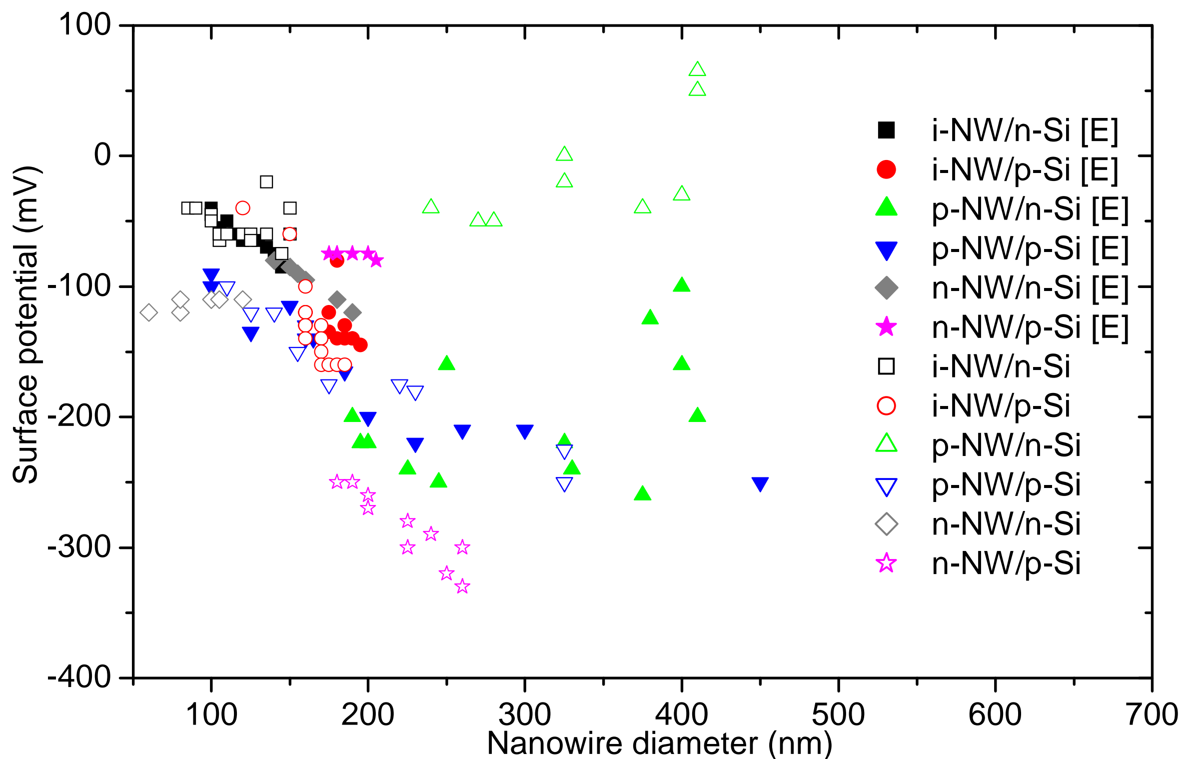


*Figure C 3 Surface potential as a function of the nanowire diameter for six samples with oxide (empty symbols) and after etching (full symbols).*

# List of publications and communications

## Articles:

**Ł. Borowik,** K. Kusiaku, D. Théron, T. Mélin - *"A formula to calculate amplitude modulation Kelvin force microscopy signals from static force fields"* Applied Physics Letters, accepted (2010)

**Ł. Borowik,** K. Kusiaku, D. Deresmes, D. Théron, H. Diesinger, T. Mélin, T. Nguyen-Tran, P. Roca i Cabaroccas - *"Charge transfer from doped silicon nanocrystals"* submitted (2010)

**Ł. Borowik**, K. Kusiaku, D. Deresmes, D. Théron, H. Diesinger, T. Mélin, T. Nguyen-Tran, P. Roca i Cabaroccas - *"Quantum confinement and surface states in silicon nanocrystals"* in preparation

**Ł. Borowik,** H. Diesinger, D. Hourlier, T. Mélin - *"Scanning-probe measurements on silicon nanowires"* in preparation

## Conferences:

**Ł. Borowik,** I. Gronowska - *"Acoustic microscope application to investigate bone techniques"* (poster presentation) University of Technology, Bydgoszcz, Poland, 27-30 June 2004

**Ł. Borowik,** I. Gronowska - *"Acoustic microscope application to investigate materials irradiated with laser beam"* (poster presentation) University of Technology, Bydgoszcz, Poland, 27-30 June 2004

**Ł. Borowik,** H. Diesinger, D. Hourlier, T. Mélin - *"Scanning-probe measurements on undoped silicon nanowires"* (poster presentation) Forum 2008 microscopies en champ proche , La Londe les Maures, 17-21 March 2008

H. Diesinger, D. Deresmes, D. Brunel, **Ł. Borowik,** D. Houlrier, T. Mélin - *"Optimization of the response of the KFM-cantilevers and the application to carbon nanotube devices"* (poster presentation) Forum 2008 microscopies en champ proche, La Londe les Maures, 17-21 March 2008

**Ł. Borowik,** H. Diesinger, D. Hourlier, T. Mélin - *"Scanning-probe measurements on undoped silicon nanowires"* (poster presentation) Summer school on semiconductor nanowires, Roscoff, 15-20 June 2008

**Ł. Borowik,** K. Kusiaku, D. Theron, H. Diesinger, D. Deresmes, T. Mélin, T. Nguyen-

Tran, P. Roca i Cabarrocas - *"Electrostatic properties of doped silicon nanocrystals probed by Kelvin force microscopy"* (oral presentation) Forum 2009 microscopies à sonde locale, Hardelot, 16-20 March 2009

**Ł. Borowik,** K. Kusiaku, D. Theron, H. Diesinger, D. Deresmes, T. Mélin, T. Nguyen-Tran, P. Roca i Cabarrocas - *„Charge transfer from doped silicon nanocrystals"* (poster presentation) 12th International Conference on Noncontact Atomic Force Microscopy Yale University, New Haven, CT, USA, 10-14 August, 2009

**Ł. Borowik,** K. Kusiaku, D. Theron, H. Diesinger, D. Deresmes, T. Mélin, T. Nguyen-Tran, P. Roca i Cabarrocas - *„Charge transfer from doped silicon nanocrystals"* (poster presentation) TNT 2009 Trends In Nanotechnology, Barcelona, Spain, 7-11 September 2009

**Ł. Borowik,** K. Kusiaku, D. Theron, H. Diesinger, D. Deresmes, T. Mélin, T. Nguyen-Tran, P. Roca i Cabarrocas - *"Kelvin probe force microscopy investigation of charge transfer mechanisms from doped silicon nanocrystals"* (oral presentation) 2009 MRS fall meeting , Boston, United States, 30 November 2009

## Seminar:

**Ł. Borowik** - *"Scanning-probe measurements on nanocrystals and nanowires in ultra high vacuum"* CEA-LETI, Grenoble, 3 July 2009

## Polish patent application:

**Ł. Borowik**, I. Gronowska, A. Latuszek, K. Lipiec, J. Orzechowski, M. Trzciński, L. Tykarski - *"Detection of delaminating in layered structures"* P-378 672 (2006)